3D Micro and Nanomanufacturing via Folding of 2D Membranes

by

Stanley M. Jurga, Jr.

S.B., Harvard University (2000)

Submitted to the Department of Mechanical Engineering
in partial fulfillment of the requirements for the degree of

Master of Science in Mechanical Engineering

at the

MASSACHUSETTS INSTITUTE OF TECHNOLOGY

June 2003

Signature of Author ....
Department of Mechanical Engineering
9 May 2003

Certified by ....
George Barbastathis
Assistant Professor of Mechanical Engineering
Thesis Supervisor

Accepted by ....
Ain A. Sonin
Chairperson, Department Committee on Graduate Students

3D Micro and Nanomanufacturing via Folding of 2D Membranes

by

Stanley M. Jurga, Jr.

Submitted to the Department of Mechanical Engineering
on 9 May 2003, in partial fulfillment of the
requirements for the degree of
Master of Science in Mechanical Engineering

Abstract

This thesis presents "membrane folding," a new method for manufacturing three dimensional (3D) micro and nanostructures. First, micro and nano features are patterned on a planar substrate just as they are today. Then the substrate is folded upon itself at predetermined creases or hinges, resulting in an organized, dense packing of 3D space. Membrane folding satisfies and in many ways surpasses the functional requirements of 3D, including connectivity, development and fabrication costs, heat dissipation, and scaling to multiple levels. The design, modeling, and fabrication of a single fold are described in full, and the end result is a proof of concept that works better than predicted. We have achieved large 180 degree motions with alignment to within $10\mu m$ with no mechanical or electrical failure. Steps have been made toward understanding how residual stress might aid folding actuation in an effort to find a more parallel means of assembly, and further improvements in the membrane folding strategies have been implemented in a second round of prototyping, which include multiple folds and integration of active MEMS elements on adjacent membranes.

Thesis Supervisor: George Barbastathis
Title: Assistant Professor of Mechanical Engineering

Acknowledgements

I never would have managed to succeed in my research and reap the numerous benefits offered by MIT without the help and support of many people. I have learned many things, especially those beyond the realm of science and technology.

George, the first time I met you I knew that this was going to be an awesome journey. I am not exactly sure what led me to believe this... maybe it was your infectious enthusiasm for research, your outgoing charisma, or the copy of Ultimate Dance Party II sitting on the top of your stack of CDs? Since that day I have not been let down in the least. Through the years you have provided me with guidance and flexibility in my research, and you have always been a source of motivation and inspiration. You have so many exciting ideas, and it has been a wonderful opportunity for me to work with you on developing these into a tangible reality.

I have so many thanks for everyone in the Optical Engineering Group. Carlos, Arnab, Wei-Chuan, and Greg, you all have contributed to my experience in such a tremendous way... from the technical to the farcical. In the process you really have become like a family, even though I am "the evil one."

Nick, it has been great sharing an office with you. Your insight is tremendous, and you have so many brainstorms that sometimes I thought you were going to take over my project! It has been fun bouncing ideas and jokes off of each other.

The staff from MIT's Microsystems Technology Laboratory, especially Kurt Broderick, Gwen Donahue, Dave Terry and Dennis Ward, have all helped out from training to troubleshooting, and especially making the cleanroom a little more comfortable. A portion of this work was conducted in Professor Hank Smith's Nanostructures Laboratory with the help of Jim Daley, Jim Carter, Dario Gil, and Mark Mondol. Rob Bernstein directed me in my search for information on residual stress in thin films, and the video analysis would not have been possible without the generosity of the Schmidt Group, including Xueen Yang and Christine Tsau.

Friends and family have been a constant source of support and perspective. Mom and dad, I would not be here without your love and support and all that you have done for me in the past. Blake, Lynsay, Al, Sam, Heather, Joel, Brian, and all the rest of the Pirate House crew, you are the best. It has been great living with you and it has always been nice to come home. Here's

to many more adventures! Kate and Aviva, you have always been and always will be a source of reason. Jason, Caitlin, Chip, Ariel, and the rest of the MIT cycling club, you have helped me achieve some goals I thought I would never accomplish. Without your efforts it would not have been possible or as enjoyable.

This research was funded by the NSF and MIT's CMSE.

Contents

List of Figures

List of Tables

Chapter 1

Introduction

This thesis presents a novel approach to building functional three dimensional (3D) micro and nanostructures in a way that maximizes integration of new and existing semiconductor technologies, minimizes cost in terms of capital investment and product development, and allows particular devices to be built that could not be realized with previous fabrication methods. 3D micro and nanostructures are necessary in numerous technological domains. Current architectures for VLSI integrated circuits and MEMS are quickly reaching a point where two dimensional real-estate has become saturated and can no longer become denser. In the realm of microelectronics, the 3^{rd} dimension promises to extend the pace of ever faster processors and higher-capacity memories beyond "the end of Moore's law," when feature sizes of planar electronics reach their minimum physical limit. In applications other than electronics, great gains in performance and functionality can be obtained from 3D integration of sensors and actuators into hybrid systems. For example, optical elements combined with microfluidics, logic units, RF communication, and energy scavengers may be combined into a complete, independent biological assay system or environmental monitoring. However, 3D fabrication is not well understood nor developed in practice. This thesis lays the foundation for manufacturing in 3D by means of a two step process called membrane folding. Micro and nanostructures are built on a large 2D membrane just as they are commonly fabricated today. Then the membrane is folded over on itself at predetermined creases. The end result is a dense volume of micro and nanodevices.

1.1 Membrane Folding

The concept of membrane folding is simple. It involves two steps; in the first step, all devices are fabricated on a planar substrate, or "membrane," just as they are in today's semiconductor industry. The membrane is then folded into a 3D structure by appropriate actuation means at designated compliant zones which act as hinges between stiffer regions containing the micro and nano devices created previously in the first step. By virtue of compliant circuitry that spans the hinge areas, full two dimensional (2D) connectivity is preserved across the entire membrane, even after folding. Connectivity is also achieved in the vertical, 3^{rd} direction by designing connections to be formed when the planar folds reach predetermined locations. Imagine creating a microchip as a long ribbon, and then folding the ribbon over on itself many times as depicted in Figure 1-1. Electrical as well as optical interconnects link each layer of the membrane in the vertical direction. This membrane may contain microelectronics, micro-optics, carbon nanotubes, nanosensors, or microfluidics. The final result is a wholly integrated system of sensors and actuators compacted into a dense volume.

The benefits of membrane folding for building in the 3^{rd} dimension are:

- massive, yet manageable connectivity throughout the volume
- organized architecture
- inexpensive development and production costs
- good thermal management
- the ability to scale indefinitely.

The essence of creating functional 3D micro and nanostructures through folding 2D substrates is that the fabrication of discrete devices (i.e. transistors, capacitors or pressure sensors) is decoupled from the assembly process.

1.2 Biological Motivation

This approach takes inspiration from biology. Examining how biological nature fills 3D space, one finds an interesting observation that functionally complex 3D compositions are often times

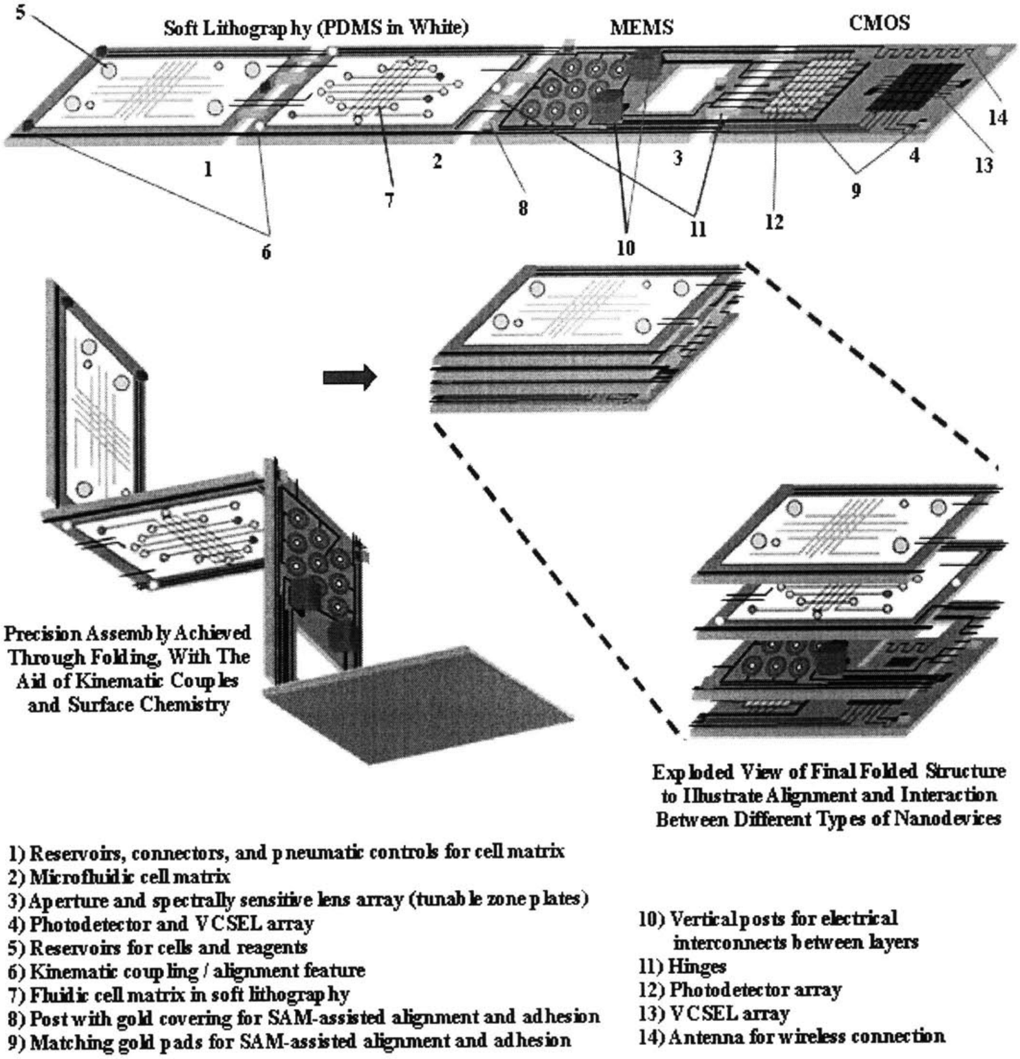

Figure 1-1: The vision of membrane folding.

built from lower dimensional structures that are layered or stacked together. For example, DNA and protein are 3D structures assembled from 1D strands. Trees grow outward as laminar sheets only one cell thick [50], and the primate brain is built of folded laminar sheets.

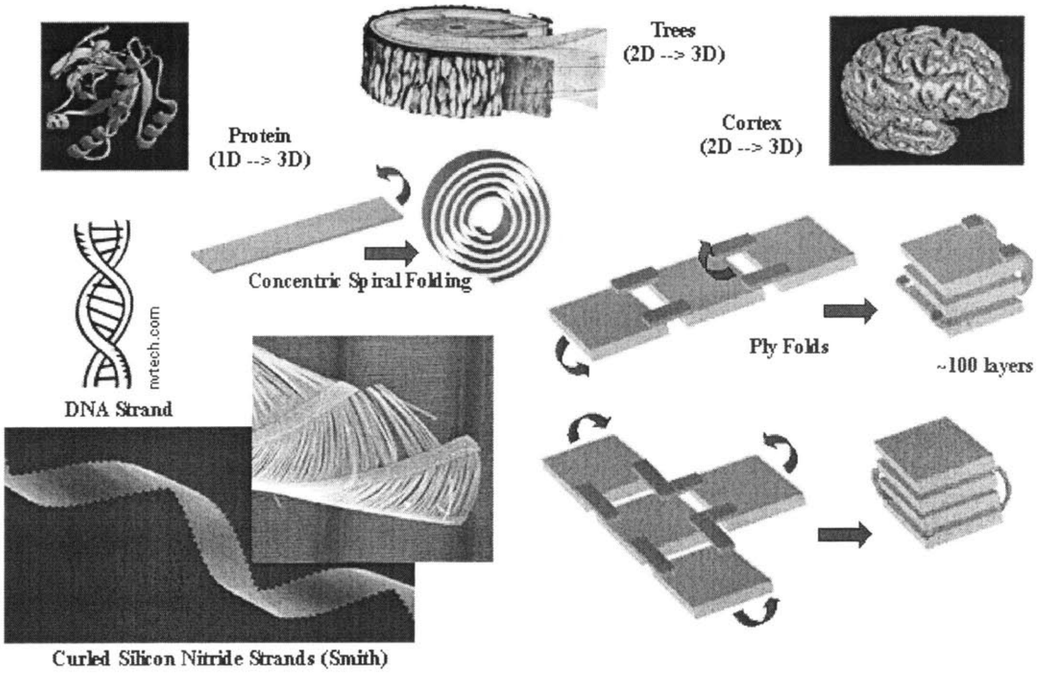

Figure 1-2: Volume filling strategies; natural and synthetic.

In particular, the visual cortex is a powerful example because in a sense it is a 3D processor about the size of a sugar cube. There are several major sections within the visual cortex, each of which is composed of folded membranes. Dissecting one region, the primary visual cortex or "V1," one finds that structurally it is a 2D membrane that is folded over on itself many times. Unfolded, it is a sheet measuring roughly four square inches containing more than 150 million neurons (as compared to a Pentium 4 processor with a billion transistors within 2.2cm^2 [25]). Neurons (i.e. circuitry) are distributed primarily along the length of the membrane and within the 2D topology. However, neurons also grow between the folded regions of the membrane, but to a much lesser degree [1]. Therefore, the final result is an anisotropic, 3D distribution of interconnects.

One can make the inference that evolution selected toward an anisotropic arrangement of

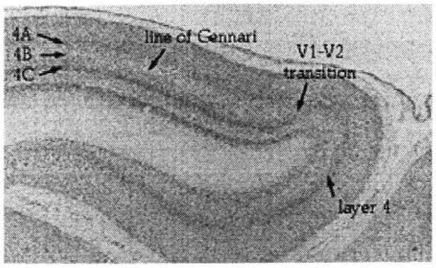

Figure 1-3: Folds of the visual cortex [51].

connectivity rather than full isotropic distribution for complexity management reasons. If each neuron were able to connect to other neurons in all three directions, then the connections would scale as N^6. Instead, by remaining mostly in the plane, connectivity is constrained as N^d, where $4 < d < 6$; the benefits of denser-than-surface connectivity are obtained, but without the full volume complexity. The layered architecture also serves the purpose of distributing specific visual processing functions to certain areas [52][53][54]. Perhaps this layered arrangement works well because typically, interesting things happen at interfaces, and more folds maximize surface area within a volume.

For the reasons of connectivity and maximizing surface area, membrane folding is attractive for 3D micro and nanomanufacturing, with particular emphasis on 3D microprocessors and integrated 3D MEMS.

1.3 Outline of the Thesis

This thesis presents a new method for micro and nanomanufacturing in 3D. In Chapter 2 we explain the design of membrane folding by first highlighting general requirements for 3D and then outlining functional requirements particular to membrane folding. Chapter 3 explains how the concepts and functional requirements developed in Chapter 2 were transformed into the first generation of working prototypes. Material selection, modelling and simulation, and the process flow and mask layout are all addressed in detail. Chapter 4 describes how we tested the first prototypes and the results, including the speed of folding and the $10\mu m$ alignment achieved after folding to 180 degrees. The design and fabrication of the second round of folding prototypes is also discussed in Chapter 4. Preliminary work on a specific kind of actuation, folding by residual stress in thin films, is presented in Chapter 5. It is hoped that residual stress may be the key to self assembling folds in parallel. We conclude with a discussion of future work and applications, with special attention given to nanostructured origami.

Chapter 2

Design of Folding Micro and Nanostructures

Undoubtedly there is much talk of building in 3D for the micro and nano regimes, both in the research community and industry. Before illustrating our approach to this technological area, it is important to frame the criteria for a successful strategy to conquer the 3D world. In this section key goals, or functional requirements, for 3D will be outlined, and many approaches will be presented as potential design solutions. The aim is to explain prior art and to highlight important technological benefits as well as limitations.

2.1 Functional Requirements of 3D Micro and Nanomanufacturing

2.1.1 Ability to Build in Three-space, Volume-wise

In order to create 3D structures, an approach must be able to create end-products with micro and nanofeatures defined within a volume. For this reason, many researchers are looking away from traditional semiconductor tools which remain planar in their function and for the most part are unsuited for creating high aspect ratio features. The major methods proposed for creating 3D microstructures are microstereolithography, two-photon lithography, interference lithography, and self assembling techniques.

In the case of microstereolithography, (μSL), complex 3D shapes are created in a liquid polymer one layer at a time [23]. A liquid polymer is spread to a thickness ranging from one to ten microns, and then a UV laser scans the surface, solidifying the exposed portions. A new, thin layer of polymer is spread and the process is repeated. In this way, a complex 3D shape can be built up by a single cross-section at time (see Figure 2-1). The benefits are aspect ratios up to 16:1, the capability to create overhung features (resembling cliffs), and the ability to incorporate "exotic" materials such as shape memory alloys and metal powders for use in MEMS actuators. However, the limitations are that vertical slices are limited to the thickness of polymer spread, on the order of several microns, and the UV beam spot size is only 1-2μm, limiting lateral resolution to an extent that impedes nanotechnology. Additionally, in this form of manufacturing, fabrication of wires and layering different materials consecutively is not possible.

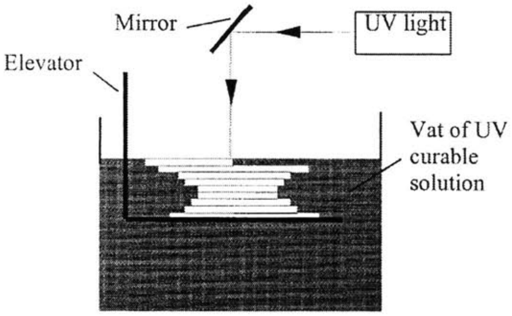

Figure 2-1: The principle of microstereolithography [23].

Two-photon methods [24] are similar to μSL in that photopolymerization is used to create structures in 3D, however the physics and functionality are very different. The polymerization is stimulated by two-photon absorption. Instead of being layer by layer, two-photon writes features with a pulsed laser, a high numerical aperture lens, and linear stages to scan the highly focused spot in three space. Compared to μSL the resolution slightly improves because the lateral feature size is limited by two-photon absorption which is proportional to the intensity of the beam. Hence, the minimum feature size is the width of the square of the point spread function of the focussed beam, around 550nm, and the depth resolution is less than a few

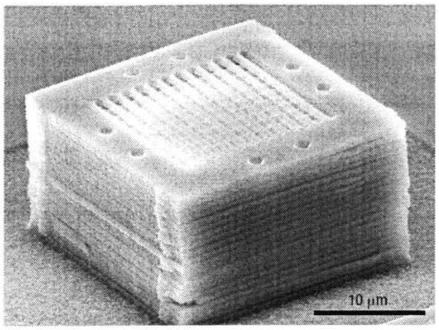

Figure 2-2: 3D photonic crystal fabricated from 2D plates [26].

microns, the beam's depth of focus. Even though this method creates interesting, previously unrealizable patterns which someday may be useful, it suffers because it is not a very general fabrication process. The set of materials is quite limited, and creating features a single point at a time in three dimensions can be enormously slow and does not scale well.

Matrix Semiconductor has pioneered 3D memory and 3D transistors with existing semiconductor technology and some advances from the flat-panel-display industry [25]. Matrix builds its 3D memory very similar to traditional 2D chips, but by stacking layer upon layer. After each thin film deposition, such as amorphous silicon or silicon dioxide, the film is chemically mechanically polished (CMP) flat to within 50 nanometers. In this painstaking process of depositing and polishing, they are successful at building eight layers of static memory. They claim that the method scales to well beyond eight layers, yet certainly errors will propagate from one layer to the next. Additionally, heat becomes a concern as the number of layers increases. Standard 2D chips already require cooling fins and fans to dissipate an average of 80 watts over a 2.2 square centimeter Pentium 4 [25]. Stacking layers upon more layers may prove impossible for thermal reasons alone, as will be described in section 2.1.4.

Another approach that falls under the layer by layer category is the very recent presentation of three dimensional photonic crystals created by assembling individual plates of 2D photonic crystals [26]. Four to twenty 2D plates are brought together and stacked with alignment tolerances of less than 50nm (see Figure 2-2). The 2D plates were fabricated with what is considered traditional semiconductor tools. The assembly is guided by polystyrene microspheres that are inserted into etched pores on each plate. Thus the pores and spheres essentially act

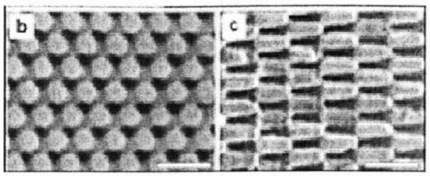

Figure 2-3: 3D photonic crystals in SU-8 resist created using holographic lithography [57].

as kinematic couples, though the details of the coupling are still somewhat unclear so it is difficult to say whether it is an exact constraint or an elastically averaged constraint. The plates are assembled with the aid of a custom micromanipulation system inside of a scanning electron microscope (SEM). The plates bond to each other permanently when pressure is added to the stacked array. Although this method seems very promising, especially considering the alignment reported, it still suffers a major drawback in that the assembly is extremely time consuming since each plate is handled individually, and manually assembled.

3D photonic crystals have also been produced by holographic lithography techniques [57]. Using four non-coplanar lasers the researchers are able to expose a $30\mu m$ layer of SU-8 resist with an interference pattern which results in a sub-micron periodic structure in 3D (Figure 2-3). The regions of resist that experience the maxima of the interference pattern are exposed and become insoluble. The rest of the polymer is washed away by the developer solution. The interference technique is especially adapted to creating photonic bandgaps because it can only create periodic structures. However, this is also a sever limitation because it cannot be a general purpose tool for building in 3D.

In a very radical approach to the problem of filling 3D space, George Whitesides' group has developed self-assembly techniques for creating 3D mesostructures based on shape complementarity and the hydrophobic effect [27][28][29]. In this work they have created simple, 3D, operational electrical circuits. Regularly shaped polyhedra with chemically treated side walls are attracted to each other in an aqueous solution, self align due to minimum energy principles, and then bond once the temperature is raised to a threshold. One limitation in this method is that the assembly is random because it takes place in a solution. Additionally, only ordered, periodic 3D structures assemble, therefore there is little freedom in the final shape of the device.

As an alternative to the methods presented above, membrane folding has all the benefits and none of the limitations. The fundamental advantage is independence between the fabrication process and 3D assembly. In this manner it is possible to utilize all of the existing technologies, even the ones presented above, and incorporate any new advances.

2.1.2 Connectivity in Three Dimensions

Whether the final application is 3D electronics or robust 3D MEMS sensors and actuators, the ability to communicate between devices is essential to the functioning of the system. In 3D electronics issues such as latency become crucial to the performance of the system. In MEMS and nanotechnology, the sensors and actuators must be connected to power supplies and data channels leading to memory or controllers. The challenge then becomes how to connect discrete elements located in three-space in the most efficient manner.

An extreme example of connectivity is Intel's Pentium 4 processor. It is an eight layer device in which the first layer houses all of the active elements for computing. The additional seven layers form a nest of wires that connect all of the active elements. The first level is semiconducting single crystal silicon, and the upper layers are mostly dielectric films with the embedded circuitry [25]. The architecture follows a basic pattern of in-plane circuitry on discrete levels connected by vertical vias.

An alternative for 3D connectivity is simply allowing connections to take place in all three dimensions simultaneously. However, this is not a very good approach based on complexity arguments. In a cube with N^3 elements, an isotropic distribution of connections goes as N^6, compared to N^2 elements and N^4 connections within the plane. Thus it seems that an anisotropy of interconnects may in fact be more efficient and simpler than a full isotropic distribution. If most of the connectivity is confined to within planes and only sparse communication goes vertically between planes, then the system is more organized, and from a practical standpoint, easier to design and simpler to build. Perhaps one way to better organize a Pentium would be to distribute the active elements to various levels in such a way that components that must talk with each other frequently are closer to each other on a particular level. Routes of less frequent communication would exist in the vertical direction between layers. This follows the architecture of the visual cortex (it should be noted, however, that the visual cortex is quite specialized in its functions whereas the Pentium is designed to be a general purpose processor). As mentioned earlier, biological nature seems to follow a design rule of folding layers on top of each other, physically structuring anisotropy. As is true with the primary visual cortex, most information flows within planes and across folds, but in addition, signals pass across adjacent layers but to a much lesser extent. If the Pentium were laid out in an architecture more similar to the visual cortex, it would be built on a long ribbon-like 2D membrane. Most connections would take place within the plane of the membrane. This 2D sheet would then be folded over on itself to make it more compact, but also to permit shorter routes between key areas where latency is critical. Connectivity would be maintained through the folded areas, and additional connections in the vertical direction would be established for communication in between adjacent planes. Membrane folding achieves maximal connectivity because connections exist within each plane, around each fold, and between planes by means of vertical vias. Above all else, 3D presents an access problem, and membrane folding is the solution.

2.1.3 Low Cost

For a new technology to gain market acceptance there must be sufficient reason to make a change. Often times new functionality is the primary motivation, followed by lower cost, in terms of capital investment, development, and production. However, even if a new technology surpasses all others in performance by orders of magnitude, high costs will be a barrier to entry. Radical changes to machinery or processes is also a severe hurdle because it is very difficult to change the momentum of industry. For this reason, disruptive technologies with a paradigm shift often times have to be extremely less costly to gain entrance and acceptance.

Matrix Semiconductor and Aoki's 3D photonic crystals are attractive prospects for a new 3D micro and nano technology because they extend the capabilities of current microfabrication tools. In terms of capital investment, there is a smoother integration because existing foundries already have the machinery and knowledge base for processing such devices. For similar reasons, development costs are also held lower because these fabrication methods have been well characterized over the last few decades. However, in terms of production, neither layer by layer construction is very fast.

Membrane folding is attractive because it also seeks to use existing microfabrication tools.

Additionally, due to the decoupled nature of the fabrication and 3D assembly, development costs are reduced because new advances in micro and nanotechnology can be developed independently and then integrated with ease. Membrane folding is also fast because it does not involve individual manipulations of components.

In terms of product development, membrane folding saves time and money. Complete mask sets cost millions of dollars. In a layer by layer type process, each level requires its own set of unique masks, and so the cost of the complete mask set will scale directly proportional to the number of layers. Membrane folding, on the other hand, only requires a single mask set no matter how many layers are to be built. This is because all of the device fabrication is done in the first step along one continuous 2D membrane in the plane of the substrate. Thus, all levels are patterned at once, saving time and money.

2.1.4 Adequate Heat Dissipation

An important consideration particular to 3-D devices is heat dissipation. As devices expand into the 3^{rd} dimension and increase in volume, the relative amount of surface area decreases, and removing heat becomes more difficult. The severity of the problem becomes apparent when one realizes that contemporary microprocessors have power densities greater than the average stovetop burner [25]. And as new generations of wires continue to have smaller cross sectional areas, and more wires are packed closer together, Joule heating will present some significant challenges to chip designers. One strategy for dealing with heating includes shutting off portions of a chip to let them cool. However, this dramatically limits performance.

Looking at biology again, the human brain is cooled by circulating fluids. Even though it is much more massive than a microprocessor, it generates only 25 watts, whereas the Pentium 4 in its 2.2 square centimeter package dissipates 80 watts [25].

Layering techniques, such as Matrix Semiconductor's may suffer from the consequences of heat generation because of the dense packing of vertical layers. Membrane folding, on the other hand has the benefit in that its folded structure can be tuned to accommodate spacings between layers. This architecture when viewed from the side looks much like a radiator (see Figure 2-4). It is true that other layering techniques could use deposited sacrificial material which could be etched away to create a similar radiator geometry. Yet sacrificial materials are

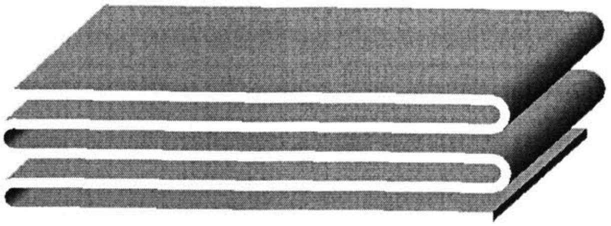

Figure 2-4: Membrane folding creates a structure resembling those commonly used in radiators.

at a very high premium because due to selectivity issues there are few combinations that work well and thus they are often reserved for more important uses. Forced convection by means of blowing air or pumping a dielectric fluid through the spacings created by membrane folding is an ideal solution for the anticipated heat dissipation problem.

Beyond aiding thermal management, the radiator style of architecture of membrane folding can be useful for other applications where maximal surface area in a small volume is desirable. For example, in biological or chemical assays and micro fuel cells it may be advantageous to have a large surface area treated with a particular kind of reagent.

2.1.5 Scaling

The evolution of homes and offices may serve as an important lesson for the future of micro and nanosystems. Buildings began as a single level covered by a roof. But as real-estate became less available or at least more costly, the only logical way to gain more living space was to build upwards. Most single family homes are still wider than they are tall, however in areas where real-estate is expensive or where the population density is enormous, such as in geographically confined cities such as Manhattan and Hong-Kong, the buildings are taller than they are wide. Transportation distance and time are also reduced in cities with a vertical tendency, especially Los Angeles, which is spread out, compared to New York.

This just might be the case for microelectronics, MEMS sensors and actuators, and nanodevices over the next decade. The number of active elements squeezed into a planar chip is ever increasing and the demand for smaller consumer electronics will probably never be satiated. These competing demands necessitate the building of 3D devices just as skyscrapers have come to dominate the urban landscape.

Layer by layer methods and microstereolithography appear to be scalable to many layers. Matrix has demonstrated twelve layers, Aoki's 3D photonic crystals demonstrate up to twenty layers, and microstereolithography seems as though it can scale indefinitely as long as the z-axis stage has enough travel (with enough precision). Yet in the methods where layers are grown directly upon one another it is possible that a defect in one layer could propagate throughout the rest of the vertical layers. The 3D photonic crystals and membrane folding have an advantage in that each layer is created on the same substrate so that errors in one level do not contaminate another, and furthermore, all of the features are fabricated within a single mask so that scaling to multiple levels is not impeded by the cost of having unique mask sets for each level. In the case of membrane folding, if each crease contains its own source of actuation, there is no limit to the number of membranes that can be folded.

2.1.6 Platform Compatibility with Microelectronics, MEMS, and Nanosystems

A successful platform for 3D micro and nanomanufacturing must be flexible and as general as possible to accommodate the vast applications, materials, and fabrication methods of the micro and nano worlds. There exists no standard micro or nano fabrication process. Some devices are created with standard silicon processing, some use exotic III-V substrates, and still others use soft lithography and other non-standard fabrication means. The beauty of membrane folding is that the fabrication is decoupled from the assembly. Any existing method or future developments in lithography or other processes are easily integrated into folding. The fabrication takes place just as it would on a typical planar substrate and then it is assembled into a compact 3D geometry in which more connections may be made. Other proposed 3D methods lack this flexibility, largely because they are new fabrication methods attacking 3D directly. The decoupled nature of membrane folding also allows integration of logic circuitry and sensors to be combined adjacent to one another even if the fabrication methods are very dissimilar. And techniques such as flip chip solder bonding can be used to assemble different MEMS and CMOS components onto various membrane flaps before the folding process takes place [42]. Some nano applications use extensive surface chemistry (for example, creation of nucleation sites) which will not stand up to the rigors of other layer by layer fabrication methods as they coat one layer directly by the next, possibly destroying fragile chemistry before it is utilized.

Many concepts for fabricating 3D micro and nanostructures have been proposed in the literature and reduced to practice. However, they struggle to meet all of the functional requirements for a successful 3D methodology. Membrane folding, on the other hand, presents a flexible platform for seamless integration of many types of micro and nano fabrication into dense volumes. The folding process does not impede material selection or exotic fabrication requirements. Folding surpasses all other approaches in terms of 3D connectivity and heat dissipation. Development costs are reduced by fewer masks and parallel fabrication of multiple layers. Capital investment remains steady state as no new tools are needed, yet membrane folding does not impose any limits on new fabrication techniques. For example, all of the other 3D methods presented, such as microstereolithography, layered methods, and surface chemistry techniques are easily incorporated into the folding process.

2.2 Functional Requirements of Membrane Folding

We decompose membrane folding into five main functional requirements, or goals that must be satisfied to meet the needs of some future applications. The functional requirements are hinge, actuation, connectivity, alignment, and latching. There is a large body of work from the MEMS and semiconductor fields that relates to these aspects, and they are presented below.

2.2.1 Hinge

Perhaps the most obvious way of making a hinge capable of large rotations is to miniaturize macroscopic hinges. Mechanical rotating joints have been fabricated as depicted in Figure 2-5 [30]. Many of these hinges in combination with one another define only one degree of freedom for a group of plates. Just as in a pop-up story book, when one flap is turned all the other plates fold into a final position as depicted in Figure 2-6. While some incredibly intricate folded structures have been fabricated, there is a severe limitation in that the actuation is manual, typically by using a probe tip to fold the structure.

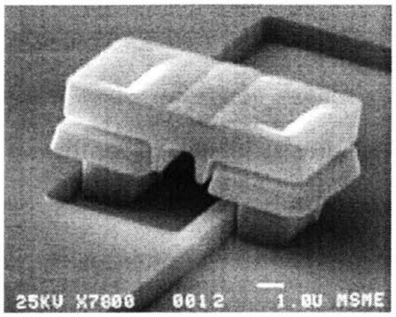

Figure 2-5: Berkeley hinge structure [30].

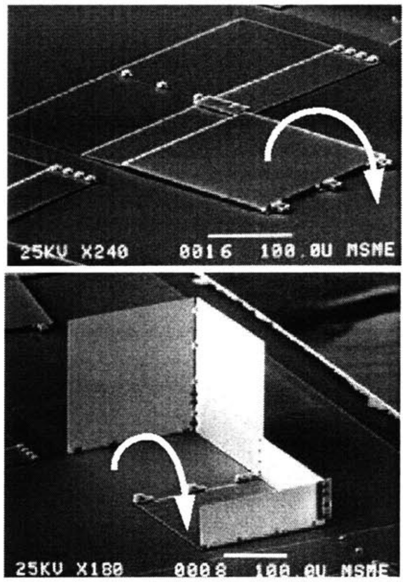

Figure 2-6: Berkeley hinges and linked flaps of silicon [30].

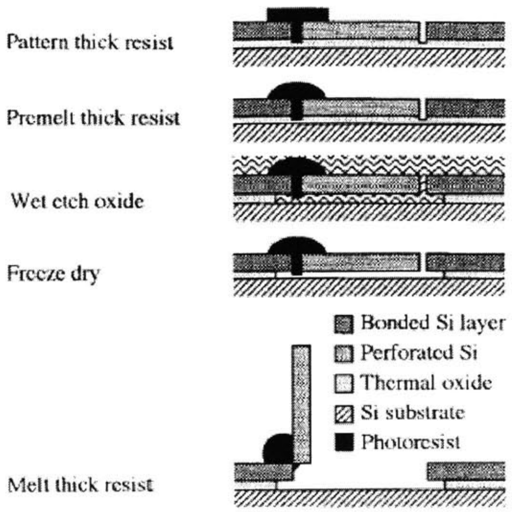

Figure 2-7: Photoresist as hinge material [31].

Photoresist joints have also been proposed for rotating silicon micro flaps. Squares of photoresist are patterned between independent segments of silicon. Upon release of the flaps from the substrate, and subsequent heating of the photoresist, the flaps rotate out of the plane. This happens because the surface tension of the photoresist clings to the flaps, and as the photoresist melts it attempts to reach a minimum energy state by becoming round (see Figure 2-7).

Flexible circuits are commonplace in laptop computers. Typically, these circuits are fabricated on polyimide, a soft, flexible polymer which achieves the highest wiring density and for that reason is an industry standard [58]. The largest application of flexible circuits is in interconnects between chips on circuit boards, which have large radii of curvature. Yet some research has shown that polyimide can be used as micro-hinges for micro-robot applications [59]. These polyimide micro-hinges are bent to ninety degrees, and thus demonstrate that polyimide sustains tight curvature. It still remains to be seem whether polyimide will fold completely to 180 degrees and how embedded wires will affect the mechanics of folding. Other materials such as the insulating polymer benzocyclobutene (BCB) and mylar should also be investigated.

The use of plastically deformed metals as hinges has been demonstrated by two different

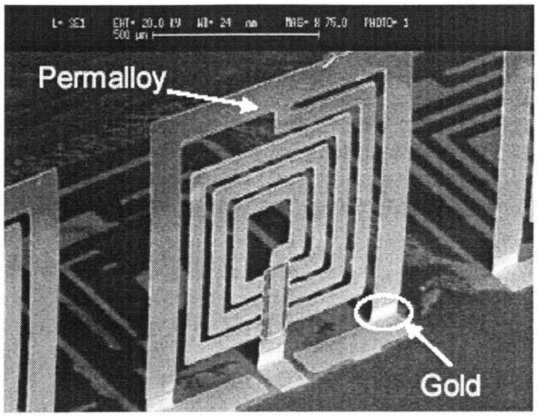

Figure 2-8: Vertical inductor created through PDMA process [18].

research groups [18][19][32][33][34]. The concept is to fold a thin metal film to the point where it begins to plastically deform. Upon further bending any plastic deformation results in permanent strain so that the hinge remains bent. The University of Tokyo's group is primarily interested in new kinds of MEMS actuators for micro-positioning stages, particle movers, and insect wings. These actuators are no more than loops of wire actuated by a Lorentz force. At the University of Illinois, the Plastic Deformation Magnetic Assembly (PDMA) process was developed for creating out of plane structures such as planar spiral inductors as shown in Figure 2-8. Gold hinges are bent beyond the yield point and the result is a free standing, vertical structure.

Similar to folding hinges, but still quite different, is the idea of a four bar lift which is depicted in Figure 2-9. Essentially just four metal hinges attached to a plate, the rotation out of plane results in stacked parallel plates. Yet this type of hinge lacks the ability to form vertical connections between plates, and it does not scale very well.

A common grievance among the MEMS community is the negative effect of residual stress. Often times the inherent stress in a thin film due to deposition conditions is enough to ruin a device. For example the free-standing grating shown in Figure 2-10 snapped and curled due to too much stress in the thin films. The PZT actuated cantilever depicted in Figure 2-11 is curled up not due to an applied voltage potential as intended, but due to the residual stress in the multiple films. Thus, this is the equilibrium position of the cantilever which is completely

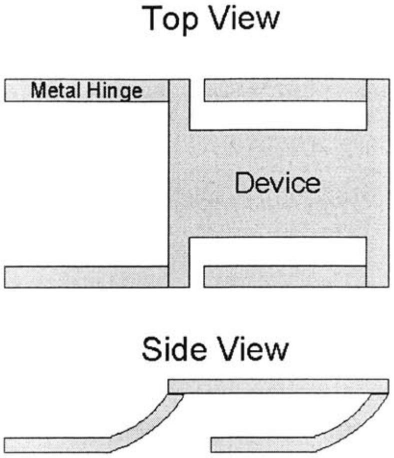

Figure 2-9: Schematic of four-bar lift concept.

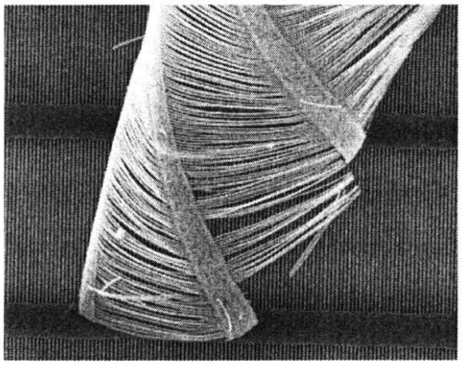

Figure 2-10: Silicon nitride grating curled due to residual stress [37].

undesirable for the intended application. However, as undesirable as this may be for some uses, it is ideal for membrane folding. If the residual stresses can be engineered correctly, massively parallel and completely self-assembling folds will be realized. At the present time, there does not appear to be any such work being done in the research community.

2.2.2 Actuation

There is an intimate relationship between the hinge and method of actuation. The actuation must be compatible with and capable of folding the selected hinge. The actuator ideally will also have a small footprint, scale to many folds, and remain relatively non-complex to fabricate

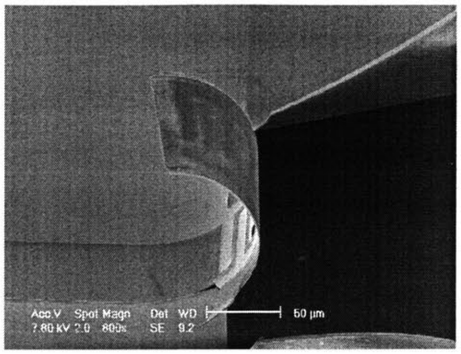

Figure 2-11: PZT actuated cantilever bent by the forces of residual stress [36].

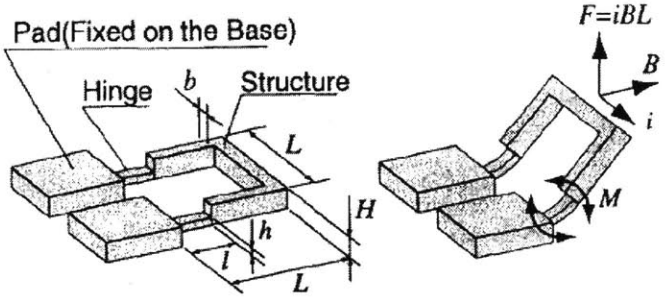

Figure 2-12: University of Tokyo's Lorentz force actuator [32].

and control.

In the case of plastically deformed hinges, the University of Tokyo and the University of Illinois chose very different means of forcing the bends. In the former, the Lorentz force was used by flowing a current trough a wire in the presence of an external, perpendicular magnetic field (Figure 2-12). The Lorentz force has the benefits of being highly controllable (adjusting current levels), addressable, directional (reversing current direction changes the sign of the force), and highly compact because it only requires a wire.

In the PDMA process, a permalloy (magnetic material, typically a combination of electroplated nickel and iron) is patterned on the hinged flap so that when an external magnetic field is applied, the permalloy experiences a torque up until the shape anisotropy is aligned with the field (Figure 2-13). The benefit of using permalloy is the large force produced, typically three

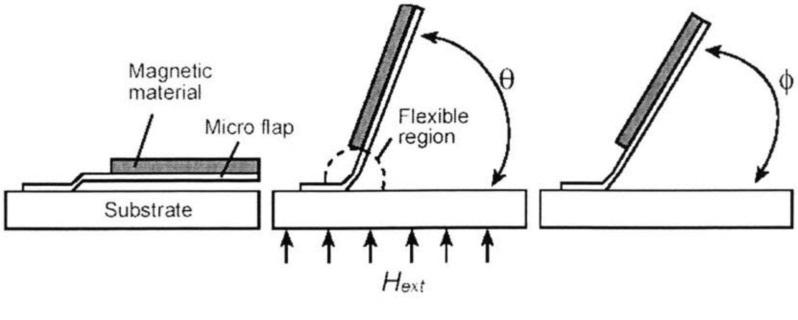

Figure 2-13: The PDMA folding process, side view [18].

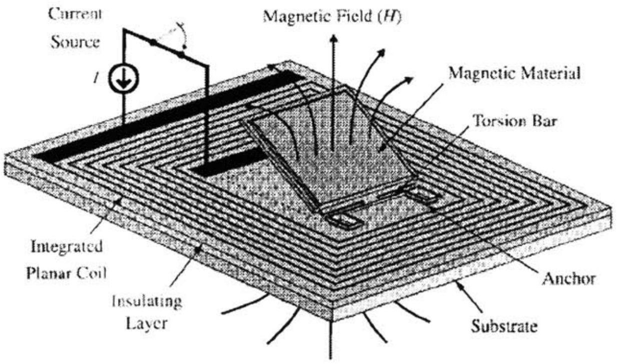

Figure 2-14: Permalloy actuation by integrated coils [38].

orders of magnitude greater than that from the Lorentz force. The permalloy scales well to multiple folds, however it has a large footprint occupying much of the flap which renders the surface unusable. Additionally, there is no on or off switch meaning that all the devices on a wafer will be actuated simultaneously. A slight variation of the PDMA process is earlier work conducted by Jack Judy in which the magnetic field is generated on chip by microfabricated coils [38][39]. The motivation for integrating coils is so that the device is a self-contained microactuator for scanning mirror positioning. However, as attractive as this may be, it requires an enormous footprint not ideal for 3D fabrication with multiple folds (Figure 2-14).

Flipping Judy's design around, one could also fabricate coils on the flap, and then in the presence of an external magnetic field the dipoles would self-align and rotate the flap out of the page. For thirty coils the generated torque would be about half as much as the permalloy methods, which is quite strong. However, the inclusion of coils around the flap increases the complexity of accessing any internal component with other wires, which would add additional masks to the fabrication process.

The surface tension method using photoresist bumps presented earlier is an example of a coupled design where the hinge and actuation are inseparable. From the axiomatic design point of view [40], this is a suboptimal design. However, thermal actuation is highly parallel and could be good for mass production.

Bilayers can also be used for folding. It is commonly learned in mechanical engineering that a bimetallic strip composed of two metals with dissimilar thermal expansion coefficients will curl upon addition of heat. Due to the strain mismatch, the linear displacement of each layer is redirected into bending. A variation of this theme is electrochemically driven polypyrrole bilayers [41]. Polypyrrole is a conjugate polymer that exhibits electrochemically controlled volume. Upon the application of a voltage, the material absorbs ions resulting in volume changes on the order of a few percent (compared to PZT actuators with 0.1% strain). It has been demonstrated that polypyrrole on gold forms a high force, large motion hinged actuator. At the present time this actuator must operate in an aqueous environment as it needs a source of ions readily accessible. Additionally, research has shown that lattice mismatched epitaxial layers result in bending [60]. This method has produced angles of 25 degrees and radii of curvature smaller than $50\mu m$.

Following the bilayer theme, residual stress in thin films is also suited for initiating large degrees of bend with high forces. Using residual stress is another example of a coupled design because the thin films serve both as the hinge material and the source of actuation.

Due to the large range of motion, electrostatic means are not feasible as their force quickly falls off with distance ($\sim 1/r^2$). Some other methods of actuation are hydrodynamic and vibratory assembly. Hydrodynamic has been referred to by the Berkeley hinges [30] because upon releasing the plates from the substrate in a liquid etchant, some of the structures stood on end. This is highly stochastic and thus not suitable for a marketable device or repeatable process.

2.2.3 Connectivity

One of the key features of membrane folding is the ability to run electrical connections through the hinged regions in addition to vertical vias created upon the completion of the folds. Extending a chip's circuitry across the folded regions essentially results in one very long 2D chip. References [18][19][32][33] and [34] have already demonstrated that it is possible to fold thin metal films, and [59] has shown that polyimide thin films can be folded to 90 degrees. Thus it seems that in principle it would be possible to fold many wires encased in a flexible polymer (to prevent shorts) in order to transform the long 2D chip into a dense 3D structure.

In terms of establishing vertical connections, there exist many options. Perhaps the best is a variation of flip-chip solder bonding, a very common and well characterized industrial process which is also starting to be used in the MEMS field for building hybrid systems with sensors, actuators, and control electronics without the arduous task of monolithic integration [42]. In this particular example, compression, rather than heat, initiates the solder bonds between components. This method could also be used to assemble logic, sensors, and nanostructures, all of which were fabricated on separate wafers, along one continuous membrane to be folded later.

In a similar vein, electroplated posts as well as metalized thin film flexures could serve as points of vertical connection. Some degree of compliance is needed to ensure massive and repeatable connectivity across the surface of a membrane flap. For example, a three legged stool is often times more stable than a four legged version. Three points exactly define a plane, therefore more than three points of contact means that all the contact points must be exactly matched along the plane. This is either difficult or impossible to manufacture depending on the specified tolerances. Compliance ensures that contact will be made despite nonuniformities.

Connectivity is not limited to electrical signals. Optics presents tremendous opportunity for increased functionality and performance. Steps are being made toward using integrated optics to distribute clock signals and other time-critical signals throughout a chip using waveguides and free space optics. In the case of membrane folding, arrays of vertical cavity surface emitting lasers and photodiodes establish communication links in the vertical direction between layers (Figure 2-15). Folding opens the possibilities of new chip configurations such as the cube geometry depicted in Figure 2-16 which would enable optical signals to be broadcast to a large number of sites using just one source. Additionally, optical interconnects enable higher bandwidth and throughput by strategies such as wavelength multiplexing.

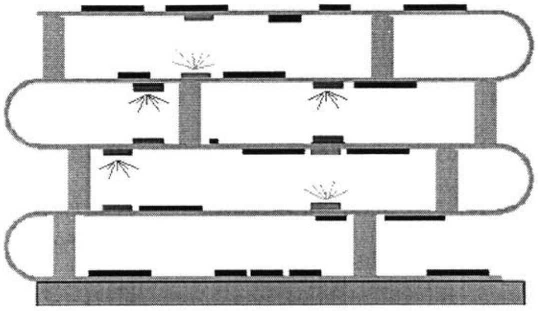

Figure 2-15: Electrical and optical interconnects between layers oriented in the vertical direction.

2.2.4 Alignment

Proper placement of the folded membranes with respect to one another is very important, especially if physical connections are to be made between layers or if optical elements need to be positioned within specified tolerances in order to function properly. Kinematic couples and elastic averaging are two techniques that have been borrowed from the macro world and implemented on the microscale. Kinematic couples are a form of exact constraint design, where the number of contacts equals the number of degrees of freedom being constrained [43]. Typically, this involves grooved structures mated with concave geometries. Aoki's 3D photonic crystals present an example of kinematic couples formed by polystyrene microspheres placed into precisely etched holes [26]. It is reported that the alignment is on the order of 50nm, yet the design seems to be overconstrained because each layer has eight microsphere and pore couplings. Flexural kinematic couples and elastic averaging take advantage of compliance in order to achieve repeatability and accuracy, and have been demonstrated as methods for aiding wafer to wafer alignment [44].

Electrostatic alignment is a novel approach that has not been seen in the literature. The concept is to use electrostatic attraction to pull a structure into alignment by creating potential wells.

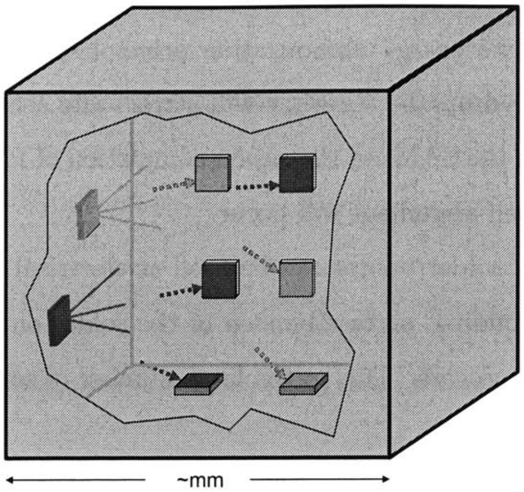

Figure 2-16: Cube formed by folding membranes. Optical interconnects broadcast signals in free space to many photodetectors located inside the cube. Microelectronics could be located on the outside of the cube [55] [64].

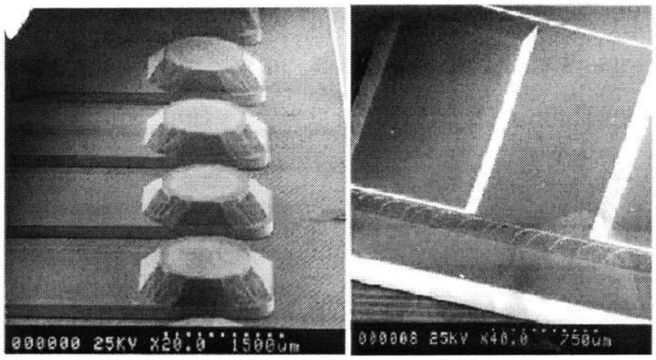

Figure 2-17: Microfabricated kinematic couples for wafer to wafer alignment. Bosses and grooves shown [44].

Surface chemistry has been used to demonstrate alignment tolerances on the order of $0.2\mu m$ and angular misalignment of less than 0.3 degrees for assembly of microparts [45][46][47]. Self-assembling monolayers (SAMs) that are patterned on a substrate establish hydrophobic and hydrophilic areas. Due to energy minimization principles, areas with similar geometry and similar hydrophobic or hydrophilic tendency will attract and self-align. One idea is to pattern the membrane flaps with the SAMs so that upon completion of folding, the patterned areas will be in contact and then self-alignment will occur.

As mentioned before, solder bumps can be used as electrical connections. However, in the case of thermal solder bonding, surface tension of the solder on the metallic bond pads tends to self-align the bonding process. Due to the large number of solder bumps, it becomes a form of elastic averaging.

2.2.5 Latching

Mechanical latches have been implemented in the micro world for MEMS applications [35][31]. Microwelding has also been proposed as a method of securing microstructures [48], and it could be an almost natural continuation of electrostatic alignment techniques. An extension of the surface chemistry alignment is to include an adhesive after coating the SAMs that is either activated by ultraviolet radiation or by thermal means [46]. Perhaps one of the most novel ideas is to use stiction. Typically, stiction is something to be avoided when releasing a MEMS device, however it has been used to fasten devices once they are positioned by electrostatic scratch drive actuators [49]. Finally, solder bumps obviously are also a means of securing components aside from their roles in electrical connections and alignment.

2.3 Design Selection

After surveying the literature and brainstorming concepts for 3D structures based on membrane folding it was determined that the best approach for a proof of concept was to implement plastically deformed metals as hinges which are actuated by a Lorentz force. The first task was to demonstrate folding of a single membrane to 180 degrees. Plastic deformation of thin metals seemed ideal because of the simplicity of design and the fact that once plastic deformation begins the hinges will stay permanently bent at a new equilibrium position so that latching could be put off until later design iterations. The Lorentz force was chosen largely because the magnitude of force is easily controlled which makes studying the mechanics of folding much easier. However, in the future, the Lorentz force will most likely be replaced because it does not scale as well as other methods. For this reason we have also made preliminary steps toward characterizing folding by engineered residual stress in layered thin films. The Lorentz prototype is depicted in Figure 3-2 below, in its most basic rendering.

Chapter 3

Prototype Design and Fabrication

Having converged upon a conceptual design for the first prototype using plastically deformed metal hinges actuated by a Lorentz force, a more detailed design with proper dimensions and a logical process flow came next. The mechanics and dynamics of folding were simulated to ensure that sufficient force would be generated to fold and plastically deform the hinges to 180 degrees, with sufficient alignment tolerances. The fabrication process flow presented some specific challenges which were met and overcome. The end result was a device that successfully folded to 180 degrees using less current than predicted and achieved a final lateral positioning alignment of 10 microns.

3.1 Material Selection

The first prototype was meant to be a simple proof of concept demonstrating the folding principle. Thus it sought to fold a planar membrane by 180 degrees and bring it either into contact or parallel with the wafer substrate. Bending to 180 degrees requires a ductile material in order to support large amounts of plastic deformation without failure. A small minimum bend radius and minimal spring back angle are needed so that once the fold is made it will remain fixed near the final angle of bend. Current must flow through the hinges, and so it is necessary to select a material with low electrical resistance and high thermal conductivity to avoid melting the hinges upon actuation.

The set of materials available for use in the cleanroom include Al, Au, Cu, Cr, Ti, and

Material	E (GPa)	σ_Y (MPa)	σ_u (MPa)	ρ (kg/m^3)	k (Wm^{-1}k^{-1})	Crystal Structure [62]
Al (film)	70	124	176	2700	237	FCC
Au (bulk)		206 [18]	250 [20]	19280	315	FCC
Au (film)	80					FCC
Cu (bulk)	128	100	220 [20]	8960	398	FCC
Cu (film)		262	310			FCC
Cr (film)	140					BCC
Ti (film)	110					HCP

Table 3.1: Material properties of cleanroom metals.

many other exotic metals. Table 3.1 lists the most important parameters for the leading material choices (the more exotic material were avoided for the first prototype due to a lack of information about their mechanical properties as thin films). Values were obtained from the MEMS Clearinghouse Material Database [17] unless otherwise noted.

Bulk values from the macro world do not always accurately describe the nature of mechanical properties on the micro scale. It has been reported that down to around $10\mu m$ bulk values may suffice, yet below this length scale material properties such as Young's modulus can vary substantially from the bulk values [4]. Moreover, the values for the microscale often times are dependent upon the method of deposition. Whenever possible material properties specific to thin films have been used from the literature.

The hinge material should have very little springback after the bending force is removed so that the membrane remains very close to the maximum angle. Even though Al can be folded over on itself without failure, it has an enormous springback angle. It is for this reason that automobile bodies are not stamped of Al but steel [62]. Due to the comparatively high spring back angle, Al was ruled out as a possibility for hinge material.

Copper wires were used in the University of Tokyo's Lorentz force actuator, and Cu has extremely competitive values for the yield stress and thermal properties. Yet Cu was avoided as a potential hinge material because it was thought that a permalloy might be electroplated onto the flap. This requires a Cu seed layer which would eventually be etched away. Therefore it did not make sense to build hinges from copper from the standpoint of process flow.

Body-centered cubic (BCC) crystals present the highest ductility because they have a higher number of slip systems allowing more plastic deformation before fracture than other structures. Face-centered cubic (FCC) follows BCC structures in terms of ductility, and hexagonal close-packed (HCP) are typically quite brittle at room temperature [62]. Titanium is an HCP, and so it was avoided because it would have cracked during the extreme degree of bending required by folding. Cr is the only BCC metal in Table 3.1, however, due to extremely high residual stress (on the order of 1GPa for a 200Å thick layer) it was decided that Cr should not be the primary hinge material because it could introduce warping and other parasitic effects.

Gold was chosen as the hinge material because it possesses the best combination of mechanical properties for the folding application. The one difficulty of using gold is that it is not considered CMOS compatible because Au atoms, as well as Cu, are capable of diffusing throughout a wafer and can lead to shorts in electrical devices. A wafer is considered "gold contaminated" once it contains Au or Cu, or simply has been in a machine that has had Au or Cu wafers in the past. Thus, aside from the stigma of being "gold contaminated" or a "dirty process," using gold prevents one from using a large set of machines in the cleanroom and it needs to be taken into account when designing a successful process flow.

Gold and copper would then seem to be poor candidates for eventual use in 3D microelectronics created through folding. However, leading microprocessors currently use copper as interconnects in time-critical circuits due to the high conductivity of copper. In these circuits a diffusion barrier of Tantalum prevents the spreading of copper atoms. Since our first prototype contains no sensitive electronics we do not need to take the pains to create a diffusion barrier, yet it is important to know that one exists, and that what we are doing is applicable.

Au does not adhere well to Si. For this reason a thin layer of either Cr or Ti is used to promote adhesion. As mentioned earlier, Ti is too brittle for folding, and so Cr was used as the adhesion layer.

Future plans call for devices to be built on the membranes, such as electrical networks, Fresnel zone plates, and microfluidics. Thinking ahead, we wanted to include a tunable grating developed by one of our colleagues [3]. This set the initial size of the membrane to be $500\mu m$ by $500\mu m$, large enough to house this particular device in the second round of fabrication. In addition to the size of the flap, inclusion of the tunable grating required that the substrate be a $10\mu m$ thick silicon on insulator (SOI) wafer.

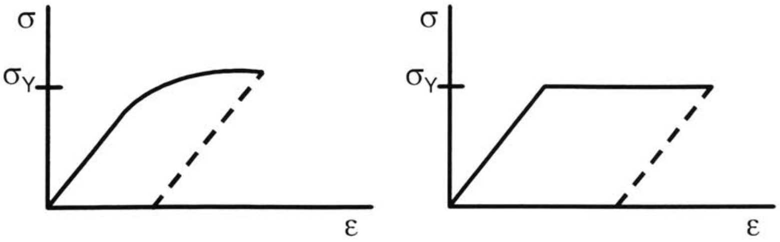

Figure 3-1: Stress-strain curves for real (left) and elasto-plastic material (right).

3.2 Modeling and Simulation

3.2.1 Mechanics of Folding

The choice of a material allows for the optimal dimensions of the hinge to be calculated based on the material properties. For the sake of modeling the first prototype, it is assumed that Au behaves as an elastoplastic (or elastic-perfectly plastic) with stress-strain curve as depicted in Figure 3-1.

There are three major parameters to set; the length, thickness, and width of the hinges (see Figure 3-2). Assuming constant radius of curvature the length of each hinge determines the final spacing between the membrane and substrate. Three target stand-off spacings of 20, 30, 60μm were chosen, and thus the corresponding lengths are 30, 50, and 100μm.

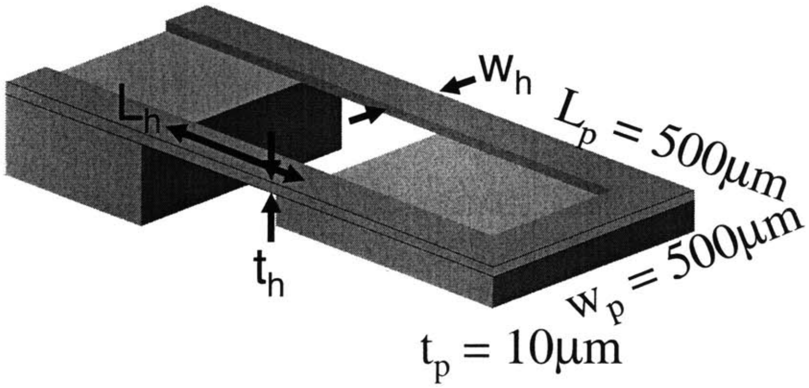

Figure 3-2: Solid model representation of the first prototype design using Lorentz force actuation.

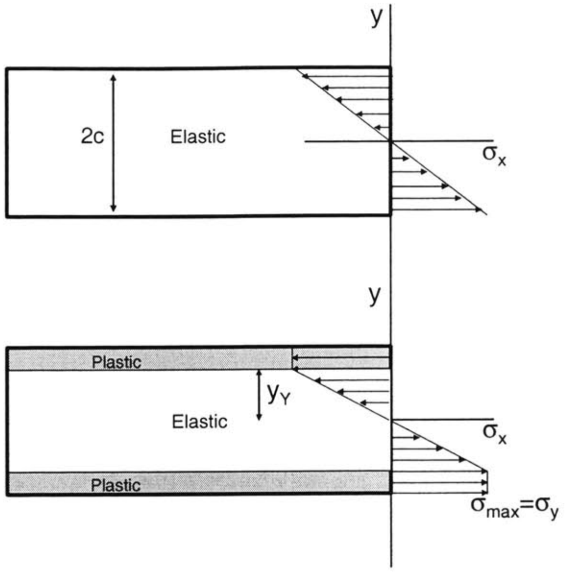

Figure 3-3: Reduction of elastic core as plastic deformation progresses.

In pure bending during the elastic regime, the radius of curvature is given by $\frac{1}{\rho} = \frac{M}{EI}$ where ρ is the radius of curvature of the bend, M is the applied bending moment, E is Young's modulus, and I is the moment of inertia about the neutral axis. Under these conditions Hooke's law applies such that the stress is linearly distributed across the thickness of the beam with a maximum stress of

$$\sigma_{\max} = \frac{Mc}{I} \tag{3.1}$$

where c is the half thickness of the beam and $I = (1/12)w_h t_h^3$ for the rectangular cross section of the hinge.

Under the assumption of Au behaving as an elastoplastic, the required bending moment will continue to increase up until yield occurs, and then the moment required to continue bending remains constant. This elastoplastic and constant bending moment approximation is easily justified because it serves as an upper bound. After the onset of plastic deformation, an elastic core of half thickness y_Y remains. The relation between the required bending moment, the elastic core thickness, and the total thickness $2c$ is given by

$$M = \frac{3}{2}M_Y(1 - \frac{1}{3}\frac{y_Y^2}{c^2}) \tag{3.2}$$

where M_Y is the maximum elastic moment. As the beam continues to plastically deform, y_Y approaches zero and the required moment to further deform the beam increases to a limiting value of

$$M = \frac{3}{2}M_Y. \tag{3.3}$$

M_Y is found by substituting in the yield stress, σ_Y, into equation (3.1) so that the maximum moment required to fully plastically deform a beam is given by

$$M = \frac{3}{2}\frac{I}{c}\sigma_Y. \tag{3.4}$$

In theory, this is the maximum moment required to bend the hinges to 180 degrees. It is impossible to fully plastically deform a beam in pure bending due to the discontinuity of stresses at the neutral axis. Thus, y_Y never reaches zero and equation (3.4) serves as an upper limit of the torque required to completely deform the hinge.

Further substitution of the moment of inertia for a rectangular beam reduces equation (3.4) to the maximum required bending moment

$$M_{req} = \frac{wt^2\sigma_Y}{4}. \tag{3.5}$$

An order of magnitude estimate for the required bending moment is found by assuming there are two hinges on the order of $50\mu m$ wide and $0.5\mu m$ thick: $2(50\mu m)(0.5\mu m)^2(206Mpa)/4 = 1.3 \times 10^{-9}Nm$.

The force of gravity due to the small mass of a single flap measuring $500\mu m \times 500\mu m \times 10\mu m$ is insignificant when compared to the force required to plastically deform the hinges. The mass of the flap is $5.8 \times 10^{-9}kg$, resulting in an approximate torque about the hinges of $T = 250\mu m \times 5.8 \times 10^{-9}kg \times 9.8m/s^2 = 1.4 \times 10^{-11}Nm$, two orders of magnitude less than the required moment for plastically deforming the hinge.

The Lorentz force is modeled as $F = Li\hat{}B$, where "^" denotes the vector cross product of the current, i, and the magnetic field, B. Due to the experimental setup we can assume that the external magnetic field can be aligned perpendicular to the wire loop embedded in the membrane. Thus the force acts along the section of wire that is perpendicular to the magnetic field, and no force is generated along the length of the wires that lie parallel to the field. In this case the length of the wire, L, is equal to the width of the plate, w_p. As the membrane begins to fold by angle θ, the applied torque attenuates by $\cos\theta$. Thus the applied moment is modeled as

$$M_{app} = i w_p L_p B \cos\theta. \tag{3.6}$$

Once the device is fabricated, the applied moment is primarily a function of the current sent through the wire. There are limits to how much current can be sourced safely through a wire. To avoid melting the wires, the rule of thumb of $5mA/\mu m^2$ was used as an upper limit for designing the hinges [5]. For the cross sectional area of the hinges

$$\frac{i_{\max}}{w_h t_h} \leq \frac{5mA}{\mu m^2}. \tag{3.7}$$

A design rule for the thickness of the hinges can be determined by setting $M_{req} \leq M_{app}$ and using equation (3.7) for the largest feasible current. We see that for two hinges of equal dimensions

$$\begin{aligned} \frac{2 w_h t_h^2 \sigma_Y}{4} &\leq i_{\max} w_p L_p B \cos\theta & (3.8) \\ t_h &\leq 10 \frac{mA}{\mu m^2} w_p L_p B \sigma_Y \cos\theta & (3.9) \end{aligned}$$

Note that the width of the hinge cancels. At this point everything is known except for the thickness of the hinge.

The angle of bend, θ, can be ignored because the magnetic field is produced by a permanent horseshoe magnet [6] which can be freely rotated about the device. Thus, based on the maximum producible Lorentz force an upper bound on the thickness of the hinge is $1.21\mu m$. This means that a hinge thicker than $1.21\mu m$ cannot be folded by a Lorentz force due to the competition

B	0.1T
L_p	$500\mu m$
w_P	$500\mu m$
σ_Y	206MPa

Table 3.2: Known physical parameters

between maximum sustainable current and the moment required to plastically deform a hinge of given dimensions.

The optimal thickness is found by solving $\max\{M_{app} - M_{req}\}$, since M_{app} is linear in t_h, and $M_{req}$is quadratic as depicted in Figure 3-4.

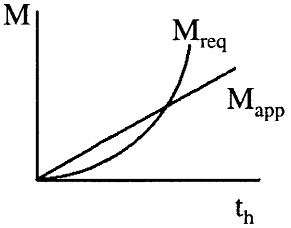

Figure 3-4: Required and applied moments as a function of hinge thickness.

$$\frac{\partial}{\partial t_h}\left\{\frac{5mA}{\mu m^2}w_h t_h w_p L_p B - \frac{2w_h t_h^2 \sigma_Y}{4}\right\} = 0 \quad (3.10)$$

$$th = \frac{5mA}{\mu m^2}\frac{w_p L_p B}{\sigma_Y}. \quad (3.11)$$

The result is an optimal thickness of $0.61\mu m$ of Au. With this thickness and the prescribed maximum current density, the membrane should fold to 60 degrees without having to rotate the magnet (in practice we were able to source more current and get ~90 degrees without rotating the magnet). The remaining 120 degrees is achieved by rotating the horseshoe magnetic about the device.

The width of the hinge is the last parameter to set now that the length and thickness have been constrained to meet the geometrical and mechanical requirements of folding. The width of the hinge in combination with the length is important for stabilization during folding, ensuring accurate alignment of the membrane with respect to the substrate. With the other dimensions fixed, the width is the primary factor in determining the lateral stiffness of the hinges so that acceptable tolerances for the final fold can be obtained. It should be noted that making the hinges extremely stiff is not the best method to ensure alignment because instead, it may prevent final, more precise positioning by another means. To avoid overconstraining the first prototypes, only two hinges were used instead of multiple hinges.

In theory the magnetic field should be arranged perpendicular to the end of the wire loop, however, in practice there may be some misalignment. Any misalignment will result in a torque about the hinges due to a uniform Lorentz force generated along each portion of the wire loop that runs the length of the membrane on either side.

A worst case analysis of the angle of twist goes as follows. First, the model is reduced to a single hinge as it is less stiff than the actual design with two hinges. The force produced along one side of the membrane due to a field misalignment of angle α is $F = iL_pB\sin\alpha$. The force of $F = iw_pB\sin\alpha$ is ignored because in the situation with two hinges, this force does not produce a twist. Concentrating the force acting along the sides of the membrane at the far end results in a torque of $F = iL_pB(\sin\alpha)w_p$. Thus, the worst case stiffness reduces to a calculation of the angle of bend of a beam in torsion. The angle of twist is given by $\phi = TL/JG$, where $J = (1/12)bh(b^2 + h^2)$, and $G \sim E/2$. Substituting these values we see that the angle of twist is predicted to be

$$\phi = \frac{ML_h}{\frac{1}{12}w_ht_h(w_h^2 + t_h^2)G} = \frac{iL_p(\sin\alpha)w_pL_h}{\frac{1}{12}w_ht_h(w_h^2 + t_h^2)G}. \tag{3.12}$$

A generous in-plane error of $\alpha = 20$ degrees was chosen for the magnetic field misalignment since one can surely align a magnet to within 20 degrees by hand (in practice, alignment marks deposited on the wafer were used to position the magnet). The allowable angle of twist was set to $\phi = 2 \times 10^{-4}$ radians because it was desired that one end of the membrane not tip by more than 100nm across its $500\mu m$ width. Substituting these and the other known dimensions, such as the optimal hinge thickness, t_h, results in the minimum hinge widths for the given lengths listed in Table 3.3.

Again, these minimum widths were calculated based on a worst case analysis. One extra constraint imposed by expense concerns is that the first generation of prototypes were to be

length(μm)	minimum width(μm)
30	10.7
50	17.9
100	35.8

Table 3.3: Minimum hinge widths for given hinge lengths.

thickness(μm)	length(μm)	width(μu)
0.6	30	25
0.6	30	50
0.6	50	25
0.6	50	50
0.6	100	25
0.6	100	50

Table 3.4: Final hinge dimensions used in prototypes.

fabricated using transparency masks. Instead of masks created by electron beam writing that can routinely produce features down to a single micron, the transparency films are printed on a high resolution printer that can only guarantee features greater than $20\mu m$. Thus the final widths were chosen to be 25 and $50\mu m$ for all three lengths. All of the devices would then have hinge widths stiff enough in the lateral direction, except for the combination of $100\mu m$ long and $25\mu m$ wide hinges which were included to study the effect of having a less stiff hinge in the lateral direction.

Thus, the final hinge parameters are of six flavors as summarized in Table 3.4. All of the hinges are of thickness $0.6\mu m$ because the deposition of the Au is uniform across an entire wafer.

3.2.2 Electrical Considerations

The device layer of the SOI wafer is slightly doped with a resistivity between 1 and 10 Ω-cm. This raises the concern of shorts if the wire loop is placed directly on the silicon, which could result in a nonfunctional device. However, the leakage current through the silicon is negligible. The Au wire loop and silicon are modeled as two resistors in parallel with resistances of 5×10^{-2} and 20×10^{3} Ω respectively [7]. The resistances differ by five orders of magnitude, and the Au wire can be deposited directly on the silicon without concern for short circuits. This was later confirmed experimentally by testing sample wires fabricated adjacent to each device. Two probe tips were placed on an Au wire. The power supply connected to both probes was set to source 0.4A. One probe was then slid off of the wire and onto the silicon. As soon as the probe slid onto the silicon the current stopped, indicating an open circuit. This was repeatable on other test wire structures as well as device wires.

3.2.3 Thermal Management

Additionally, the hinge and wire dimensions must satisfy heat conduction conditions such that the wires do not melt or soften with the applied current that generates power in the form of Joule heating. For this analysis a segment of wire was treated as having a perfect heat sink below and convection above. The silicon behaves as a perfect heat sink due to its high thermal conductivity of $1.412 Wm^{-1}K^{-1}$ [8], and because it is a larger thermal mass than the wire. Also, the folding actuation takes place in a fraction of a second (see section 3.2.4 below) so that prolonged heating of the silicon is of little concern. Due to the aspect ratio of the hinge width and thickness (50:1 or 100:1 depending on the design), convection from the $0.6\mu m$ tall sides is neglected. The current that produces the Lorentz force results in uniform heat generation throughout the wire of $q' = I^2R/\text{volume}$ or $q' = I^2\rho/(w_h t_h)^2$, where ρ is the bulk resistivity. The heat equation is given by

$$\frac{\partial^2 T}{\partial x^2} + \frac{q'}{k} = \frac{1}{\alpha}\frac{\partial T}{\partial t}, \tag{3.13}$$

where k is the hinge's thermal conductivity and α is the thermal diffusivity of Au. The steady state result is of most concern as it will yield the highest temperature encountered in the system. Thus the right side of equation (3.13) is zero, and the general solution to this differential equation is simply

$$T(x) = \frac{-q'}{2k}x^2 + c_1 x + c_2 \tag{3.14}$$

with the imposed boundary conditions for the heat sink (constant temperature) and convection surface conditions (modeled by the convection heat transfer coefficient, h)

h	$15 WK/m^2$ [61]
k	$315 Wm^{-1}K^{-1}$
ρ	2.44×10^{-8} Ω-m
T_{air}	$293K$
T_o	$293K$
T_{melt}	$1064 + 273K$

Table 3.5: Thermal coefficients and boundary conditions.

$$\begin{aligned} T(x=0) &= T_o && (3.15) \\ -k\frac{dT}{dx}|_{x=t_h} &= h\left[T_\infty - T(x=t_h,t)\right]. && (3.16) \end{aligned}$$

The resulting temperature distribution is a quadratic in x of the form

$$T(x) = \frac{-q'}{2k}x^2 + \left(\frac{q'}{k} - \frac{h}{k}\left[T_{air} - T(t_h)\right]\right)x + T_o. \tag{3.17}$$

The maximum temperature is of most concern. It is located where $dT/dx = 0$, which is

$$x_{\max} = t_h - \frac{h}{q'}\left[T_{air} - T(t_h)\right]. \tag{3.18}$$

Replacing q' with the heat generated, $I^2\rho/(w_h t_h)^2$, and substituting $x_{\max}$ into the temperature formula gives the maximum temperature in the wire as a function of applied current which is plotted in Figure 3-5 for the two different hinge cross sectional areas chosen. The material, convective properties, and boundary conditions listed in Table 3.5 were used.

We get the numerical values plotted in Figure 3-5 showing the relation between applied current and maximum temperature in the wire for two widths of 25 and $50\mu m$. These are worst-case estimates of the maximum current, and when compared to the rule of thumb of $5mA/\mu m^2$, we see that the two are in close agreement, differing by only a few milliamperes. The rule of thumb says that the maximum current for $0.6\mu m$ thick, $25\mu m$ wide and $50\mu m$ wide wires are 75mA and 150mA respectively, a discrepancy of only +4 and +8mA. As will be mentioned in section 4.2 up to 0.5 amps were successfully passed through the $25\mu m$ and $50\mu m$

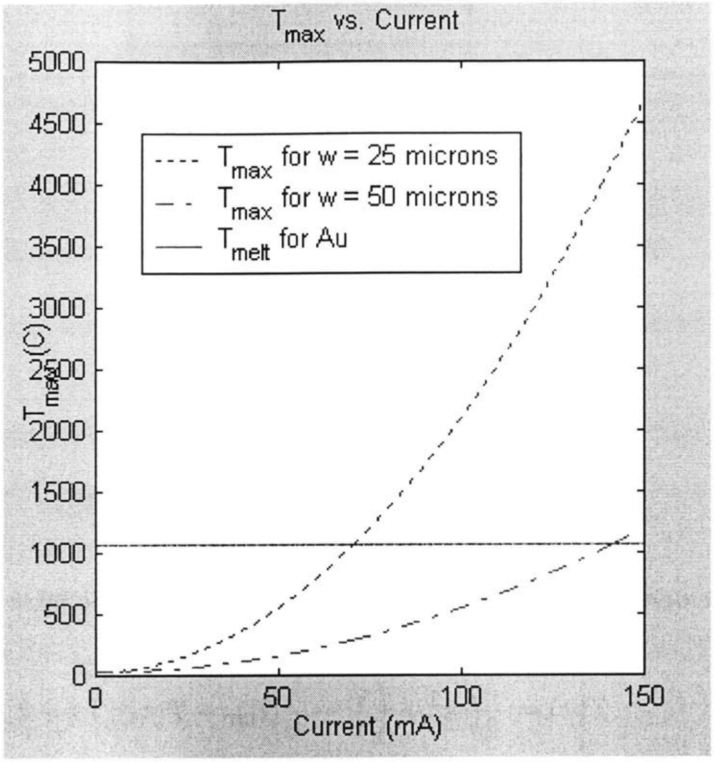

Figure 3-5: Theoretical model of maximum temperature in Au wire vs. applied current.

wide test wires on a silicon substrate for over one minute without any noticeable damage to the wires or substrate. This is roughly three to seven times greater than theory predicted and what was used in practice to initiate folding of the fabricated devices.

The strain induced by thermal expansion of the gold is insignificant for these first initial folding prototypes. With a coefficient of linear thermal expansion of $14.4 \times 10^{-6}/C$ [9] and a temperature increase of 1000C, the thermal strain results in a length increase of $1.4\mu m$ over a $100\mu m$ long hinge. In practice less than 20mA folds the device, which in theory only generates a maximum temperature of 350C and a corresponding length increase of half a micron. In the future, when alignment tolerances must be met for final positioning, this may be an important factor to consider.

3.2.4 Dynamics of Folding

There are three regimes of the folding process: elastic, plastic, and elastic oscillation. The time constant of the folding process is calculated by integrating the equations of motion for all three regimes numerically. Up to a critical angle when the yield stress is reached, the folding is purely elastic in nature. Beyond the yield point, plastic deformation of the Au hinge begins and continues until the maximum angle is reached for a given forcing function. From the maximum angle, the hinge springs back elastically and oscillates before settling to an equilibrium position. If the forcing function were removed at this point, the hinge would return not to the original starting point, but to a new "rest angle" determined by the extent of permanent strain due to plastic deformation. Due to the nature of the second order system, the hinge would oscillate about this rest angle until finally settling.

During the initial elastic folding, the equation of motion is a standard second order system with spring constant k, damping coefficient c for drag, and forcing functions due to the applied moment from the Lorentz force and gravity,

$$J\ddot{\theta} + c\left(\dot{\theta}\right)^2 + k\theta = M_a \cos\theta - M_g \cos\theta. \tag{3.19}$$

J is the moment of inertia for the flap based on the parallel axis theorem since the membrane is rotating about a virtual pivot point at the midpoint of the hinges,

$$J = m_p \left(\frac{L_p^2}{12} + \left(\frac{L_h + L_p}{2}\right)^2\right). \tag{3.20}$$

L_p is the length of the plate or membrane and m_p is the plate's mass. The spring constant k is calculated from the torque required to bend the hinge in the elastic regime

$$\frac{M}{EI} = \frac{1}{\rho} \tag{3.21}$$

where E is the Young's Modulus, I is the second moment of area or moment of inertia of the hinge and ρ is the radius of curvature of the bend. Knowing that $\theta\rho = L_h$ for a constant radius of curvature, equation (3.21) can be rewritten as

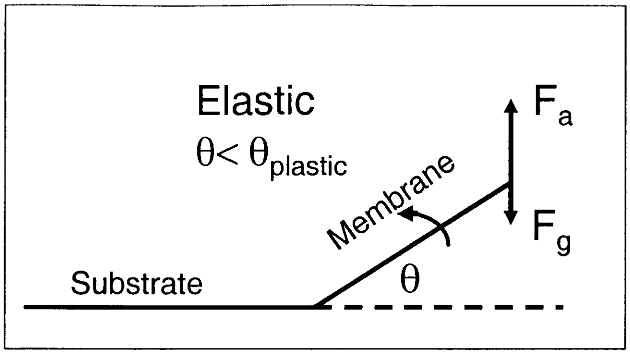

Figure 3-6: Elastic regime: $J\ddot{\theta} + c\left(\dot{\theta}\right)^2 + k\theta = M_a \cos\theta - M_g \cos\theta$

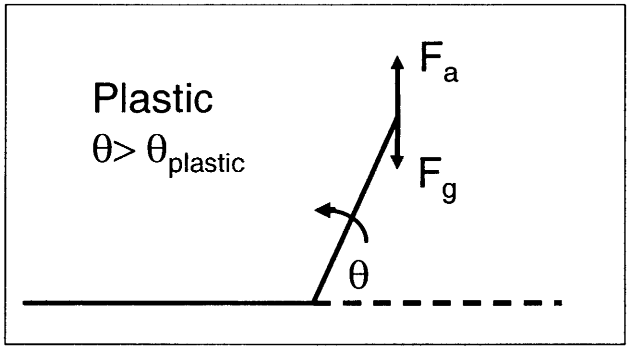

Figure 3-7: Plastic regime: $J\ddot{\theta} + c\left(\dot{\theta}\right)^2 + M_{req} = M_a \cos\theta - M_g \cos\theta$

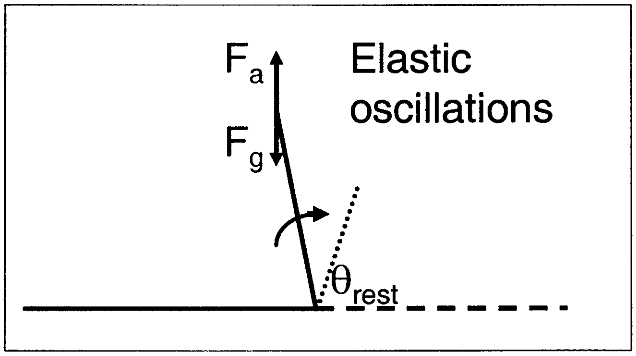

Figure 3-8: Elastic oscillation: $J\ddot{\theta} + c\left(\dot{\theta}\right)^2 + k(\theta - \theta_{rest}) = M_a \cos\theta - M_g \cos\theta$

$$M = \frac{EI\theta}{L_h} \qquad (3.22)$$

whereby the torsional spring constant is recognized as being $k = EI/L_h$.

Drag is the primary damping mechanism as the membrane moves through and displaces ambient air while folding. Another source of energy dissipation stems from thermoelastic damping. It is well known that thermal effects induce stress and strain, as in the classic example of a temperature sensor based on a bimetallic strip. The relation between temperature and strain can be derived from the Hemholtz Free Energy since it is a function of both strain and temperature [11][12]. From this relation it can also be seen that strain induces temperature gradients. Due to these temperature gradients, heat flows, which is irreversible. Thus, there exists a coupling between the mechanical energy in bending and energy dissipation through heat loss. This thermoelastic effect is negligible when a MEMS device operates in ambient atmosphere [11], and it is only significant for the design of high Quality factor MEMS resonators which typically operate in vacuum [11][12][13][14]. For our device, drag is assumed to be the only significant source of damping.

The membrane presents a bluff body moving through air. Tabulated drag coefficients for a plate subjected to fluid motion perpendicular to the face are available in many texts on fluid mechanics. It is assumed that fluid flow remains perpendicular to our plate while it undergoes rotation about the hinges. Therefore, the drag associated with a square plate moving through a fluid is modeled as

$$D = (1/2)C_d\rho_{fluid}U^2A \qquad (3.23)$$

where D is the drag force, C_d is the dimensionless drag coefficient of value 1.18 (based on the square aspect ratio of the membrane) [15], ρ_{fluid} is the density of the fluid (air), U is the object's velocity, and A is the frontal area perpendicular to the flow. Since our plate undergoes rotation about the hinges, the average velocity becomes $U_{avg} = (1/2)(L_h + L_p)\theta'$.

The effect of drag in the form of an opposing torque is

$$M_d = (1/2)C_d\rho_{air}L_pw_p\left(\frac{L_h + Lp}{2}\right)^3\dot{\theta}\left|\dot{\theta}\right| \qquad (3.24)$$

where the $\left|\dot{\theta}\right|$ is used to maintain the correct sign or direction of the torque.

The applied moment from the Lorentz force and gravity suffer an attenuation of $\cos\theta$ as the membrane is folded. Assuming that the magnetic field remains perpendicular to the end of the wire loop, the applied moment is as listed in equation (3.6) and that of gravity is $M_g = (1/2)m_p g(L_h + L_p)\cos\theta$.

Up until the point of plastic deformation, the motion of the flap is a second order system modeled as

$$J\ddot{\theta} + M_d + k\theta = M_a \cos\theta - M_g \cos\theta \tag{3.25}$$

which oscillates and decays to a constant deflected equilibrium angle if the current is not large enough to reach the plastic regime.

However, the goal of membrane folding is to achieve a larger degree of plastic deformation. Plastic deformation begins once the applied moment, equation (3.6), is equal to the yield moment, $M_Y = (2/3)w(t/2)^2\sigma_Y$. It can be shown that the radius of curvature at the onset of yield is given by $\rho_Y = Et/2\sigma_Y$ [2]. For an Au hinge of thickness $0.6\mu m$, this places the radius of curvature at yield to be $116\mu m$. Approximating the hinge as being a perfect curve, the radius of curvature, hinge length, and angle are related as $\theta\rho = L_h$. Thus, for a $100\mu m$ long hinge, the membrane will be rotated to an angle of 49.4 degrees before yield begins.

Modeling the dynamics of plastic deformation follows the form of the second order model above, except that the torque from the spring constant is now replaced by the required torque to create plastic deformation in the hinge, equation (3.5). This equation applies only once for the time between the onset of plastic deformation on the upswing and the maximum angle reached (see Figure 3-7).

Upon the backswing the hinge once again falls into an elastic regime and is modeled in a similar way as equation (3.19) except that plastically deforming the hinge results in permanent and irreversible strain, and thus a new equilibrium position termed the "rest angle." Therefore the equation of motion during elastic oscillation is given as

$$J\ddot{\theta} + c\dot{\theta}\left|\dot{\theta}\right| + k(\theta - \theta_{rest}) = M_a \cos\theta - M_g \cos\theta \tag{3.26}$$

where the spring constant is now a function of the difference between the angle of the membrane and the rest angle. This equation is valid until the hinge settles to its equilibrium position. If the current is maintained then the new equilibrium position will be greater than the rest angle due to the external force. However, once the current is turned off, this equilibrium position will be the rest angle determined by the degree of plastic deformation, assuming that gravity is negligible. The rest angle for $0.5 \mu m$ thick Au hinges has already been studied by Zou, et. al. [18][19]. Shorter hinges result in larger rest angles because more plastic deformation occurs for the same degree of bend. Interpolating and extrapolating from their data the rest angles for 30, 50, and $100 \mu m$ long hinges are 62, 30, and 0 degrees, respectively. The zero rest angle for $100 \mu m$ was observed in our experiments.

The equations and the regimes in which they are valid are depicted in Figures 3-6, 3-7, and 3-8. The equations were integrated numerically in Matlab using the ode45 function, and the results are plotted in Figures 3-9, 3-10, 3-11, and 3-12.

There are some slight differences between the experimental and simulation results. First of all, the simulation approximates the current as a step function while in practice the current was filtered through an RC circuit with a time constant of 0.6 seconds. There are still some discrepancies in the results that are independent of the shape of the forcing function. In the lab it required only 17.7mA to actuate the membrane to 87 degrees. However, in the simulation, 17.7mA is not sufficient to induce plastic deformation, which begins at 49.4 degrees. The simulation predicts that 26.5mA or greater is needed to plastically deform the hinge (see Figure 3-9), and this yield is reached within 0.002 seconds. Furthermore, for the simulation to reach a maximum angle of deflection near 90 degrees it requires roughly 115mA. Upwards of 500mA sends the membrane to almost 150 degrees before settling to an equilibrium of nearly 85 degrees within 5 seconds (see Figure 3-12). Even though the final angle agrees with experimental observations, the current and settling time are far too great. As will be mentioned in section 4.4, this may be attributable to an error in the magnetic field strength.

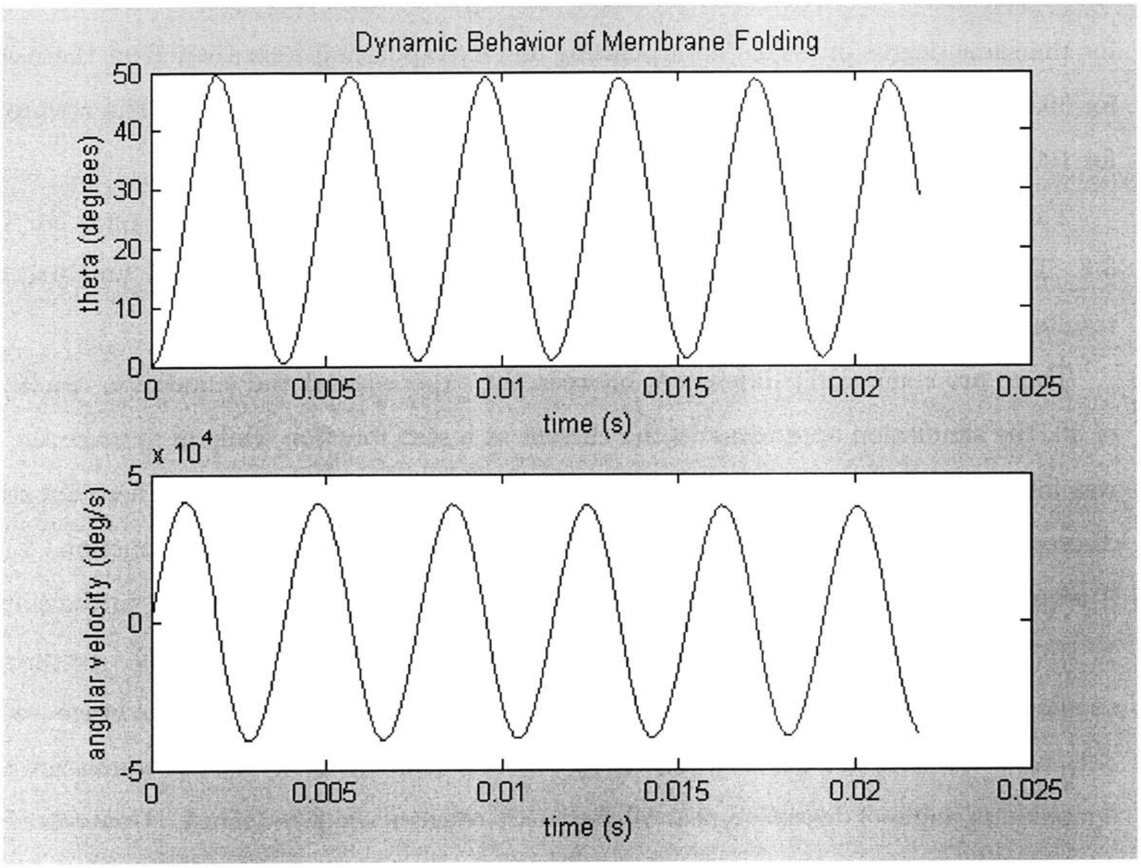

Figure 3-9: Start of plastic deformation with 26.5mA applied as step function.

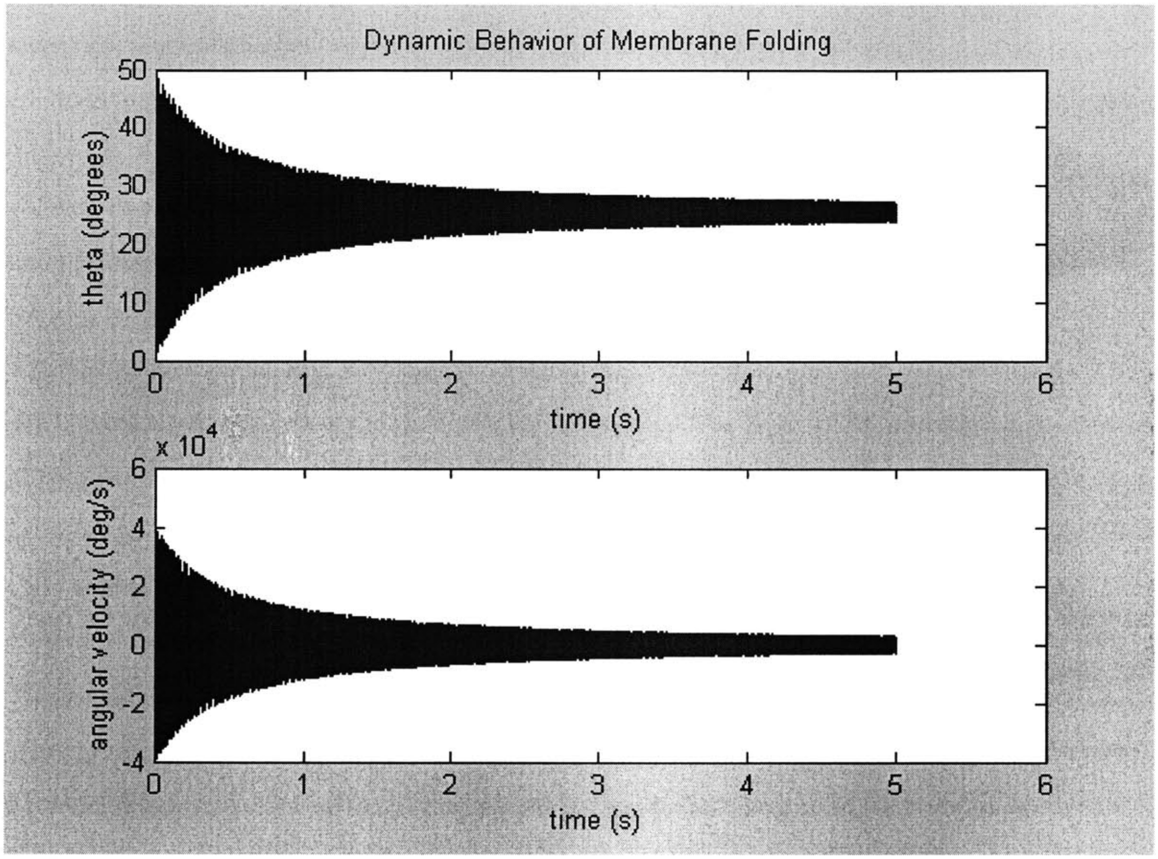

Figure 3-10: Membrane response to 26.5mA step signal.

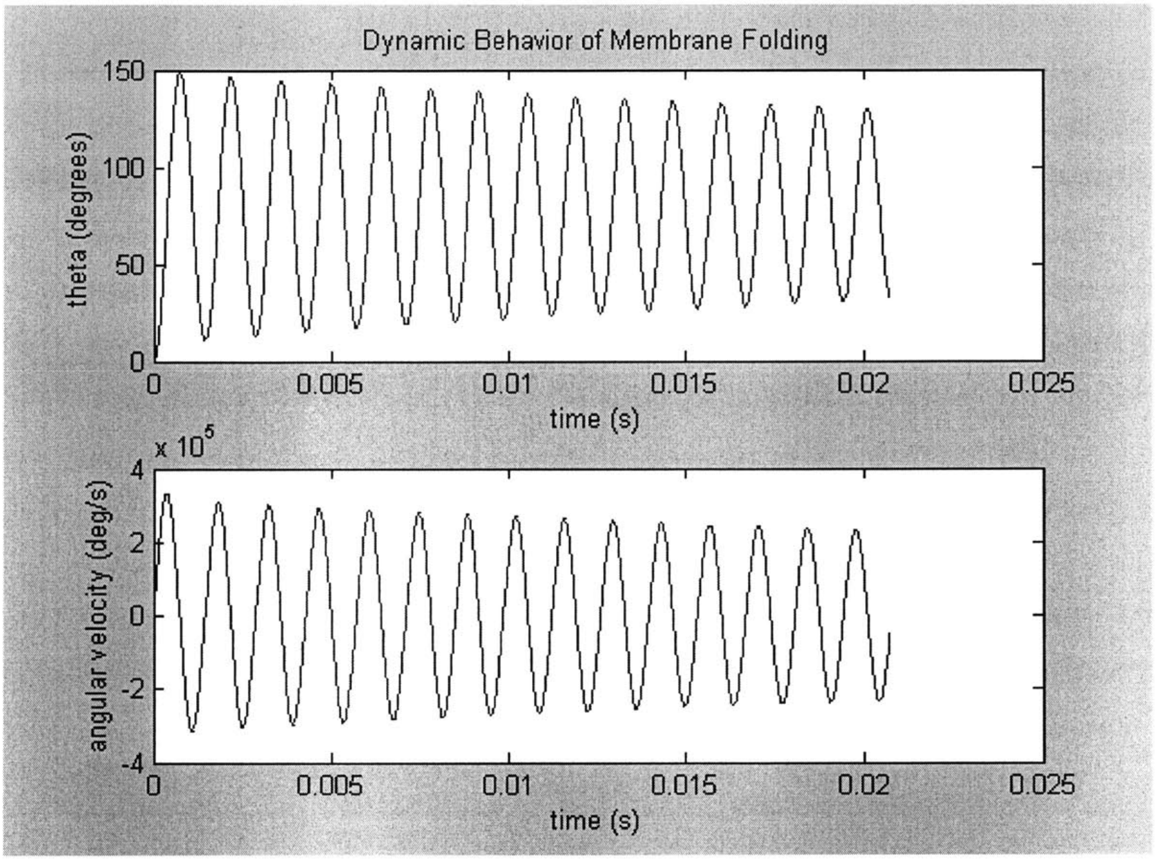

Figure 3-11: When 500mA is applied the flap overshoots 90 degrees.

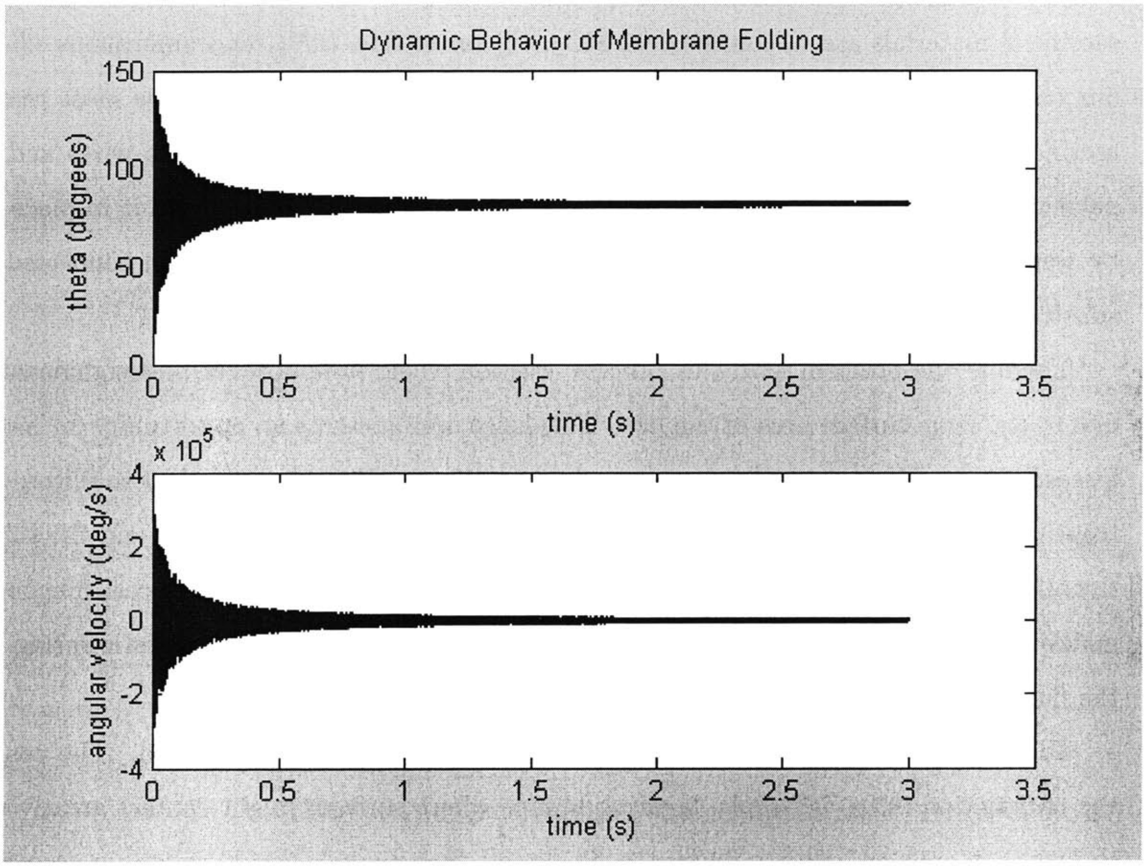

Figure 3-12: The flap settles to around 85 degrees within a few seconds when 500mA is applied.

3.3 Process Flow

3.3.1 Release from the Substrate

The most critical moment for any MEMS device is the release process. Sometimes months can be spent fabricating a device only to find out that the release process does not work as expected or that stiction fuses the released device to the substrate, rendering it useless. Typically, the release of a device takes place when a sacrificial material is selectively etched away. Common sacrificial materials are silicon dioxide, SiO_2, silicon nitride, SiN_x, and amorphous silicon. In our case, since we chose to use an SOI wafer, the buried oxide seemed the most reasonable sacrificial material. Once the membrane is defined in the silicon and the wires and hinges patterned, only the hinges and the oxide beneath the island of silicon hold it in place. Thus, by wet etching the buried oxide in hydrofluoric acid (HF) the flap is then connected to the substrate only by the hinges, and then folding can be initiated.

There is one problem with this process; stiction would undoubtedly be a significant factor due to the large surface area of the flap. This large area presents an opportunity for interfacial forces (van der Waals, hydrogen bonding, electrostatic, capillary) to weld the two silicon surfaces together irreversibly. As the wet etchant evaporates from between the flap and the substrate, the released flap is sucked down closer to the substrate by surface tension forces. If enough area makes contact and enough bonds form, the adhesion forces dominate the elastic spring back of the flap, and stiction prevails.

To prevent stiction from occurring, antistiction bumps were to be used. The concept of the antistiction bump is simple; creating bumps where surfaces might contact greatly reduces the contact area and thus reduces the likelihood that enough bonds will form to overpower the elastic springback. Several antistiction bump methods exist, but we felt that the maskless technique of [10] was the simplest. As depicted in Figure 3-13, a short HF etch exposes the underside of the silicon device layer of an SOI wafer. A conformal layer of nitride is deposited so that the underside edges are coated. The next step is a nitride reactive ion etch (RIE) which selectively etches the nitride, but only that which is exposed to a direct line of sight. Thus the nitride deposited underneath the silicon remains, forming a bump.

Stiction forces dominate elastic forces once a critical length between bumps is exceeded.

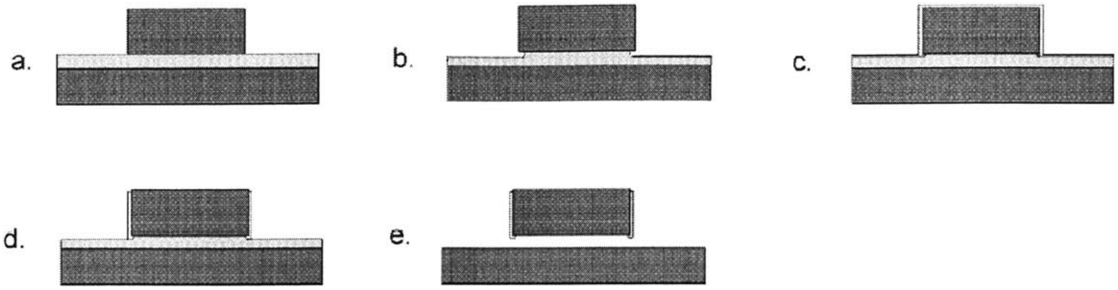

Figure 3-13: Fabrication process for creating maskless antistiction bumps presented in 3-14.

The beam is simply supported on either side by antistiction bumps. Adapted from the models and calculations in [10] the mechanical energy required to deflect the beam a distance equal to the gap, g, is found to be

$$E_m = \frac{Et^3g^2w}{2x^3}. \tag{3.27}$$

The surface energy is given by

$$E_s = C - \gamma_s(l - 2x)w \tag{3.28}$$

where C is a constant and γ_s is the adhesion energy per unit area.

Taking derivatives to find where the decrease in elastic mechanical energy matches the increase in surface energy (by increasing the detachment length x) yields the critical length scale as

$$\begin{aligned} \frac{\partial E_m}{\partial x} + \frac{\partial E_s}{\partial x} &= 0 && (3.29) \\ x_{crit} &= \left(\frac{3}{16}\frac{Et^3g^2}{\gamma_s}\right)^{1/4}. && (3.30) \end{aligned}$$

Therefore, if a membrane flap with our dimensions and surface adhesion $\gamma = 100J/m^2$ [10] was simply supported by antistiction bumps running the length of two parallel sides (Figure 3-14) then the minimum distance between antistiction bumps would need to be $278\mu m$. Therefore, as the flap is $500\mu m$ wide, it would be necessary to have at least one more bump running along the center to prevent stiction from occurring. However, in reality, the structure of interest is 2D with antistiction bumps running along the entire square perimeter. Therefore, applying the critical length in both directions builds in an extra factor of safety.

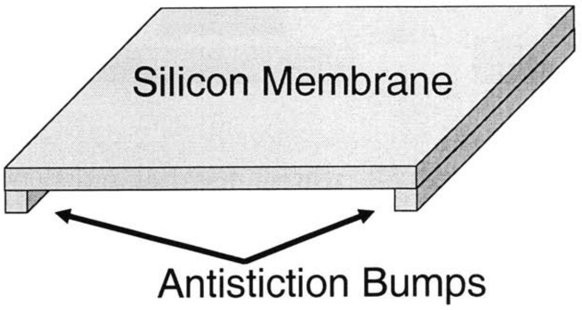

Figure 3-14: Antistiction bumps running the length of a membrane on two sides.

Adding extra bumps in the center of the membrane was actually very easy to do because the prototype design also called for extra holes in the silicon so that HF could penetrate into more of the SiO_2. As 5:1 buffered HF etches SiO_2 at $0.1\mu m$/min, it was desirable to add perforations in the membrane to allow for a quicker release etch. Without the added holes, it would take approximately 42 hours for the SiO_2 to be completely removed underneath the membrane. During this extremely long time the HF would also etch the silicon slightly. It was decided to locate holes such that the largest gap was $50\mu m$, resulting in a release time of approximately 4 hours. The proximity of etch holes is much smaller than the critical length for antistiction bumps, therefore stiction would not be an issue during release (antistiction bumps would form a ring around each one of the etch holes).

Due to Au contamination issues we could not use LPCVD nitride as in [10]. In our design we chose to use PECVD amorphous silicon to form the bumps (PECVD nitride seemed an obvious substitution except that it is readily etched in HF unlike its LPCVD counterpart). Yet before we could test the antistiction bumps on the first membrane prototype, a colleague tried them on a tunable cylindrical zone plate and they did not work. A safer option then seemed to be to remove material from the backside of the wafer underneath the membrane.

The benefit of a backside etch is that it guarantees stiction will not occur, simply because there is no substrate left behind the released device. The downside is that backside etching increases the number of fabrication steps and tends to be more difficult to control. The most common method requires plunging through the backside of the wafer using an aqueous potassium hydroxide (KOH) solution. Deep KOH etches tend to be more of an art than a science. The reaction is highly dependent upon temperature, bubble formation at the Si interface, and masking material. Etch rate nonuniformities add up across $500\mu m$, and thus repeatability is not very high.

Protecting the devices on the front of the wafer is the most fundamental challenge in KOH etching. In the first KOH attempt, a Teflon chuck complete with an O-ring seal was used to protect the frontside. However, as the etch neared completion, the membranes popped. Doing a quick back of the envelope calculation revealed that the pressure increase due to the temperature change (the etch ran at 80C) was very close to the pressure limit that the thin layer of oxide could support.

Several alternatives were investigated. The two most promising techniques involved bonding a dummy wafer to the front of the device wafer with electronics grade epoxy and using poly(dimethyl siloxane) (PDMS) to coat the front of the wafer. The epoxy technique works very well when the device wafer is heated on a hot plate and a bead of epoxy is spread around the perimeter. A dummy wafer is then matched to the device wafer and the assembly is allowed to cool. After the KOH etch is complete, the epoxy is easily and completely removed by a piranha clean (sulfuric acid and hydrogen peroxide cocktail mixed 3:1), the recommended post-KOH clean. This approach worked reliably well, though on a few occasions leaks occurred. Due to the opacity of the two wafers, leaks are not detected until after the wafers are separated in piranha. For our devices, this would be too late, for only ten minutes of KOH exposure completely destroys the membranes. Additionally, the piranha clean would be too harsh for the membranes because large bubbles form that would latch onto the membranes and pull them off.

In the end, we chose the PDMS technique. It is ideal because PDMS forms a transparent etch mask so leaks are readily observed. However, PDMS is not a standard cleanroom material and thus it is deemed a back-end process not allowed in the Microsystems Technology Laboratory (MTL). PDMS (Dow Corning's Sylgard 184 Silicone Elastomer) was either

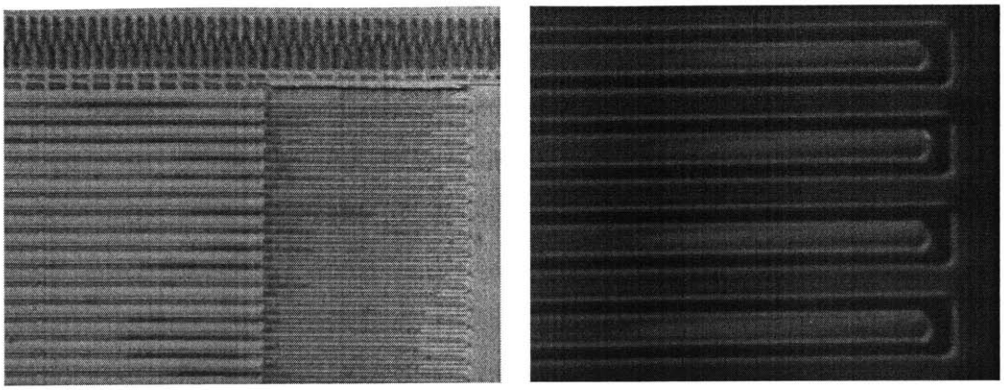

Figure 3-15: Gratings with $2\mu m$ feaures [3] intact after PDMS removal by CCR dissolver. Close up of flexures (right).

spun on (down to as thin as $50\mu m$ for KOH masks) or simply poured on (as thick as several millimeters) and then cured at 70C for 1.5 hours. Upon completion of the etch, the PDMS can be removed with a number of chemicals. The method of choice is tetrabutylammonium fluoride in n-methyl-2-pyrrolidinone mixed 3:1, yet due to its toxicity it was not allowed in the laboratory we were using. Hexane and trichloroethylene remove PDMS because they cause PDMS to swell which effectively shears the PDMS off of the substrate. This works for devices with relatively large features, yet for devices such as tunable diffraction gratings, the shear rips the $2\mu m$ wide slats and comb drive fingers off of the buried oxide (see Figure 3-16). The best solution found is a product by Amtex Chemicals called CCR Silicone Dissolver [56]. The CCR dissolves the PDMS into a gel which is then rinsed free of the substrate with deionized water. It should be noted that moisture dramatically affects the result of the dissolving process. If any water is present with the CCR, the silicon substrate becomes irreversibly tarnished. If no moisture is prevented, CCR does not adversely affect the Si, Au, Cr, or SiO_2, even after 48 hours. Unlike hexane and trichloroethylene, CCR gently removes PDMS without destroying fragile device structures (Figure 3-15).

3.3.2 Microfabrication

The process flow used to create the first prototype is discussed below and illustrated in Figure 3-17. The complete process flow is listed in the appendix. The substrate is a 100mm (4 inch)

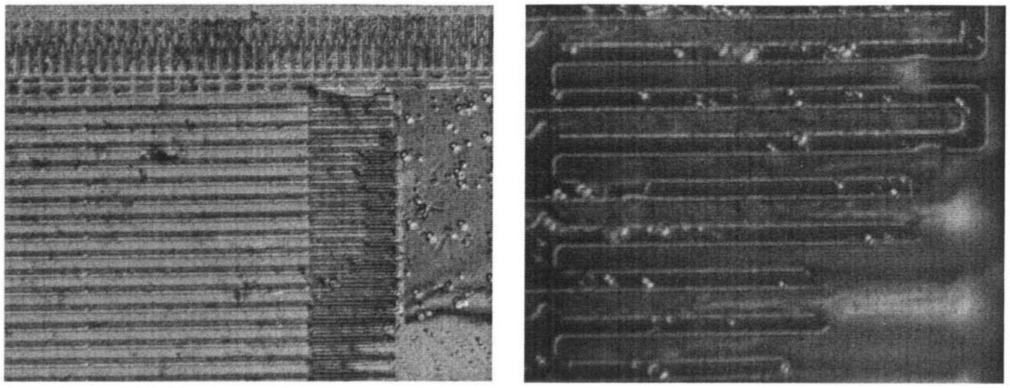

Figure 3-16: Broken flexures and combdrives [3] as a result of PDMS removal with trichloroethylene. Close up of broken flexures (right).

diameter silicon on insulator (SOI) wafer with a $10\mu m$ device layer, $1\mu m$ thick buried oxide, and $500\mu m$ handle wafer thickness.

The first step involves etching through the silicon device layer in order to define the membrane flaps. KOH was chosen instead of deep reactive ion etching (DRIE) because sloped sidewalls are better suited for the hinge material deposition rather than vertical sidewalls. Electron beam evaporation deposits gold on the wafer by line of sight. Therefore, if the sidewalls are vertical then a discontinuity forms. To avoid mechanical and electrical gaps in the hinges, a planarization step would be necessary before depositing the Au. However, the extra steps of depositing oxide and using the CMP to polish back the top surface were avoided by using the KOH sloped sidewall. Measurements taken with an AFM verified that the Au thickness was adequate along the sloped sidewalls.

PECVD SiN_x is deposited and patterned on both sides of the wafer for use as a KOH hard mask. Typically, LPCVD nitride is used for KOH masks due to its extreme resilience to KOH. Because the device layer is only $10\mu m$ thick, requiring a short etch of eight minutes (25% by weight KOH solution at 80C), 500Å of PECVD nitride is sufficient, does not lead to pinholes, and is grown in a matter of minutes as compared to hours for LPCVD. After the KOH etch exposes the buried oxide, the top layer of nitride is removed by reactive ion etching (RIE).

The metal hinges and wires are patterned in a lift-off process where resist is deposited and patterned before the metal deposition. Resist is removed where metal is to be deposited on the substrate. It is customary to use image reversal photoresist for lift-off because the sidewalls are inverted, much like a cliff. In this way a discontinuity in the metal layer exists and upon soaking in acetone the unwanted metal falls off as the photoresist dissolves. In our process it was necessary to use $8\mu m$ of thick resist (AZ 4620) instead image reversal. The image reversal photoresist was simply too thin to coat the $10\mu m$ deep trenches. The photoresist patterning was followed by electron beam evaporation of 300Å of Cr followed by $0.6\mu m$ of Au. As mentioned earlier, Au deposited directly onto Si exhibits adhesion problems, and for this reason a thin layer of Cr was deposited first.

The next major step is the KOH backside etch. The back of the wafer is coated with another layer of PECVD nitride, this time 2,000Å thick. PDMS is spun on the front of the wafer and cured. The KOH etch requires 6.25 hours to etch through the $500\mu m$ thick handle. However, the etch is typically stopped before reaching the oxide. Due to the nonuniformity of KOH etching and its low selectivity between Si and oxide, it possible to etch through the oxide and ruin devices. Near the end of the etch, the KOH is replaced by tetramethyl ammonium hydroxide (TMAH). Though TMAH has a much lower etch rate than KOH, it has a much higher selectivity. In this way, all of the Si can be safely removed without damaging the devices.

The PDMS is removed with CCR as mentioned above. At this point the membrane is held fixed solely by the buried oxide, which can be removed with HF or an RIE. We tried HF, yet the surface tension was too great, and it detached the membranes from the substrate. A dry release is almost always preferred and it turned out to be the best method. The wafer was flipped over and an oxide RIE chemistry removes the buried oxide and releases the device.

Upon release all the devices were bent in the direction toward the handle wafer. This means that they bent upwards against the force of gravity while they were being released. This is explained by the high tensile residual stress of the Cr film underneath the somewhat stress-free Au. This observation of stress induced bending is one reason why we began investigating residual stress folding as described in Chapter 5.

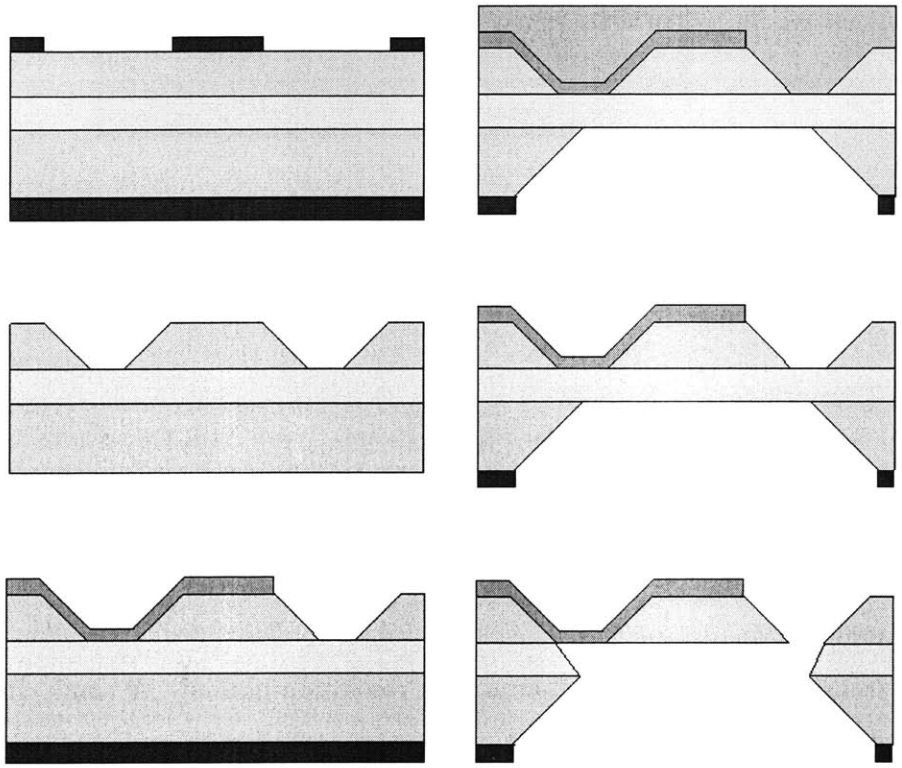

Figure 3-17: Backside etch process flow for first prototype.

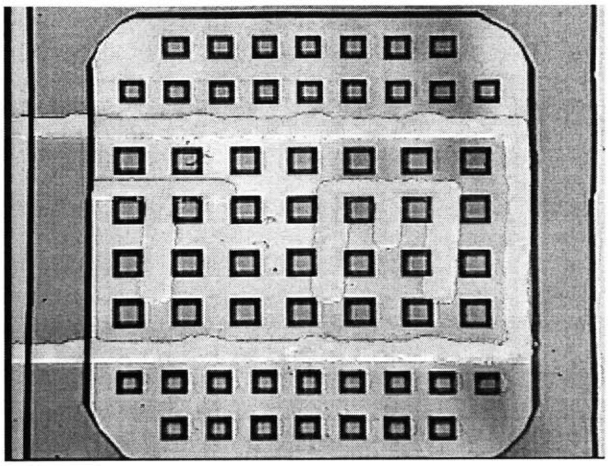

Figure 3-18: $25\mu m$ Au features patterned by transparency generated masks.

3.4 Layout

3.4.1 Transparency Masks

For the first set of prototypes we decided to use transparency masks instead of chrome masks that are written with an electron beam. The transparencies are inexpensive yet they do not permit features below $20\mu m$. For a proof of concept, $20\mu m$ was sufficient. The CAD mask layouts are listed in Appendix A.

The transparencies are printed on a high resolution printer. A blank chrome plate which is covered with photoresist is masked by the transparency and exposed in the Electron Vision's UV system (EV1). Thus the patterns are transferred to the chrome plate which is developed and then acid etched to selectively remove the chrome. This chrome mask is then used to expose the wafers.

In Figures 3-18 and 3-19 images are shown that depict in detail how the quality of the transparency varies. The $25\mu m$ wires in Figure 3-18 exhibit many ripples. The $50\mu m$ features on the other hand are much more consistent and smooth. The "T" and "M" are patterned in Au on these flaps so that upon completion of the fold they line up with a matching "I" in order to spell out "MIT" which could be visualized using an infrared camera.

No significant effects resulted from the wavy patterns generated by transparency masks.

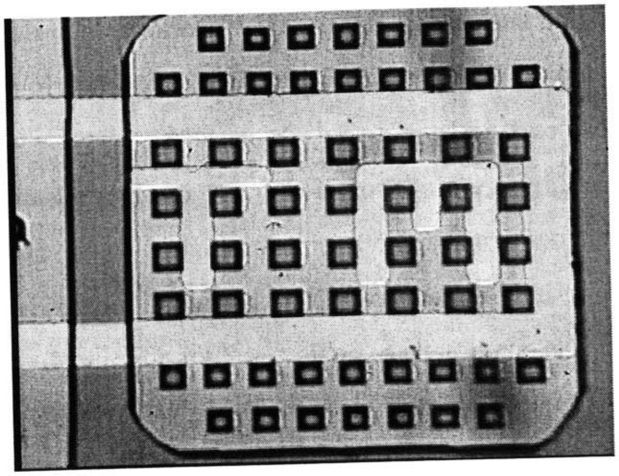

Figure 3-19: $50\mu m$ Au features patterned by transparency generated masks. Note the improved quality.

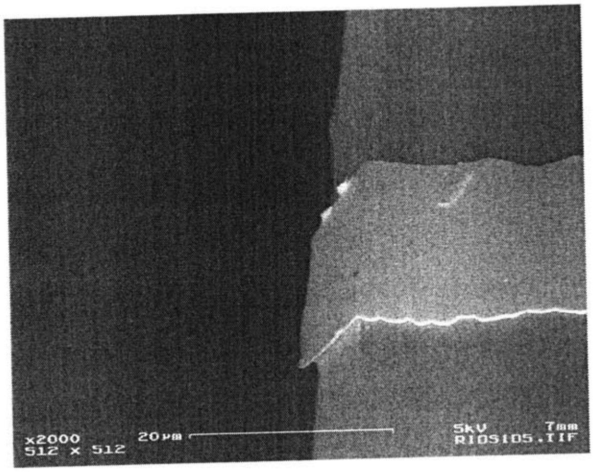

Figure 3-20: SEM of a broken hinge, showing a wavy $25\mu m$ wide wire.

3.4.2 Alignment Fiducials

The same mask used to create the Au wires and hinges also laid down alignment reference features to assess folding accuracy. Two Au "L" brackets and one bar frame the edge of where the membrane flap should land once folded to 180 degrees. It makes sense to use the same mask as the wires for creating the fiducials because this way they are most accurately aligned to the direction of the hinges. However, if the wire mask is misaligned to the first mask which defines the KOH trenches around the membranes, then some error can be introduced so that the folds end up not entirely symmetric. Yet this misalignment is very small because with the EV1 system in MTL it is customary to achieve $\pm 2\mu m$ alignment. With two alignment features on either side of the wafer separated by 5cm, this gives a worst-case rotational misalignment error of $\phi = \tan^{-1}(2 \times 2\mu m/5cm) = 0.005$ degrees, which is quite tolerable.

Extra Au wires stretching several millimeters were also created at this time for use in aligning the magnetic field. During the actuation step, the face of the magnet is aligned along these wires to ensure that the field is perpendicular to the end of the wire loop.

Chapter 4

Prototype Testing

4.1 Experimental Setup

Testing of the released devices took place on the Optical Engineering Group's probe station and videos of the folding devices were taken using the Schmidt Group's probe station and camera [21]. The wafer was positioned on the wafer chuck and the horseshoe magnet was laid directly on the wafer to ensure perpendicularity in one dimension. In order to align the magnetic field in the other direction, the faces of the magnet were positioned (by hand, using the probe station's microscope) flush against long, straight gold markings created on the wafer at the same time as the gold wires and hinges.

Folding to 180 degrees is a two step process because in the setup described above, the Lorentz force will always be directed vertically. Thus it is not possible to fold beyond 90 degrees in this configuration. The flap initially is nearly horizontal, yet it will not return to the initial position after folding to ninety degrees, but rather a new equilibrium position determined by the amount of permanent strain induced. Once permanent strain positions the membrane above the horizontal, the orientation of the magnet is rotated 90 degrees so that the magnetic field is vertical. Using this final configuration, the membrane is folded to 180 degrees.

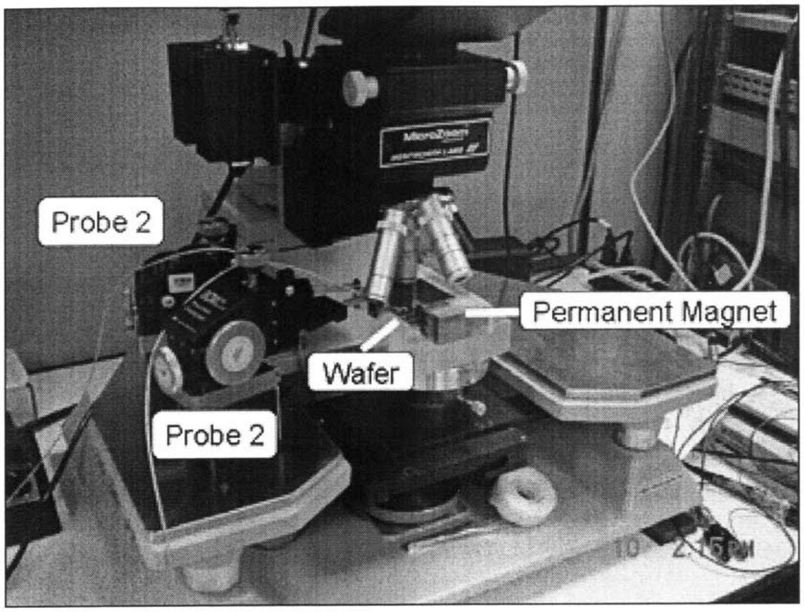

Figure 4-1: Probe station complete with wafer, magnet, and probes.

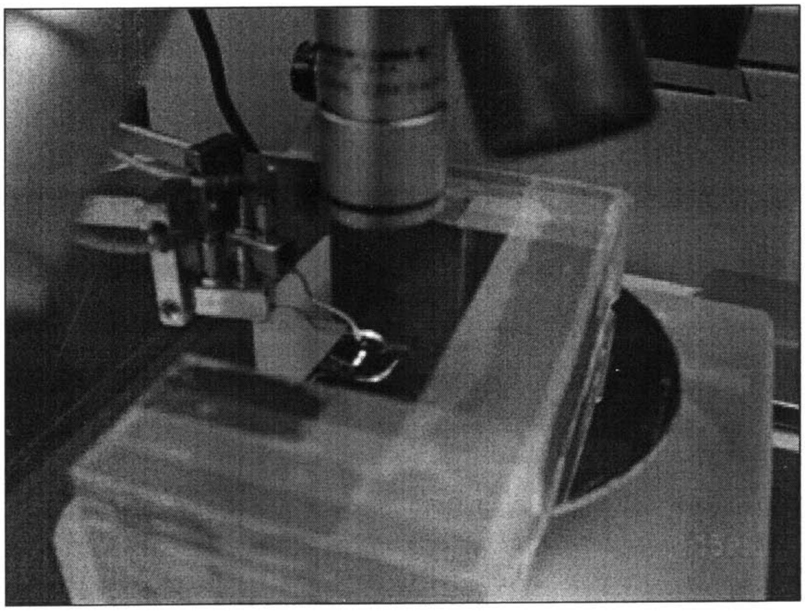

Figure 4-2: Close up showing wafer underneath magnet and probes.

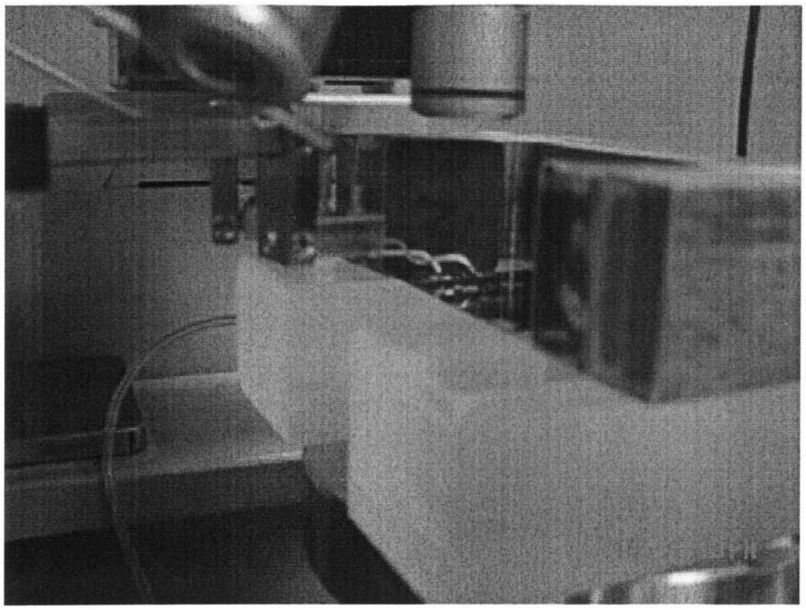

Figure 4-3: Another vantage point showing placement of magnet, wafer, and probes.

4.2 The First Fold

Test wires were fabricated along with each device so that the electrical properties could be measured before attempting to send current through the actual devices. As mentioned in section 3.5, the $25\mu m$ wide wires were designed to carry up to 75mA and 150mA for the $50\mu m$ wide wires before melting. In the lab it was possible to flow up to 500mA in each of the wire designs for up to one minute with no visible sign of damage or change in resistivity. Higher currents were not tested simply because the power supply could not source anything beyond one half ampere.

With more than enough current available, it was time to fold the first device. Testing was to begin with 1mA of current followed by increments of 5mA. Unfortunately, due to an unknown problem with the power supply, the first fold was unsuccessful because a spike in the applied current sent 200 times as much current and blew the flap off, severing the hinges completely (see Figures 4-5 and 4-6). In Figure 4-6 a slight undercut of the Au is visible. This undercut is due to the Cr adhesion layer between the Si and Au getting partially etched during piranha cleans. The power supply's transient is shown (using 1kΩ instead of the 24.5Ω of the device)

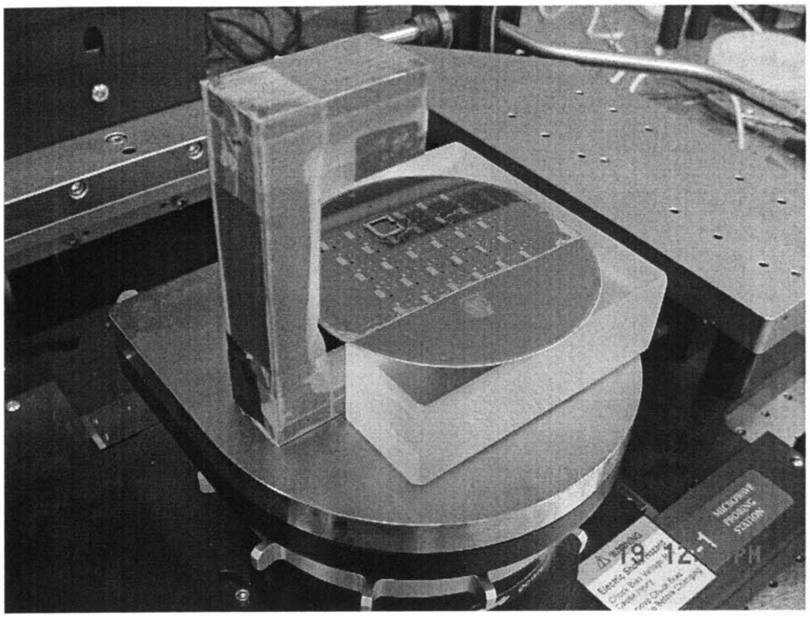

Figure 4-4: The second part of the 180 degree folding process involves rotating the magnet to a vertical orientation.

in Figure 4-7.

Carefully examining the video taken of this actuation, there are two frames that show a small part of the right hinge because it flashes as it moves through the horizontal position. At a frame rate of 30Hz, these two frames must sit on either side of the voltage spike. Looking closely at the voltage plot, there exists a small dip in the voltage right before the spike. This dip in the voltage would result in a change of sign of the Lorentz force and the flap would initially be forced downward.

These two problems with the power supply were solved by adding an RC circuit between the supply and the device. Not only does the RC circuit low pass filter the signal, but it also adds some delay to the actuation so that it is easy to capture on video. A 100 Ω resistor and 6,660μF capacitor create an RC time constant of 0.6 seconds. The total charging time, estimated as 5RC's, is 3 seconds for this circuit. The RC circuit was successful as evidenced by several completed folds.

Another lesson learned is that the membrane acts as a mirror and therefore it is impossible to image the membrane with an optical microscope when the illumination is directly above and

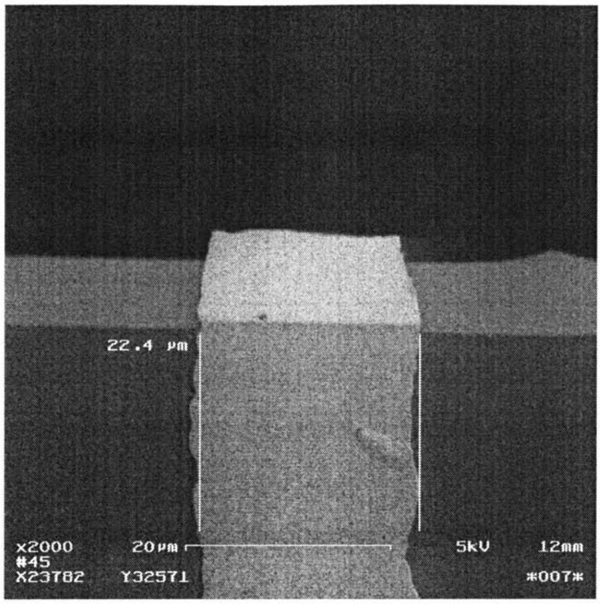

Figure 4-5: Top view of severed hinge.

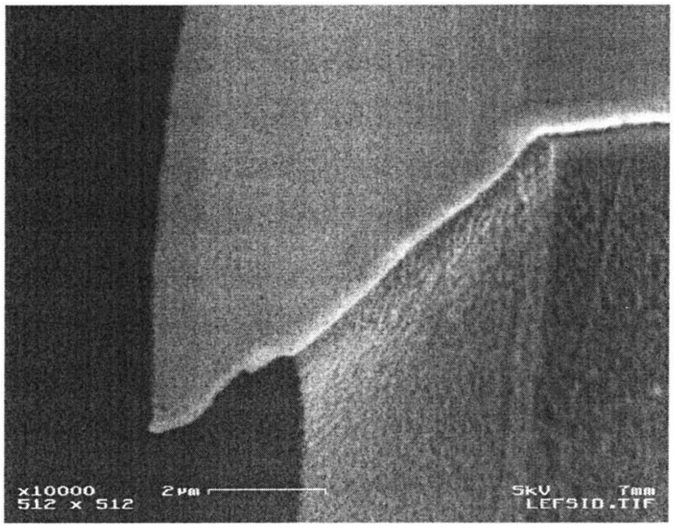

Figure 4-6: Side view of severed hinge.

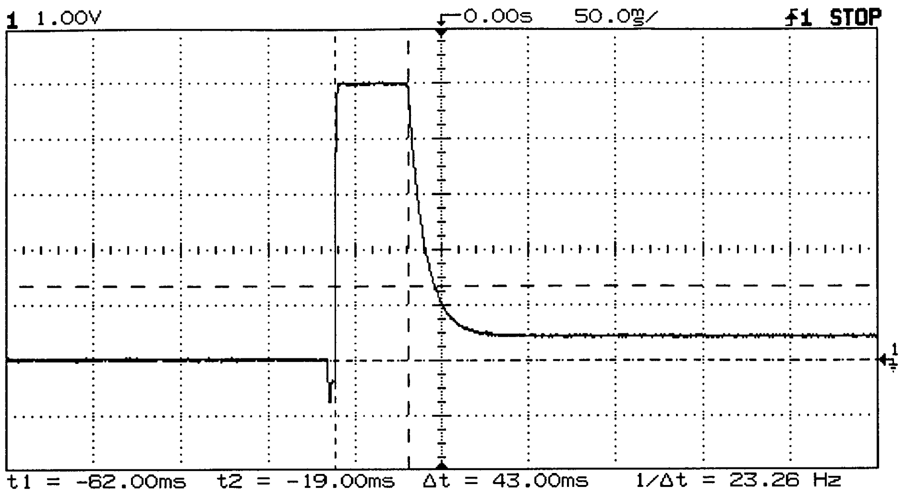

Figure 4-7: Power supply spike (voltage vs. time).

the membrane is positioned any way except horizontal. In later folding sessions, the device wafer was placed on a polished test wafer so that the shadow of the tilted membrane could be observed.

4.3 Speed of Folding

It is possible to measure the speed of folding by counting individual frames once the recorded video is digitized. Folding from just below the horizontal to 87 degrees using the RC circuit described above takes an average of 9 frames to complete. At 30 frames per second, this places the time of folding at 0.30 seconds. When the current is shut off, the membrane returns elastically to its rest angle in 30 frames for a return swing of 1 second.

4.4 Folded Angle vs Current

An important characteristic of the folding process is the relationship between the angle and the applied current. This relationship is modeled as well as characterized experimentally. The theoretical model follows directly from the dynamic model already presented in section 3.2.4. It is a simple balance between the torques produced by the current, gravity, and the restoring

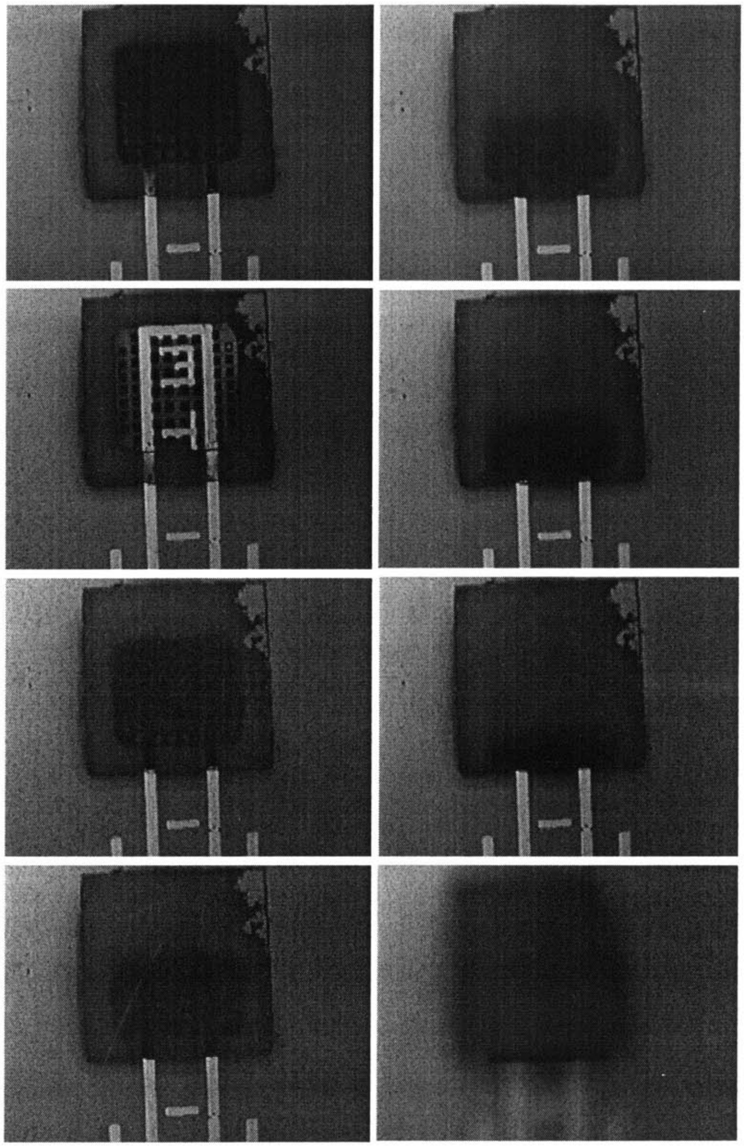

Figure 4-8: Folding sequence. Initially the membrane is bent just below the horizontal. The Lorentz force folds the flap up to nearly 90 degrees.

force of the hinge while in the elastic regime and the torque required to deform the hinge during the plastic range. The balances for the elastic and plastic regimes are

$$
\begin{aligned}
i w_p L_p B \cos\theta &= 2\left(\frac{EI}{L_h}\right)\theta + g\left(\frac{L_h + L_p}{2}\right) M_p \cos\theta && (4.1)\\
i w_p L_p B \cos\theta &= \frac{2 w_h t_h 2 \sigma_Y}{4} + g\left(\frac{L_h + L_p}{2}\right) M_p \cos\theta . && (4.2)
\end{aligned}
$$

The relationship between current and angle is nonlinear due to the cosines of the angle of bend. Thus it is non trivial to invert the function and solve for theta as a function of current. Therefore, the functions are plotted by solving for the current numerically. The first equation is used up until plastic deformation results. The relationship between current and the resulting angle is plotted in Figure 4-9 for the case of two $50\mu m$ wide and $100\mu m$ long hinges and a plastic angle of 49.4 degrees. Theory predicts that almost 0.5A of current is required to fold the flap to near ninety degrees. The dependence on $\cos\theta$ is the prime reason such a large current is required, yet folding to 90 degrees with this magnetic configuration is not needed for completing the fold. The transition between the elastic and plastic regions is clearly seen as a step at 49.4 degrees. The step is an artifact of using the maximum value for the moment required to plastically deform the hinge. The extra term in equation 3.2 was ignored due to the difficulty in predicting the thickness of the elastic core, y_Y. Had this term been included, there would be little or no step.

Experimental values for the current and angle were obtained by digitizing a video of folding at discrete currents. Currents were applied in increments of roughly one milliampere and the corresponding movement of the membrane was captured on film. The angle of the membrane was then calculated by measuring the two dimensional projection. The width of the plate was used as a reference to determine the correspondence between pixels and microns. The results are shown in Figure 4-10 for a plate with $50\mu m$ wide and $100\mu m$ long hinges.

There exists a hysteresis between the upward and downward motion. This hysteresis is repeatable and also observed in devices with different hinge dimensions. At the present time the source of the hysteresis is unknown, but conjectured to be related to the hysteresis observed in stress tests when material samples are plastically deformed, unloaded, and then stretched

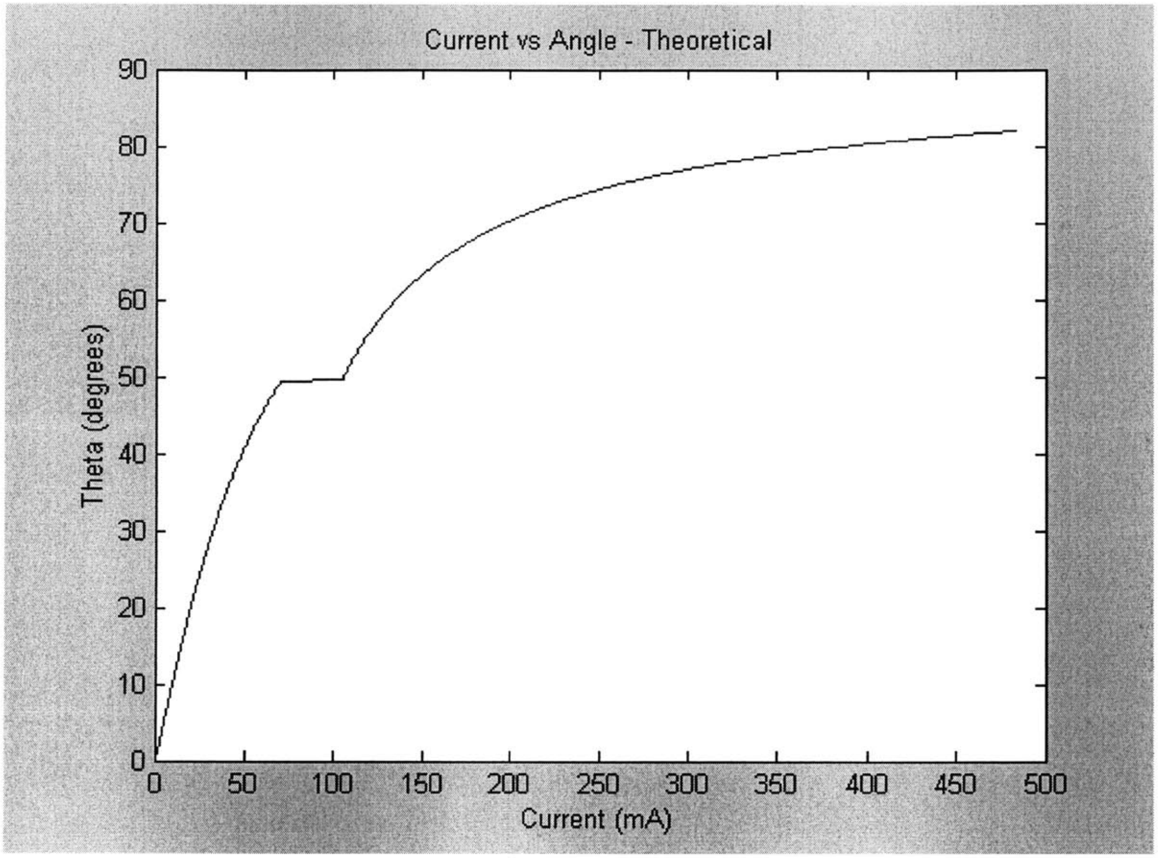

Figure 4-9: Theoretical relation between applied current and angle of bend for two 50μm wide and 100μm long hinges.

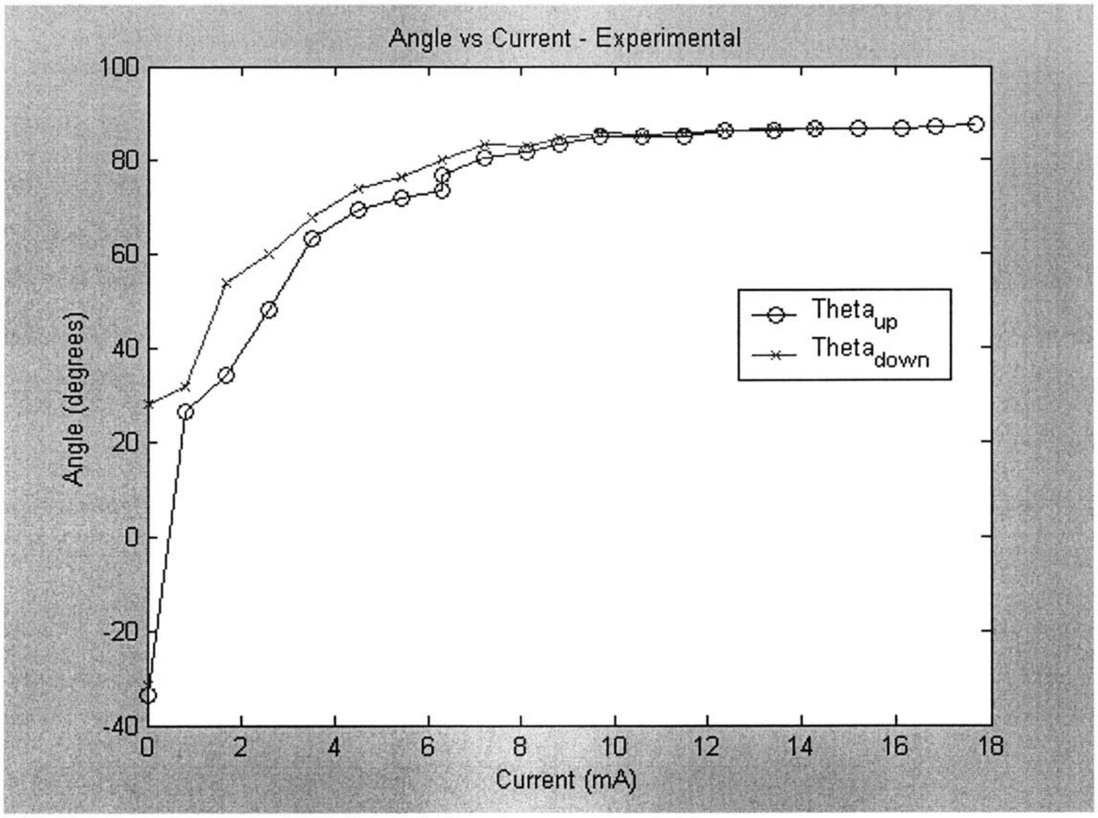

Figure 4-10: Experimental results showing the relationship between applied current and angle of bend for two 50μm wide and 100μm long hinges. Note the hysteresis between upswing and downswing.

once again.

Comparing the theoretical with the experimental it is obvious that the two do not match very well. The theoretical predicts over twenty five times as much current is needed to reach an angle of 85 degrees. The first model used the dimensions set in Table 3.4 while fabrication variations resulted in dimensions slightly smaller than those originally calculated. Yet the dimensional variations do no fully explain the discrepancy in the theoretical and experimental curves. For example, the thickness has the largest affect on the stiffness of the hinge, but to match the experimental data, the hinge in the model would have to be $0.08\mu m$ thick which is completely unreasonable because the fabricated hinges were only a few hundred angstroms less than $0.6\mu m$. The most logical explanation for the mismatch is variations in the magnetic field. Since we cannot measure the magnetic field directly in our setup, we estimated it by fitting the theoretical curve to the experimental data points and found that the magnetic field strength would be 7.8T. This is in disagreement with the manufacturer's quoted value of 0.1T in the center of the horseshoe magnet [6]. Yet in our experience this field varies dramatically with position. During one test when the face of the magnet was positioned about one centimeter from the device, only 1mA was needed to fold the flap to a vertical orientation, an increase in field strength of more than an order of magnitude. Scaling the theoretical curve by the best fit value of 7.8T shows that the experimental matches the theory as depicted in Figure 4-11.

4.5 Completing the Fold

As mentioned earlier, a full 180 degree fold using the Lorentz force requires two steps. The induced force remains perpendicular to the magnetic field and current, and so as the membrane rotates, the force remains in the vertical direction at all times. Thus, the maximum angle of bend is less than 90 degrees to the current and magnetic field vectors. The idea is to bend the hinges twice; the first time the membrane is folded to just under ninety degrees. In the process, plastic deformation occurs, the hinges yield, and once the external force is removed, the membrane relaxes to a new equilibrium rest angle. Once the flap comes to rest above the horizontal, the magnetic field is rotated ninety degrees so that the magnetic field is vertical (Figure 4-4). In this configuration the Lorentz force points in the horizontal direction and folds

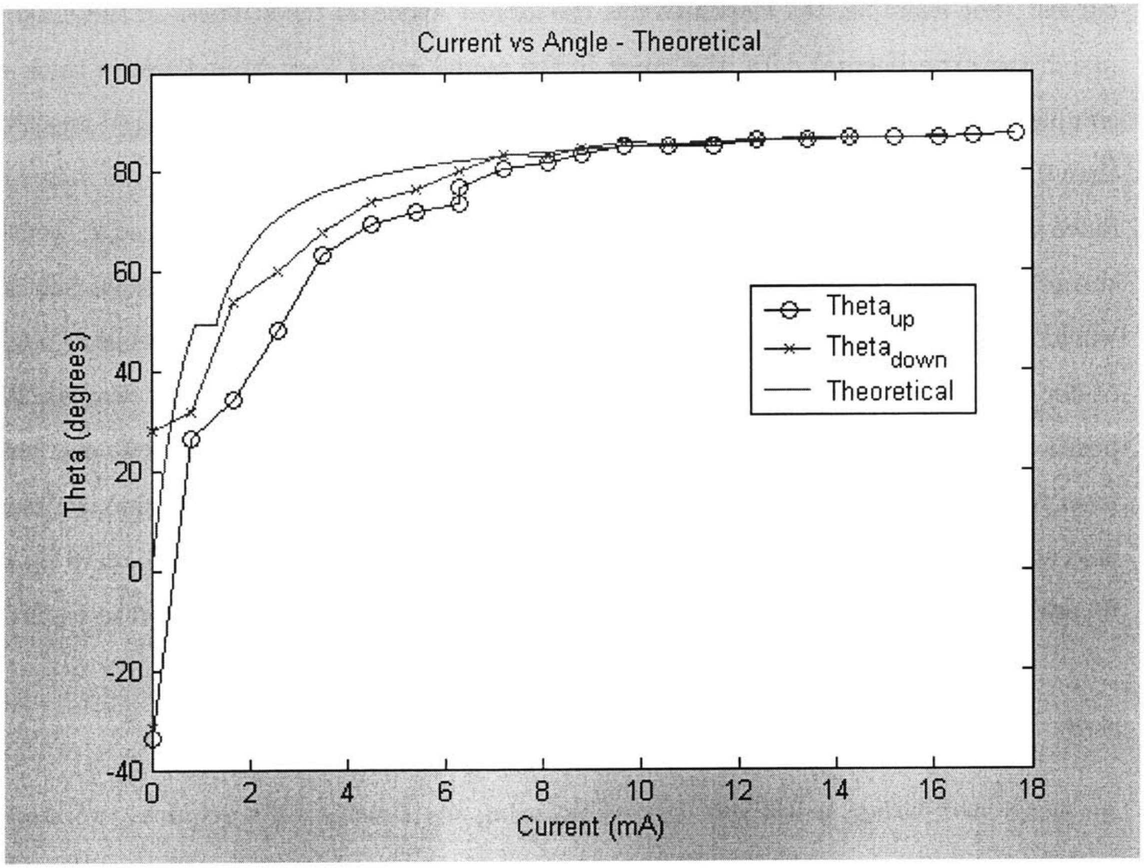

Figure 4-11: Comparisson of experimental and adjusted theoretical relationship between applied current and angle of bend.

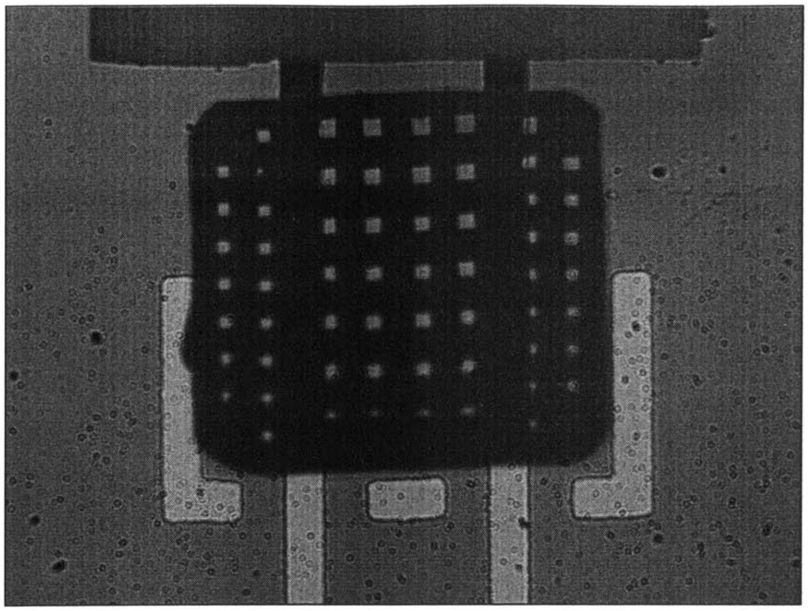

Figure 4-12: Completed fold.

the membrane to near 180 degrees. In practice, the magnet is rotated slightly more so that the Lorentz force is angled slightly downward to ensure that the membrane meets the substrate.

Unfortunately, the second fold cannot be videotaped because the horseshoe magnet blocks the field of view of the camera on the probe station. Attempts were made to buy a single magnet to place underneath the substrate to generate a perpendicular magnetic field, yet the technicians at several custom magnet vendors could not guarantee the field strength or the degree of straight field lines needed. The final result is shown in Figures 4-12 and 4-13. Note that the dark area above the flap in Figure 4-12 is the backside etch where the membrane used to reside before folding. The final position lands to within $10\mu m$ of the alignment fiducials.

The electrical properties of the wires and hinges did not change after folding to 90 or 180 degrees. The measured electrical resistance of the two probe tips and device (roughly on the order of 24Ω) did not change more than the 0.1Ω precision of the multimeter. This is preliminary experimental evidence that routing circuitry through folded hinges will not adversely affect performance. No change in the electrical impedance also indicates that no major mechanical failure occurred (if a hinge tore or the cross sectional area changed significantly it would be reflected in an increase in the resistance of the circuit).

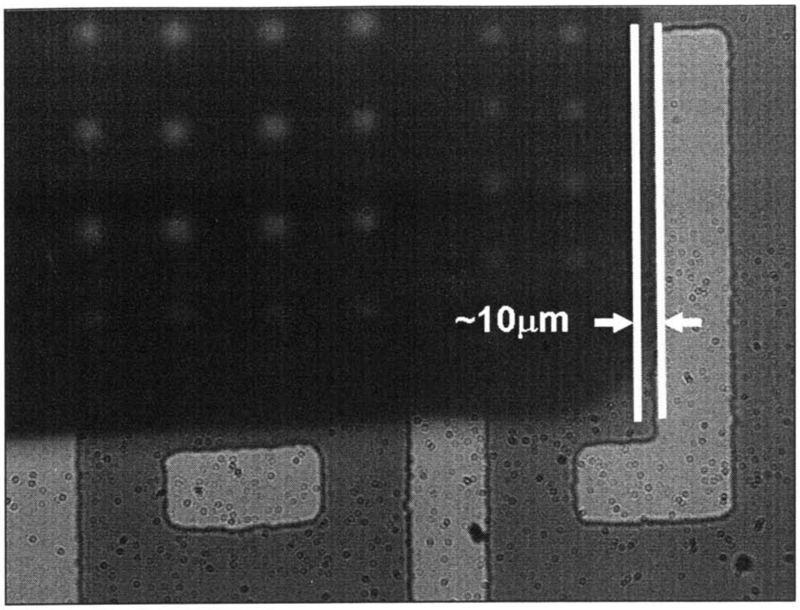

Figure 4-13: After 180 degrees of folding, the alignment is good to $10\mu m$.

4.6 Buckling

In testing half a dozen devices, most folded to 180 degrees, a couple were lost due to failure of the testing equipment, and one buckled upon folding up to 90 degrees. Just as all the devices before it, the buckled membrane began at an initial position slightly below the horizontal as seen in Figure 4-14. Upon application of the current in 1mA increments, the membrane began to fold, but before becoming horizontal, the right hinge pulled in and crumpled. The final state with force still applied is seen in Figure 4-15. When the current was turned off the membrane sprung back slightly, but the right hinge was permanently deformed (Figure 4-16). Attempts to straighten the hinge by pulling the flap with a Lorentz force in the horizontal direction proved unsuccessful.

The reason for the buckling remains unclear. One hypothesis is that the dust particle seen next to the right hinge caused some adverse effect because the particle clearly was in contact with both the substrate and the membrane. In the first image the particle appears to be attached to the substrate, while in the final image it is attached to the flap.

Another possible reason for failure is that the Cr on the right hinge was only partially

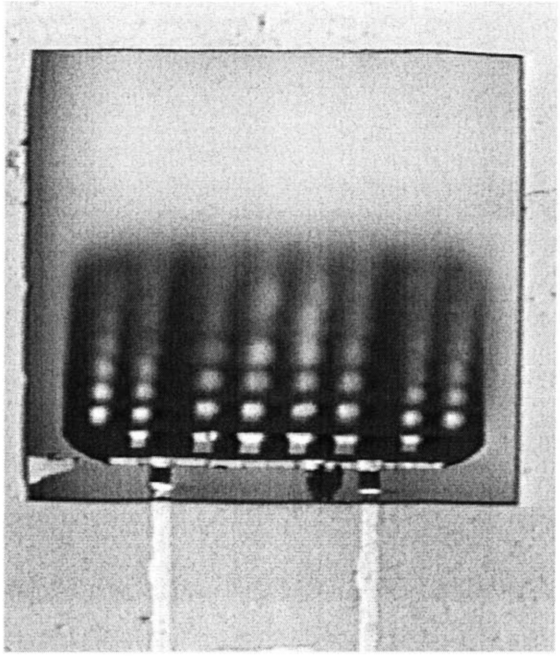

Figure 4-14: Membrane's initial position just below horizontal. Notice particle next to the right hinge.

removed during the backside oxide RIE. The chlorine chemistry used to etch the oxide also attacks Cr, and perhaps removing more Cr from one hinge than the other produced a sizeable asymmetry large enough to cause one hinge to fail. Despite this one unsuccessful actuation, the yield still remains quite acceptable for a proof of concept.

4.7 Second Round of Prototypes

Having demonstrated a proof of concept that membranes can be folded to 180 degrees without mechanical or electrical failure, it was time to begin design iteration. The objectives of the second round of are to test multiple folds, final alignment using SAMs, multiple interconnects between flaps, and increased lateral stiffness in the hinge. This series also includes the first integrated device, a Fresnel zone plate and tunable diffraction grating located on individual flaps, which will form a compound diffractive optic once folded. Each device flavor also has several variations including different hinge widths and lengths.

At the time of this writing the devices described below have been processed up to the point

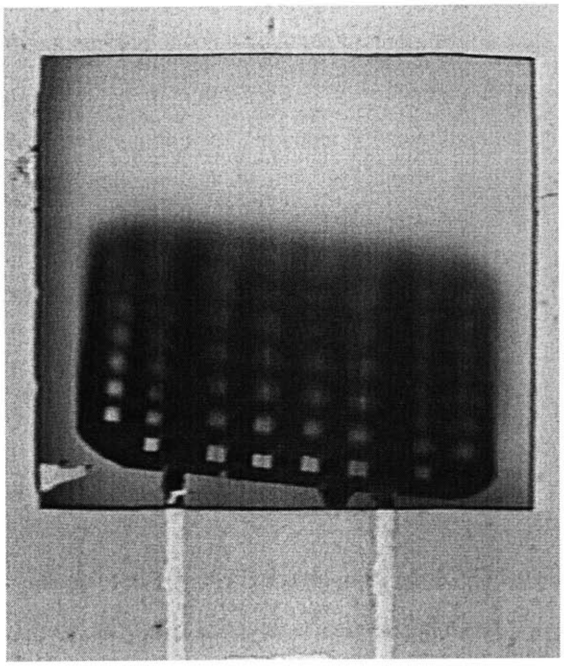

Figure 4-15: Right hinge has crumpled and membrane will not fold any further.

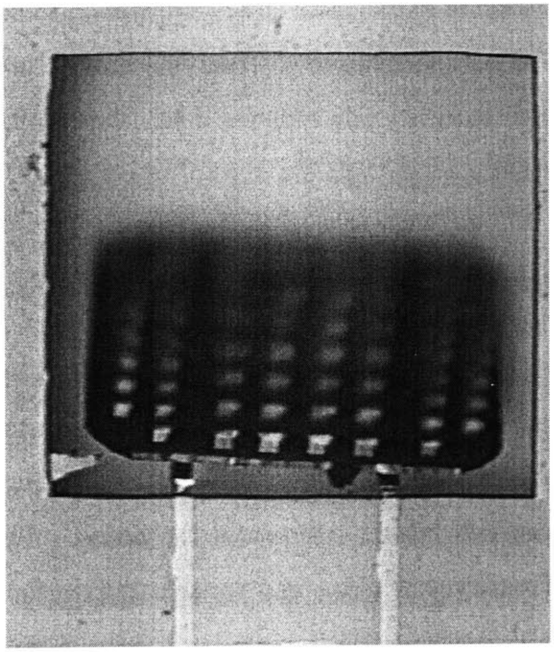

Figure 4-16: Final state without applied actuation force.

of the backside KOH etch and thus have not yet been released or tested. The mask set was written with an electron beam so that we could define features down to as small as two microns, and the features do not exhibit the waviness produced in the transparency masks.

4.7.1 Design Flavors

Multiple Folds

The question of scalability is an important issue to resolve because the savings in time and money increase dramatically as the number of layers being built in 3D goes up. As will be discussed later, the Lorentz force has some limitations when it comes to mass production of devices, and the fact that this type of actuation requires two steps for folding 180 degrees leaves something more to be desired. However, some schemes for multiple folds work well with the Lorentz force because they only require 90 degree folds instead of a full 180 degrees.

The serial and parallel folding approaches for multiple folds are presented in Figure 4-17. The serial technique is slow and requires many operations as compared to the parallel concept. The parallel fold requires only one magnetic field orientation because each membrane undergoes a single ninety degree rotation. A method for stabilizing a parallel fold is illustrated in Figure 4-18. The buried oxide and device layer of an SOI wafer can be used to create a track within which posts from each flap can travel. For the first multiple fold prototypes, we simple created a structure similar to the parallel fold of Figure 4-17 with a total of three discrete flaps. Two

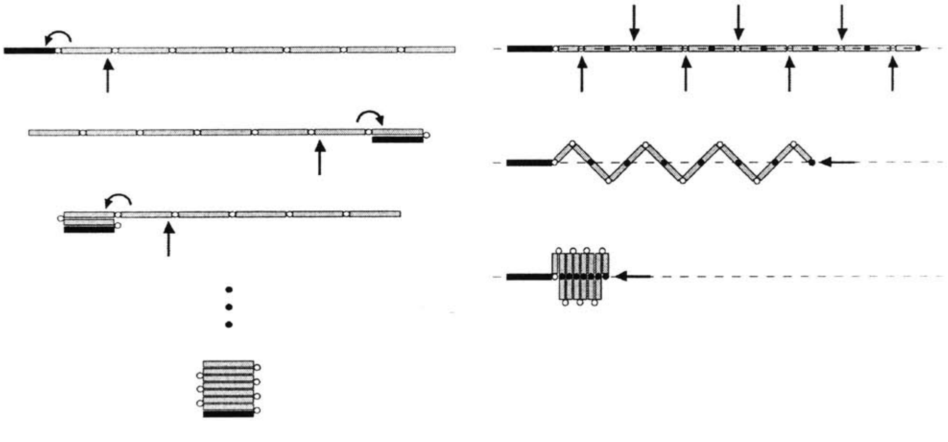

Figure 4-17: Multiple folds by serial folding (left) and parallel folding (right) [65].

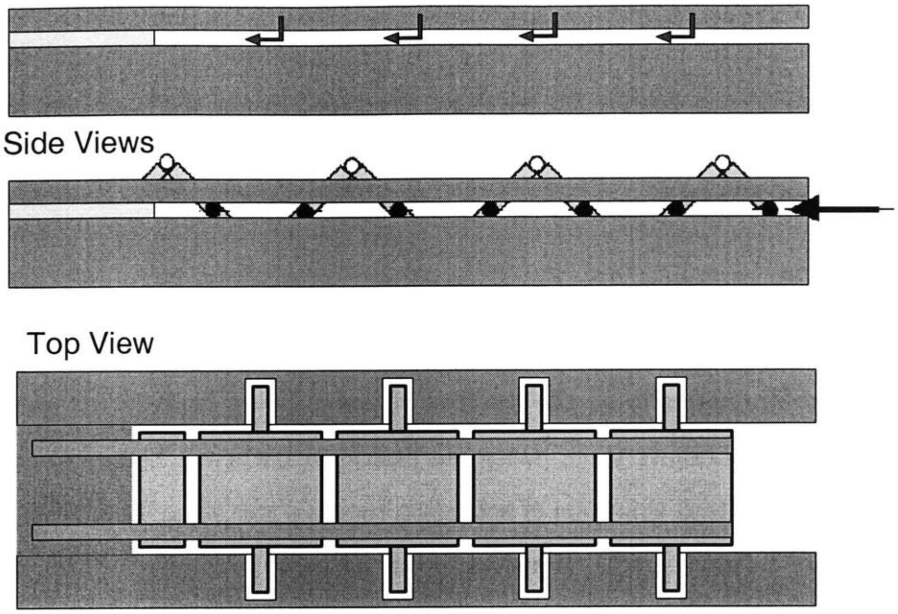

Figure 4-18: Top and side schematics of a parallel fold technique using stabilization rails created in an SOI wafer.

sets of wires are used to create current loops on each flap so that each portion of the membrane experiences a torque about its center. The mask layout is displayed in the Appendix.

A second concept for multiple folds is also included in this round of fabrication. Instead of folding as an accordion, the three flaps are to be rolled up on each other. The CAD for this design is also in the Appendix.

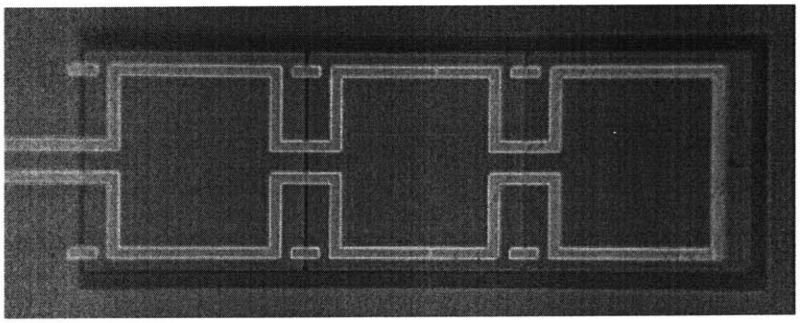

Figure 4-19: Multifold membrane prototype (second variation).

Multiple Wires

This prototype simply attempts to demonstrate that several wires can span the hinge and fold without complications such as creating electrical shorts by touching each other. In addition, multiple wires increase the lateral stiffness of the joint. These are just a single membrane with alignment fiducials similar to the ones used in the first round to aid in assessing the final alignment. This layout is displayed in the Appendix.

Fresnel Zone Plate and Tunable Grating

The first active element created by membrane folding is going to be the stacking of a binary Fresnel zone plate on top of a tunable binary diffraction grating designed by a colleague in our lab [3]. It was decided to build this example because the end result does not depend on perfect alignment of the two membranes, as we are still developing alignment techniques (see next section). This device was fabricated using electron beam written masks, therefore feature sizes as small as two microns were possible, a critical requirement for the zone plate and diffraction grating. The grating has a $12\mu m$ pitch and $600\mu m$ square aperture, and it is designed to diffract the first order from a HeNe laser by three degrees. The Fresnel zone plate contains 14 zones, has a 1cm long focal length for a HeNe laser, and the aperture is $600\mu m$ in diameter. A second zone plate designed for a $1\mu m$ IR beam was also created on some dies with twelve zones and a focal length of 6mm. These dies are displayed in the Appendix.

Alignment - Self Assembling Monolayers

Several of the multiple fold and multiple wire membranes were patterned in the center with an extra $200\mu m\times$ $200\mu m$ square of gold for the purpose of coating with a SAM. The idea is to fold the membrane almost to completion, then apply the SAM and adhesive as described in [45][46][47] and then allow the surface tension and the hydrophobic/hydrophilic interaction pull the membranes into final alignment, after which the assembly would be heated to cure the layers in place. A first order calculation reveals that the force due to surface tension (of an aqueous liquid) is one order of magnitude greater than the predicted bending moment required to fold the hinges to 180 degrees.

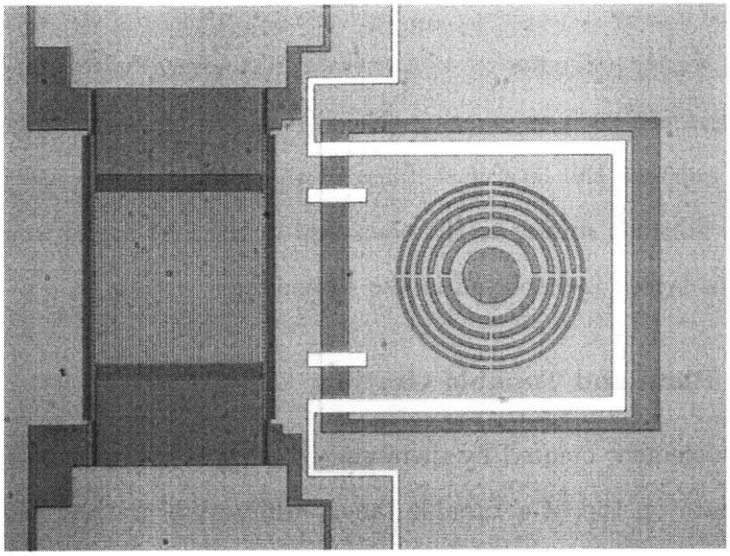

Figure 4-20: Tunable diffracting grating and Fresnel zone plate located on membrane flap.

4.7.2 Process Flow

Several changes were made to the process flow in the second round. The most visible change was the switch to 150mm (6 inch) wafers due to an almost lab-wide conversion of machines. Additionally, we wanted to test straight hinges instead of the ones created in the KOH trench. Most of the process remained the same, yet due to some unforeseen complications the KOH backside etch had to be reworked from the original process steps. The fully detailed fabrication sequence is listed in the Appendix.

An additional hypothesis for the bending of the hinges upon release (aside from residual stress mismatch between the Au and Cr layers) is that the bend at the bottom of the KOH slopes may be a contributing factor. If one thinks of a curved piece of metal as being composed of many finer strips, it is apparent that the outer strips with a larger radius of curvature are longer than the inside strips. Thus, if there is uniform residual tensile strain in the member then the outer (longer) strips will contract more than the inside ones. Upon release, the curved member will bend to balance the strains and thus increase the angle of bend. This is consistent with experimental observations. It was decided to test straight hinges in the second iteration to assess this hypothesis.

In order to build straight hinges, a planarization process was implemented. The trenches around the membranes were defined by a reactive ion etch which left near-vertical sidewalls. These trenches were then covered with PECVD oxide which was then polished back flush to the Si surface. The Au/Cr wires and hinges were then deposited and patterned using a lift-off process. The remaining fabrication sequence followed exactly that of the first round up until the KOH backside etch. For reasons that still cannot be explained, the PECVD nitride mask used in the first generation of prototypes did not work. In the end, a combination of Au and Cr worked exceptionally well.

Neither Au nor Cr are etched by KOH, and both metals are easily patterned with photoresist and their respective pre-mixed etchants. It seemed a logical choice to use them. The surface roughness of the backside of the wafer was on average 800nm, with some spikes near $1\mu m$. To avoid pinholes in the mask, 30nm of Cr followed by $1.5\mu m$ of Au were electron beam evaporated. Cr alone was not used for the reason that its high residual tensile stress and the large thickness required most likely would result in delamination and tearing at corners during the KOH etch.

The results of test wafers showed that on polished surfaces the Au/Cr mask worked perfectly with very few pinholes and no delamination or tearing (Figures 4-21 and 4-22). On the rough backside, however, the Au/Cr mask had many pinholes and was undercut at the edges. It was found that reducing the etch temperature from 80C to 65C produced better results for the same wafers (and the etch time was now over 20 hours long). It is not clearly understood why the decrease in temperature prevents the undercutting and pinholes.

Migrating to an Au/Cr mask created some problems further down the process line because PDMS does not adhere well to Au. Thus many times KOH leaked in between the PDMS and gold, destroying devices on the front of the wafer. The solution was to use a ring of electronics grade epoxy to surround the perimeter of the wafer because it adheres well to the Au, and then coat the wafer and epoxy with PDMS. The epoxy effectively acted as a dam, preventing KOH from leaking in, and the PDMS bonds to the epoxy quite well. Once the KOH etch is complete, the epoxy is removed in piranha. The PDMS covers the delicate features so that bubbles in the piranha cannot latch on and break them. The PDMS is removed in CCR dissolver. The final step is the backside RIE of the oxide, which at the time of this writing has not yet been completed.

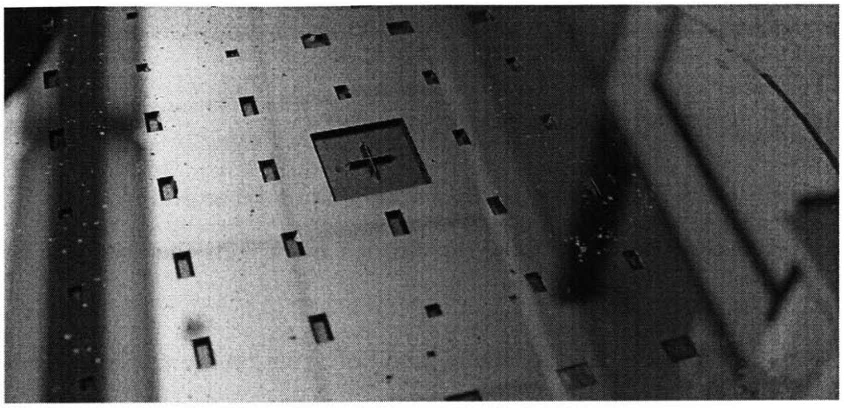

Figure 4-21: View of the Au/Cr KOH mask. Features are nominally 1.5mm, except the large feature measuring 10mm on a side.

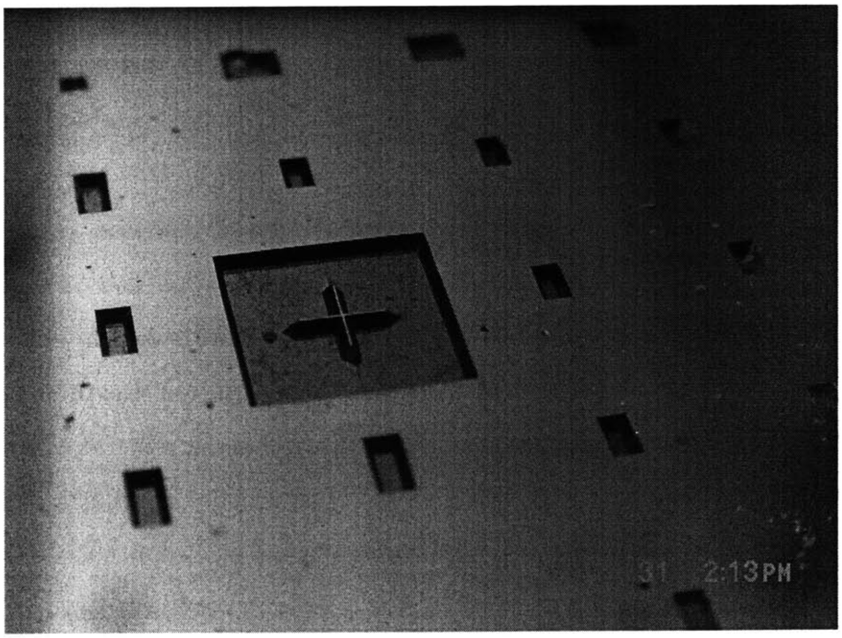

Figure 4-22: Close up showing the precision edges created with the Au/Cr KOH mask.

Chapter 5

Residual Stress Folding

As previously mentioned residual stress looks to be a promising means of actuation for membrane folding. Due to the conditions during fabrication, it is possible to tune the amount of residual stress in a thin film, sometimes even changing it from being tensile to compressive. If enough stress is produced, and if there is enough strain mismatch between two layers then folding to 180 degrees is very likely, as evidenced by Figures 2-11 and 2-10. We conducted two preliminary tests on folding by residual stress.

The first test was a quick proof of concept. A bilayer was built up of $1\mu m$ thick nitride and 50Å of Cr. Nitride strands were recovered from a shattered x-ray lithography mask from the Nanostructures Laboratory at MIT, and hence, the $1\mu m$ nitride was stress free. A shadow mask (comprised of microscope slide covers) left only an area of a few millimeters exposed at the end of the nitride strands. After electron beam evaporation of Cr, the strands were bent into the air by 33 degrees. Figure 5-1 shows before and after photos of the nitride strands. Note that the entire cantilever is in focus to begin and afterwards the cantilever base and tip are at two different heights. Examining this cantilever on its side, the angle of bend is 33 degrees (Figure 5-2). This was a simple afternoon experiment, and due to the test set-up it was impossible to quantify the magnitude of residual stress in the Cr. If the nitride strand had any compressive residual stress, the angle of bend would have been even larger. This is what we tried in the next experiment.

The second experiment on residual stress aimed to be more accurate with respect to metrology and measurement. In the first run, we demonstrated that bending can be accomplished by

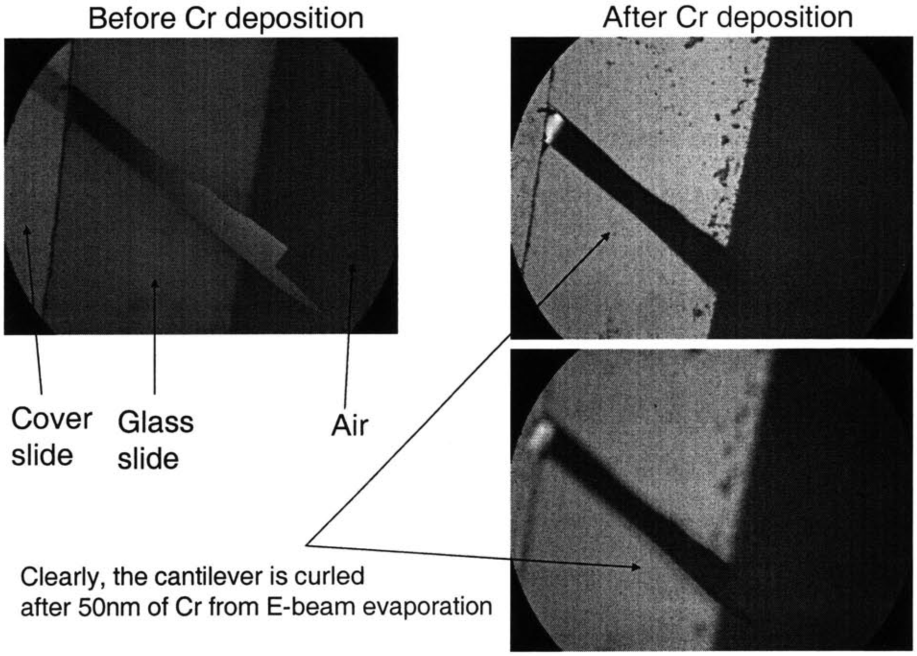

Clearly, the cantilever is curled after 50nm of Cr from E-beam evaporation

Figure 5-1: Before and after photos (top view) of a $1\mu m$ thick nitride strand covered by 50Å of Cr.

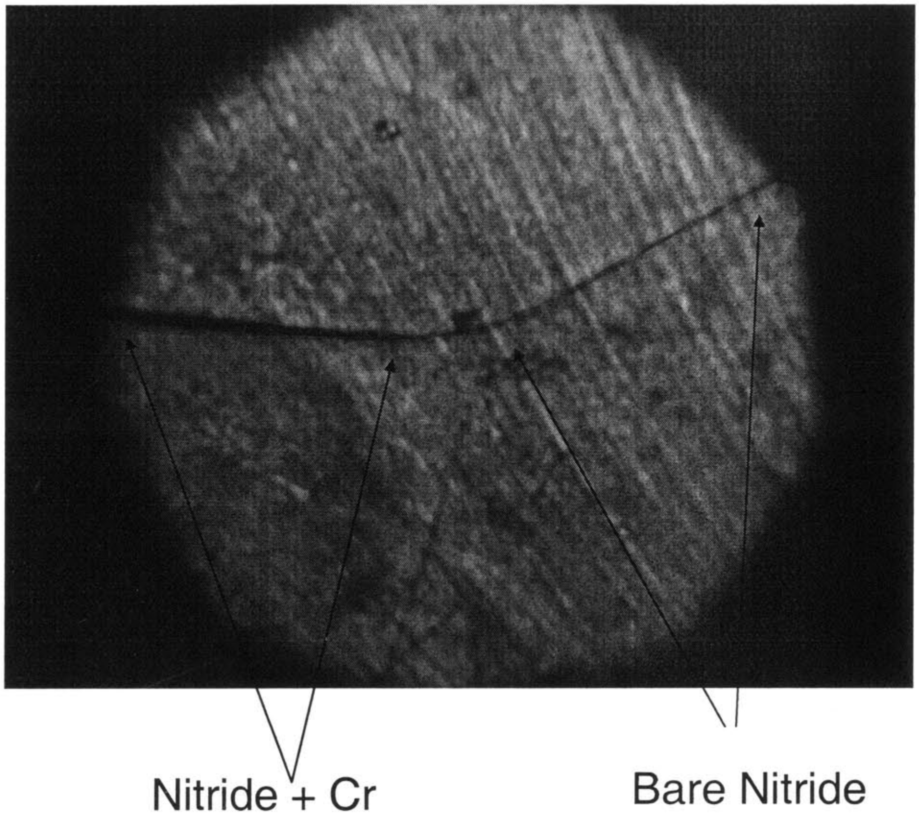

Figure 5-2: Side view of same cantilever. Measuring the angle of bend places it at 33 degrees.

residual stress, however, we were unable to obtain any data on the stresses involved. For this reason we fabricated a series of cantilevers and other geometries on a silicon wafer to better quantify the stresses and important parameters.[1] The cantilevers are composed of PECVD nitride covered by Cr which was electron beam evaporated. PECVD nitride was chosen because the deposition parameters can be tuned so that the film has a compressive residual stress unlike many other available materials. Cr was chosen because it exhibits one of the highest tensile residual stresses of electron beam evaporated metals. Before and after each deposition the stress in the film was measured using a Tencor Flextester, which measures the wafer bow. Nitride was deposited with thicknesses of 500Å and 1000Å with 40MPa and 90MPa average compressive stress respectively. 270Å of Cr was deposited with a resulting tensile stress of 800GPa.

We released the cantilevers with a XeF_2 silicon isotropic etcher. The PECVD nitride was suppose to form a suitable mask for the etch, however we discovered that it was quickly etched away. Despite this problem, we were able to partially release the cantilevers, though they were now absent of any nitride. Curling was observed as seen in Figures 5-5 and 5-6, most likely due to a stress gradient in the Cr. There is some literature that indicates oxidation of metals can induce stress gradients [66], though we have not yet confirmed that this in fact is what led to the observed curls. Two important lessons were learned in this experiment. First, PECVD nitride is indeed etched by XeF_2, and perhaps more importantly, even though these cantilevers were not fully released, it is clear that structural elements are needed to channel the direction of folding. If undercutting continued, the cantilevers would have shriveled into a disordered mess rather than making nice swiss roles as hoped. Thus some sort of anisotropy is needed along the cantilevers so that the correct type of folding is achieved.

---

[1] This work was conducted with the help of Johnathan G. Niemczura, MIT '03. A more detailed explanation of the experiment and simulations can be found in his senior thesis, "Material Study for Nanostructured Origami."

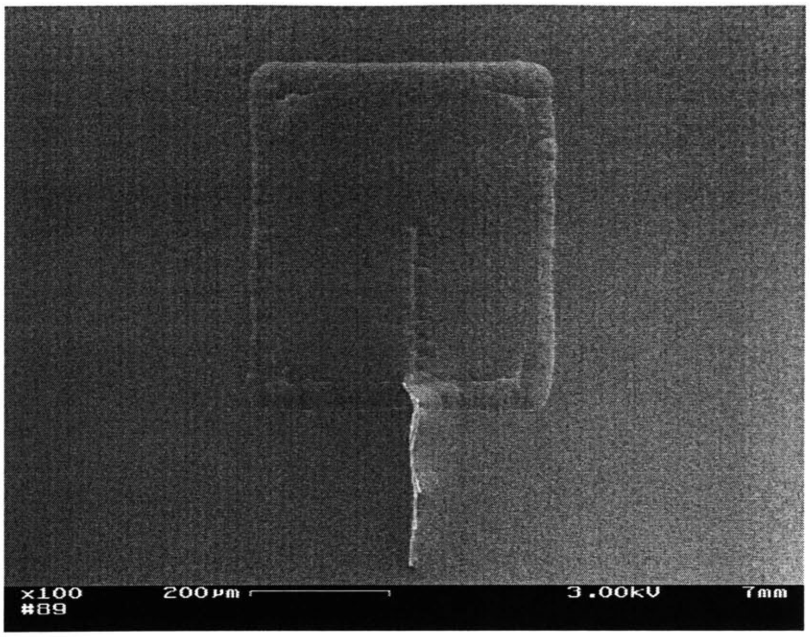

Figure 5-3: This $50\mu m$ wide cantilever is missing after the XeF_2 completely etched away the nitried underneath the Cr. Some Cr can be seen curling on the substrate below the pit.

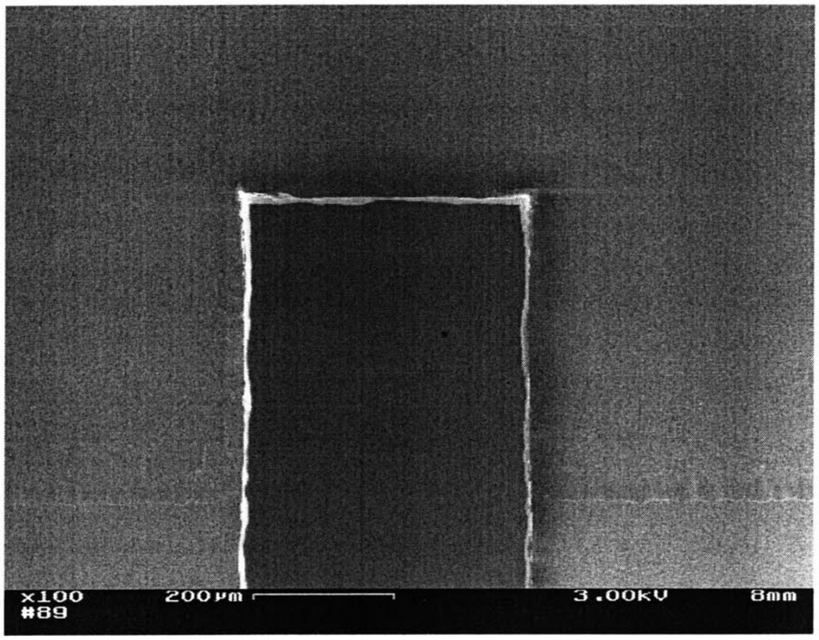

Figure 5-4: Only the edges of this wider cantilever were undercut (the bright edge). The nitride was also removed underneath the Cr. Close ups of this edge are shown in Figures 5-5 and 5-6.

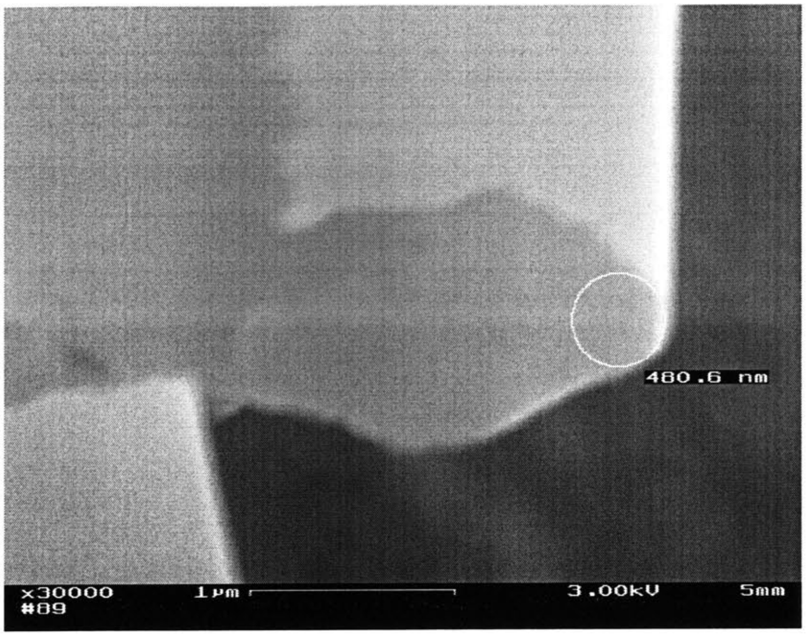

Figure 5-5: 50Å thick Cr curling with a radius on the order of 250nm.

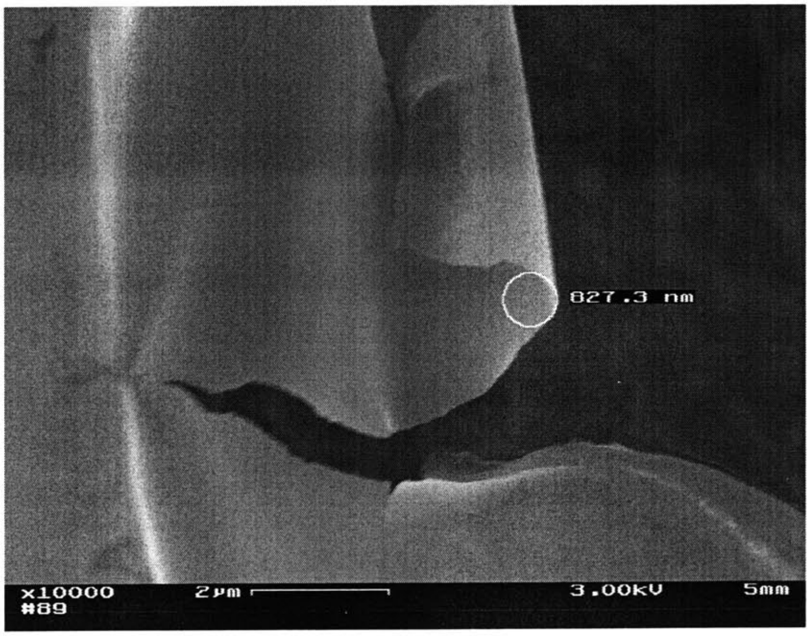

Figure 5-6: 50Å thick Cr curl with radius on the order of 400nm.

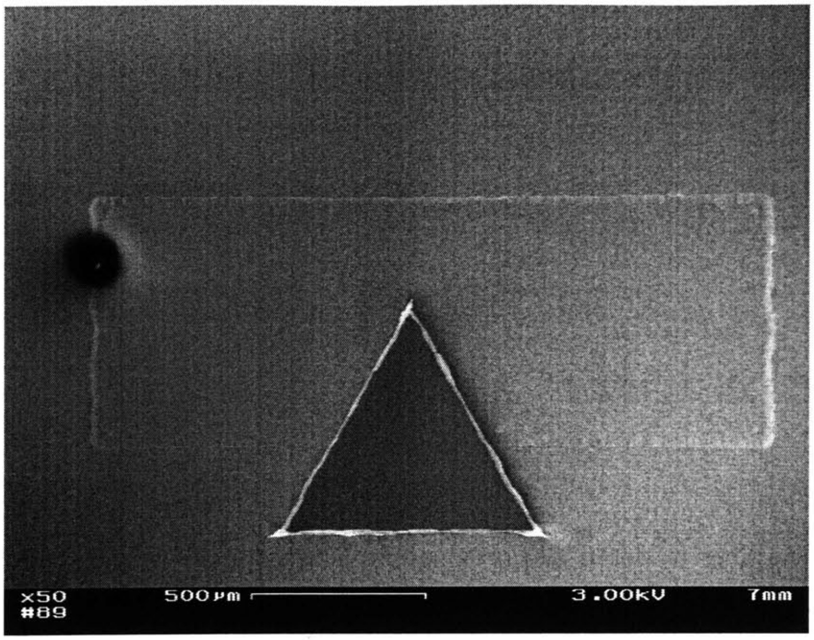

Figure 5-7: Similar to the rectangluar canitlever above, this triangular cantilever was only undercut near the edges.

Figure 5-8: Close up of the tip of the triangle in Figure 5-7, showing curling only at the immediate edge.

Chapter 6

Conclusions

This thesis outlines in detail the reasons why membrane folding is a promising approach to micro and nanomanufacturing in 3D. The functional requirements for successful 3D micro and nanostructures were listed, which membrane folding satisfies better than any other proposed 3D technology. The design of folding membranes was presented, beginning with design solutions to meet the needs of the functional requirements of folding, all the way to the implementation of the design through microfabrication of the first prototypes. Modelling and simulation results were presented, which the working prototype successfully surpassed. Folding takes place within a fraction of a second, and we have demonstrated that folding to 180 degrees can be done repeatably with no mechanical or electrical failure, and with accuracy as good as $10\mu m$. It is believed that the precision in alignment will increase by at least an order of magnitude in the next round of prototypes, which include surface chemistry techniques using self assembling monolayers.

The decoupled nature of the fabrication and assembly into 3D means that membrane folding is a general purpose technology suitable for microelectronics, MEMS, and nano applications. It is our hope that membrane folding combined with other nanotechnologies, such as templated self assembly, may revolutionize nanotechnology and the way in which people think about the third dimension. The flexibility of fabrication and the densities possible will be hard to match with any other technology.

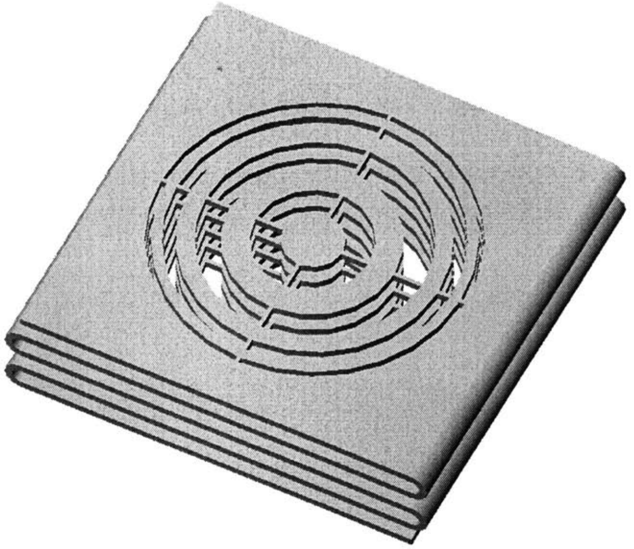

Figure 6-1: 3D DOE solid model representation. Each layer is a Fresnel zone plate with a specific focal length.

6.1 Applications and Future Work

Now that membrane folding in its most basic form is better understood, it is time to use it as a building block for the creation of functionally more complex structures. Integration of MEMS devices, multiple folds, folding by residual stress, and advances in alignment are well on their way to being realized and tested.

One of the first applications of membrane folding will be 3D diffractive optical elements or 3D DOES. One type of 3D DOE is a synthetic or digital volume hologram (Figure 6-1). It is composed of many layers, each with a Fresnel zone plate. Each zone plate focuses the first diffracted order to a common focal plane. The higher orders essentially are Bragg mismatched and cancel (the more layers, the better). Thus the diffraction efficiency approaches 100% and cross talk from the higher orders is eliminated.

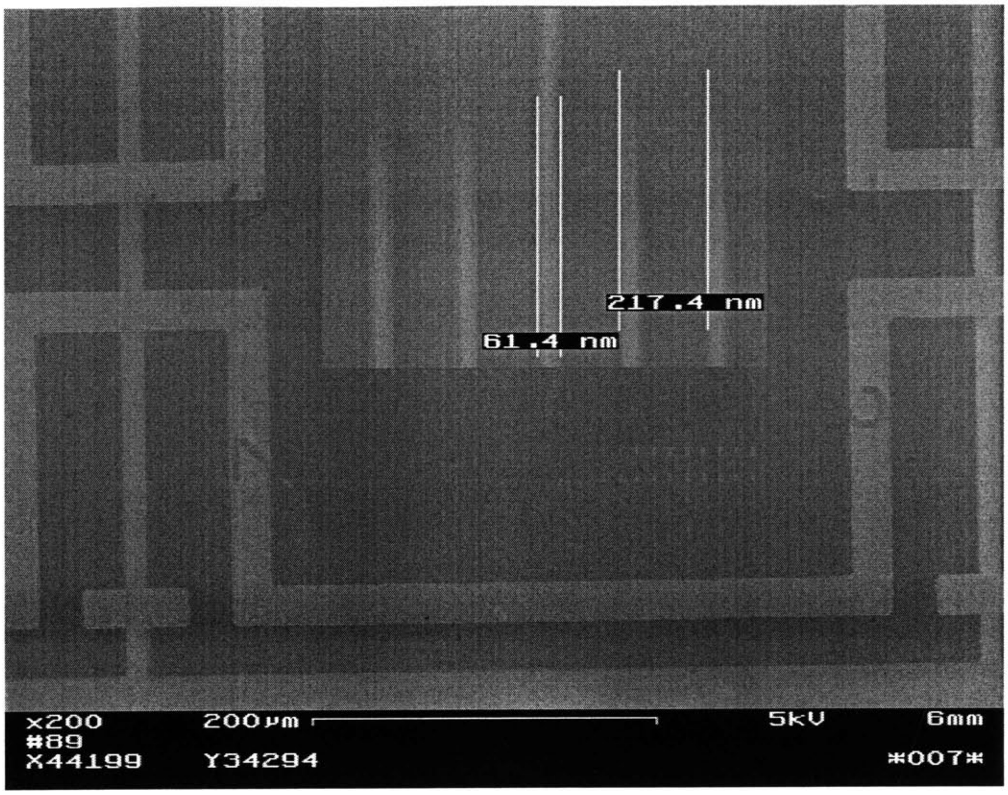

Figure 6-2: Top view seen with SEM showing the larger membrane ($500\mu m$) with nanopatterned structures in HSQ. The tiny dots are arrays of nanogratings and other shapes. The inset image is a close up of one of the gratings.

6.2 Nanostructured Origami

We have already begun integrating nanofeatures on membranes before folding. The vision is to nanopattern these planar flaps and then fold them into dense 3D configurations. Using an electron beam we wrote nanopatterns in hydrogen silsesquioxane (HSQ), a negative resist, as seen in Figure 6-2.[1]

The gold wires and hinges are the wider line structures. The arrays of dots are areas in which gratings and nano patterns were exposed and developed. The inset square shows a close up of one of the gratings with a period of 217nm and grating size of 61nm.

In the future we hope to expand this technology to areas such as 3D photonic crystals, 3D

---

[1] Mark Modol, research scientist with the Nanostructures Laboratory, MIT, was instrumental in creating the nanopatterns with the electron beam system, VS26.

optical circuits, and 3D microprocessors. Capacitors, batteries, and fuel cells, all with higher energy densities than what is currently available can be achieved with membrane folding and nanopatterning.

Bibliography

[1] Brian A. Wandell, *Foundations of Vision*, Sunderland, MA., Sinauer Associates, 1995.

[2] Ferdinand P. Beer and E. Russel Johnston, Jr., *Mechanics of Materials; Second Edition*, New York, McGraw-Hill, Inc., 1992.

[3] W. C. Shih, C. W. Wong, Y. B. Jeon, S. G. Kim, G. Barbastathis, *Electrostatic and Piezoelectric Analog Tunable Diffractive Gratings,* Conference of lasers and electro-optics / quantum electronics and laser science, Long Beach, CA, May 2002.

[4] J. Q. Broughton, C. A. Meli, P. Vashista, and R. K. Kalia, Phys. Rev. B 56, 611, 1997.

[5] Matthew Varghese, PhD MIT 2001, EECS Department., Personal communication, September 2001.

[6] Dexter Magnetic Technologies, 229 Billerica Road, Chelmsford, MA 01824. http://www.dextermag.com/index.html

[7] Specification sheet from Analog Devices listing available SOI wafers and their properties.

[8] URL: http://www.ai.mit.edu/people/tk/tks/silicon-thermal.html

[9] R. G. Craig, ed. *Restorative Dental Materials; 9th ed.*, St. Louis: C. V. Mosby, 1993.

[10] Niels Tas, et al., *Stiction in Surface Micromachining*, J. Micromech. Microeng. 6, 385-397, 1996.

[11] Amy Duwel, et al., *Quality Factors of MEMS Gyros and the Role of Thermoelastic Damping*, The Fifteenth IEEE International Conference on Micro Electro Mechanical Systems, 214-219, 2002.

[12] Ron Lifshitz, et al., *Thermoelastic Damping in Micro- and Nanomechanical Systems*, Physical Review B, Vol. 61, No. 8, 5600 (2000).

[13] S. Kobayashi, et al., *Shape Effect on Mechanical Quality Factor of Micro-Resonator*, The Eleventh Annual International Workshop on Micro Electro Mechanical Systems, 195-200, 1998.

[14] V. T. Srikar and Stephen D. Senturia, *Thermoelastic Damping in Fine-Grained Polysilicon Flexural Beam Resonators*, J. MEMS, Vol. 11, No. 5, 499, 2002.

[15] David C. Wilcox, *Basic Fluid Mechanics; First Edtition*, DCW Industries, Inc., 1997.

[16] James A. Fay, *Introduction to Fluid Mechanics*, Cambridge, MA, MIT Press, 1994.

[17] URL: http://www.memsnet.org/material

[18] Jun Zou, Jack Chen, and Chang Liu, *Plastic Deformation Magnetic Assembly (PDMA) Of 3D Microstructures: Technology Development and Application*, Transducers '01, The 11th International Conference on Solid-State Sensors and Actuators, Munich, Germany, June 10 - 14, 2001.

[19] Jun Zou, Jack Chen, Chang Liu, and Jóse E. Schutt-Ainé, *Plastic Deformation Magnetic Assembly (PDMA)*, Journal of Microelectromechanical Systems, Vol. 10, No. 2, JUNE 2001.

[20] Hans C. Ohanian, *Physics; Second Edition, Expanded*, New York, Norton and Company, 1989.

[21] Schmidt Group Laboratory, Building 39, MIT.

[22] A. Lu and K. Komvopoulos, *Nanomechanical and Nanotribological Properties of Carbon, Chromium, and Titanium Carbide Ultrathin Films*, Journal of Tribology, Vol 123, 717, 2001.

[23] X. Zhang, X.N. Jiang, and C. Sun, *Micro-Stereolithography of Polymeric and Ceramic Microstructures*, Sensors and Actuators 77, 149-156, 1999.

[24] Shoji Maruo and Satoshi Kawata, *Two-Photon-Absorbed Photopolymerization for Three-Dimensional Microfabrication*, Tenth Annual Proceedings, IEEE., Micro Electro Mechanical Systems, 1997.

[25] Thomas H. Lee, *A Vertical Leap for Microchips*, Scientific American, January 2002.

[26] Kanna Aoki, T. Ideki, et. al., *Microassembly of Semiconductor Three Dimensional Photonic Crystals*, Nature Materials, Vol. 2, February 2003.

[27] Andreas Terfort and George Whitesides, *Self-Assembly of an Operating Electrical Circuit Based on Shape Complementarity and the Hydrophobic Effect*, Advanced Materials, 10, No. 6, 1998.

[28] Ned Bowden, Andreas Terfort, Jeff Carbeck, and George Whitesides, *Self-Assembly of Mesoscale Objects into Ordered Two-Dimensional Arrays*, Science, Vol. 276, April 1997.

[29] Tricia L. Breen, Joe Tien, et. al., *Design and Self-Assembly of Open, Regular, 3D Mesostructures*, Science, Vol. 284, May 1999.

[30] Elliot E. Hui, Roger T. Howe, and M. Steven Rodgers, *Single-Step Assembly of Complex 3-D Microstructures*, The Thirteenth Annual International Conference on Micro Electro Mechanical Systems, 2000.

[31] Richard Syms, *Surface Tension Powered Self-Assembly of 3-D Micro-Optomechanical Structures*, Journal of Microelectromechanical Systems, Vol. 8, No. 4, December 1999.

[32] Isao Shimoyama, Osamu Kano, Hirofumi Miura, *3D Micro-structures Folded by Lorentz Force*, The Eleventh Annual International Workshop on Micro Electro Mechanical Systems, 1998.

[33] Raphael Holzer, Isao Shimoyama, Hirofumi Miura, *Lorentz Force Actuation of Flexible Thin-Film Aluminum Microstructures*, IEEE/RSJ International Conference on Intelligent Robots and Systems 95. 'Human Robot Interaction and Cooperative Robots', Vol. 2, 1995.

[34] Raphael Holzer, Isao Shimoyama, Hirofumi Miura, *Hybrid Electrostatic-Magnetic Microactuators*, IEEE International Conference on Robotics and Automation, 1995.

[35] Eiji Iwase, Shoji Takeuchi, and Isao Shimoyama, *Sequential Batch Assembly of 3-D Microstructures with Eleastic Hinges by a Magnetic Field*, The Fifteenth IEEE International Conference on Micro Electro Mechanical Systems, 2002.

[36] Raj Sood, Micro-Nano Systems Laboratory, MIT.

[37] Tim Savas, Nanostructures Laboratory, MIT.

[38] Jack W. Judy, Richard S. Muller, *Magnetic Microactuation of Torsional Polysilicon Structures*, Sensors and Actuators A 53, 392-397, 1996.

[39] Jack W. Judy, Richard S. Muller, *Magnetically Actuated, Addressable Microstructures*, Journal of Microelectromechanical Systems, Vol. 6, No. 3, September 1997.

[40] Nam Pyo Suh, *Axiomatic Design: Advances and Applications*, Oxford University Press, 2001.

[41] Elisabeth Smela, Matthias Kallenbach, and Jens Holdenried, *Electrochemically Driven Polypyrrole Bilayers for Moving and Positioning Bulk Micromachined Silicon Plates*, Journal of Microelectromechanical Systems, Vol. 8, No. 4, December 1999.

[42] Angad Singh, David Horsley, Michael Cohn, Albert Pisano, Roger Howe, *Batch Transfer of Microstructures Using Flip-Chip Solder Bonding*, Journal of Microelectromechanical Systems, Vol.8, No. 1, March 1999.

[43] A. H. Slocum, *Precision Machine Design*, Dearborn, Society of Manufacturing Engineers, 1995.

[44] Alexis C. Weber, *Precision Passive Alignment of Wafers*, Master of Science in Mechanical Engineering Thesis, MIT, February 2002.

[45] Uthara Srinivasan, Michael Helmbrecht, et. al., *Fluidic Self-Assembly of Micromirrors onto Surface Micromachined Actuators*, IEEE/LEOS International Conference on Optical MEMS, 2000.

[46] Karl Bohringer, Uthara Srinivasan, and Roger Howe, *Modeling of Capillary Forces and Binding Sites for Fluidic Self-Assembly*, The 14th IEEE International Conference on Micro Electro Mechanical Systems, 2001.

[47] Uthara Srinivasan, Dorian Liepmann, and Roger T. Howe, *Microstructure to Substrate Self-Assembly Using Capillary Forces*, Journal of Microelectromechanical Systems, Vol.10, No. 1, March 2001.

[48] Gary Fedder, Roger Howe, *Thermal Assembly of Polysilicon Microstructures*, IEEE Proceedings, Micro Electro Mechanical Systems, 'An Investigation of Micro Structures, Sensors, Actuators, Machines and Robots,' 1991.

[49] Vincent Agache, Lionel Buchaillot, Emmanuel Quevy, and Dominique Collard, *Stiction-Controlled Locking System for Three-Dimensional Self-Assembled Microstructures: Theory and Experimental Validation*, Proceedings of SPIE, Vol. 4408, 2001.

[50] URL: http://www.conservation.state.mo.us/conmag/1996/oct/7.html

[51] URL: http://webvision.med.utah.edu/VisualCortex.html

[52] URL: http://www.cs.utexas.edu/users/jbednar/papers/bednar.thesis/node6.html

[53] V. A. Casagrande, and T. T. Norton, *Lateral Geniculate Nucleus: A Review of its Physiology and Function.* In Leventhal, A. G., editor, *The Neural Basis of Visual Function*, Vol. 4 of *Vision and Visual Dysfunction*, 41-84. Boca Raton, Florida, CRC Press.

[54] G. H. Henry, *Afferent Inputs, Receptive Field Properties and Morphological Cell Types in Different Laminae of the Striate Cortex.* In Leventhal, A. G., editor, *The Neural Basis of Visual Function*, vol. 4 of *Vision and Visual Dysfunction*, 223-245. Boca Raton, Florida, CRC Press.

[55] Rajeev Ram, Physical Optics and Electronics Group, Professor EECS Department, MIT, Personal communication, April 2001.

[56] Amtex Chemical Company, 890 Fern Hill Rd., West Chester, PA, 19380.

[57] M. Campbell, D.N. Sharp, A.J. Tuberfield, et. al., *Fabrication of Photonic Crystals for the Visible Spectrum by Holographic Lithography*, Nature, Vol. 404, March 2000.

[58] Bill Chou, Solomon Beilin, Hunt Jiang, et. al., *Multilayer High Density Flex Technology*, Electronic Components and Technology Conference, IEEE, 1999.

[59] Kenji Suzuki, Isao Shimoyama, Hirofumi Miura, *Insect-Model Based Microrobot with Elastic Hinges*, Journal of Microelectromechanical Systems, Vol. 3, No. 1, March 1994.

[60] Pablo Vaccaro, Kazuyoshi Kubota, Tahito Aida, *Strain-driven Self-positioning of Micromachined Structures*, Applied Physics Letters, Vol. 78, No. 19, May 2001.

[61] Frank P. Incropera and David P. DeWitt, *Fundamentals of Heat and Mass Transfer; Fourth Edition*, New York, John Wiley & Sons, 1996.

[62] Serope Kalpakjian, Steven Schmid, *Manufacturing Engineering and Technology; Fourth Edition*, Upper Saddle River, NJ, Prentice Hall, 2001.

[63] Arifur Rahman, Shamik Das, Anantha P. Chandrakasan, and Rafael Reif, *Wiring Requirement and Three-Dimensional Integration Technology for Field Programmable Gate Arrays*, IEEE Transactions on Very Large Scale Integration (VLSI) Systems, Vol. 11, No. 1, February 2003.

[64] Artwork by George Barbastathis, Assistant Professor of Mechanical Engineering, Optical Engineering Group, MIT.

[65] Artwork by Dr. Carlos Hidrovo, Optical Engineering Group, MIT.

[66] H. K. Pulker, *Mechanical Properties of Optical Films*, Thin Solid Films; Metallurgical and Protective Coatings, 89, 191-204, 1982.

Appendix A

Transparency Mask Layout - First Prototypes

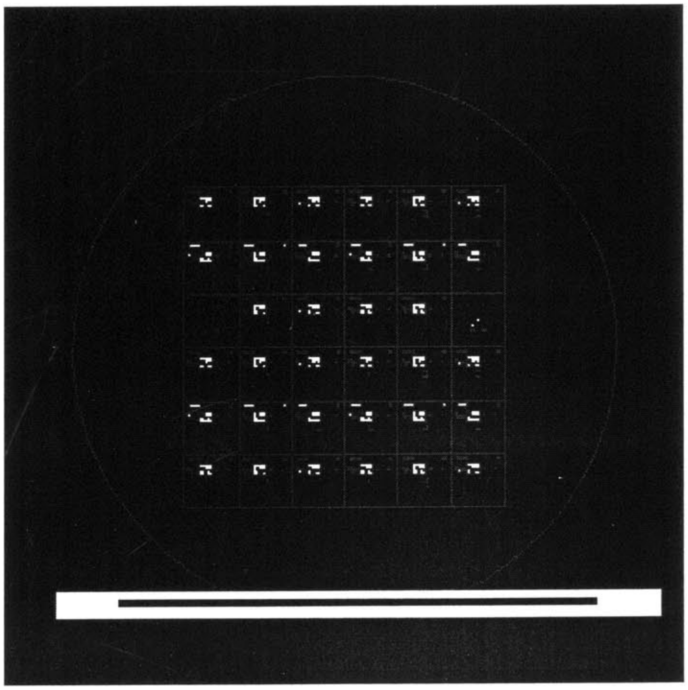

Figure A-1: Mask 1: defines KOH trenches in Si. Note the lines on the bottom for use in aligning the KOH mask to the major flat of the wafer.

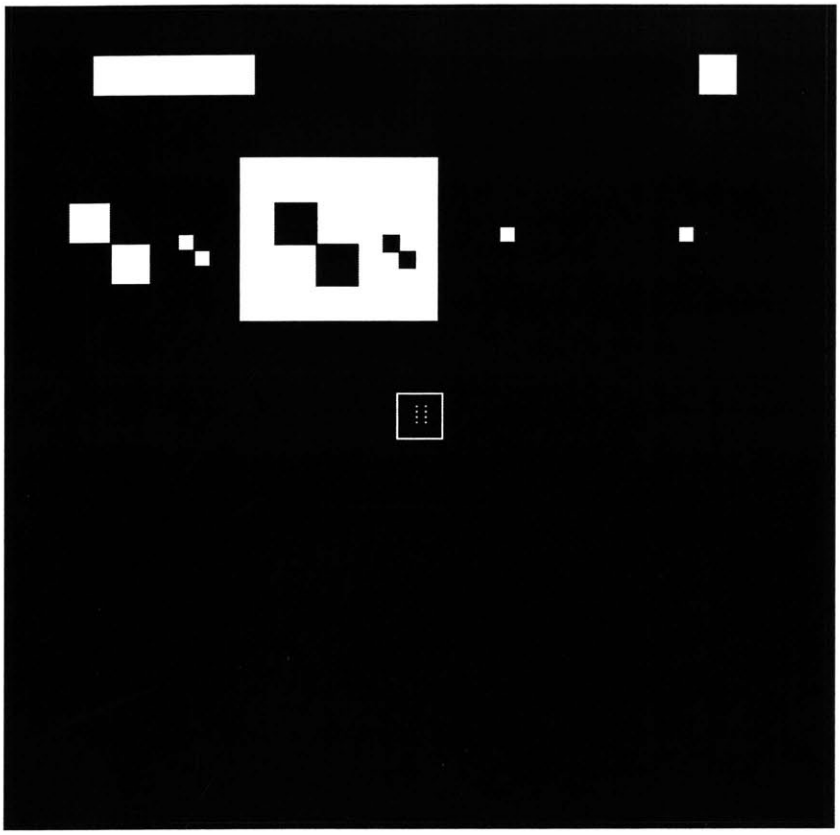

Figure A-2: Close up of a sample 1cm × 1cm die. Note the alignment and development test features in the top. The $500\mu m\times\ 500\mu m$ membrane is located in the center.

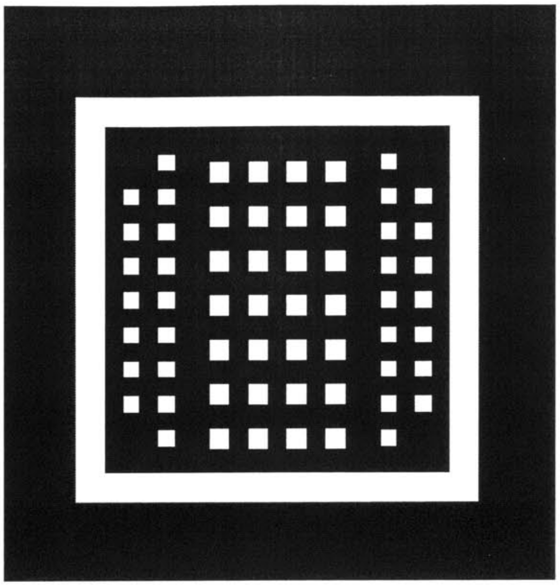

Figure A-3: Close up of a sample die depicting the $500\mu m \times 500\mu m$ membrane. The small squares are the original HF release holes.

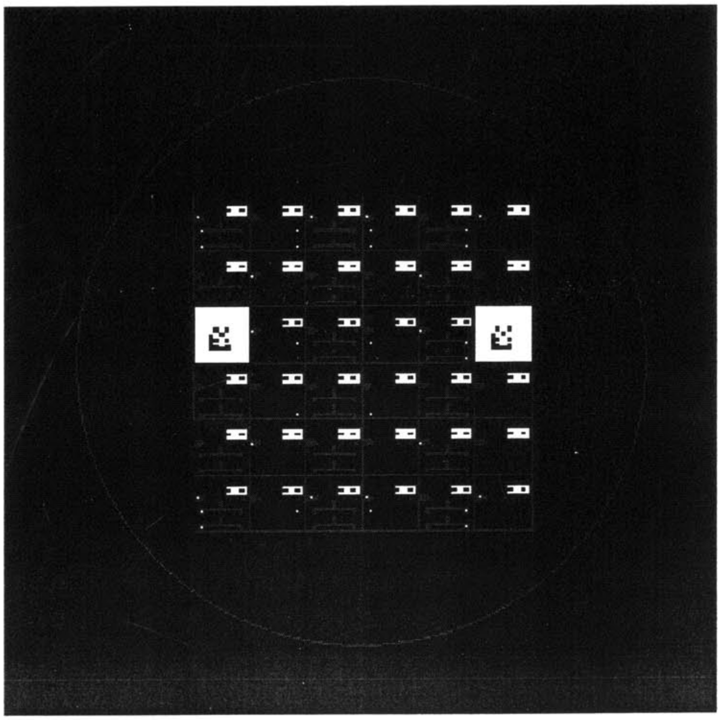

Figure A-4: Mask 2: Lift-off mask for Au/Cr wires and hinges.

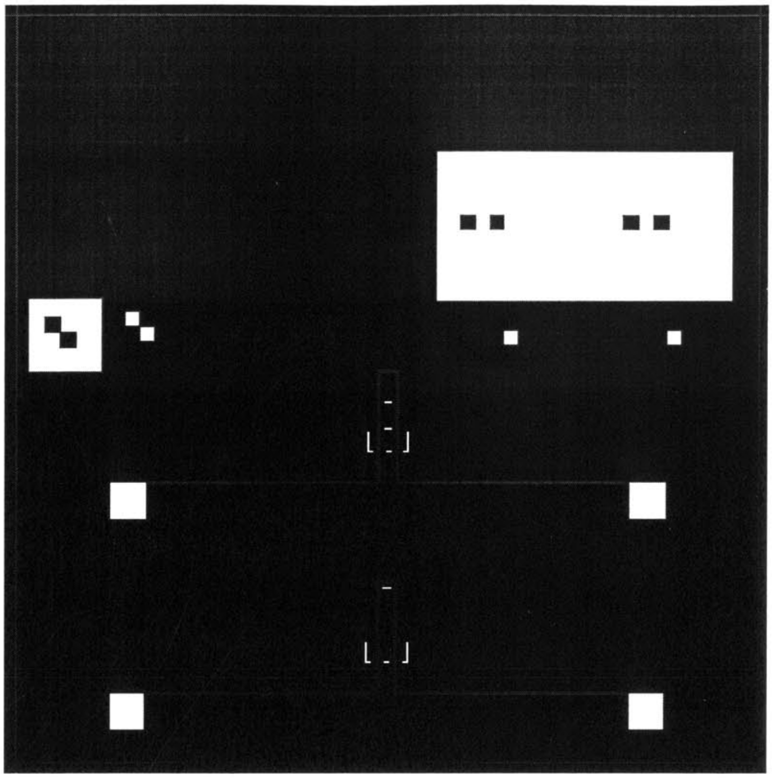

Figure A-5: Close up of a sample die. The top wire pattern is the device while the lower is a duplicate test wire.

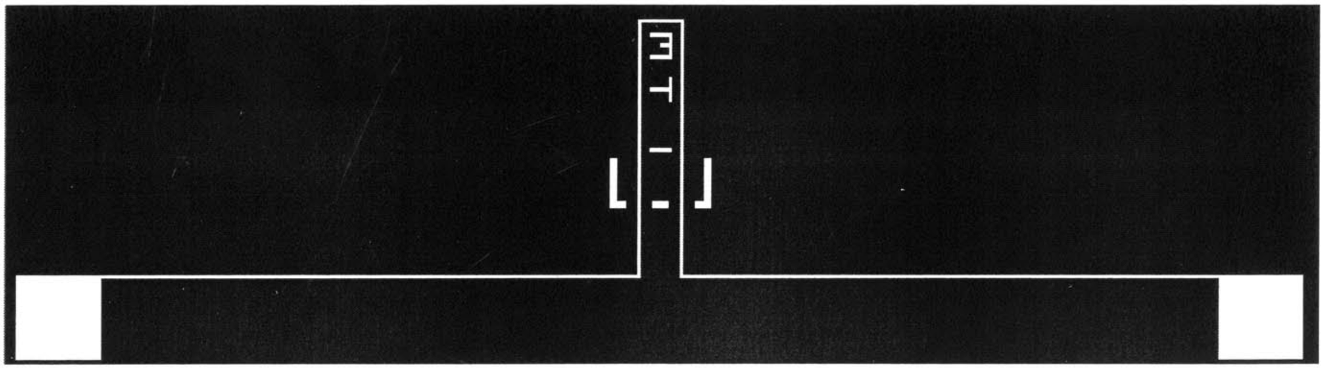

Figure A-6: Close up of sample die showing the Au/Cr wire pattern and alignment fiducials. The M, T, and I were also patterned so that once the fold is complete, they could be imaged with an IR camera and spell out MIT.

Appendix B

Chrome Masks - Second Round of Prototypes

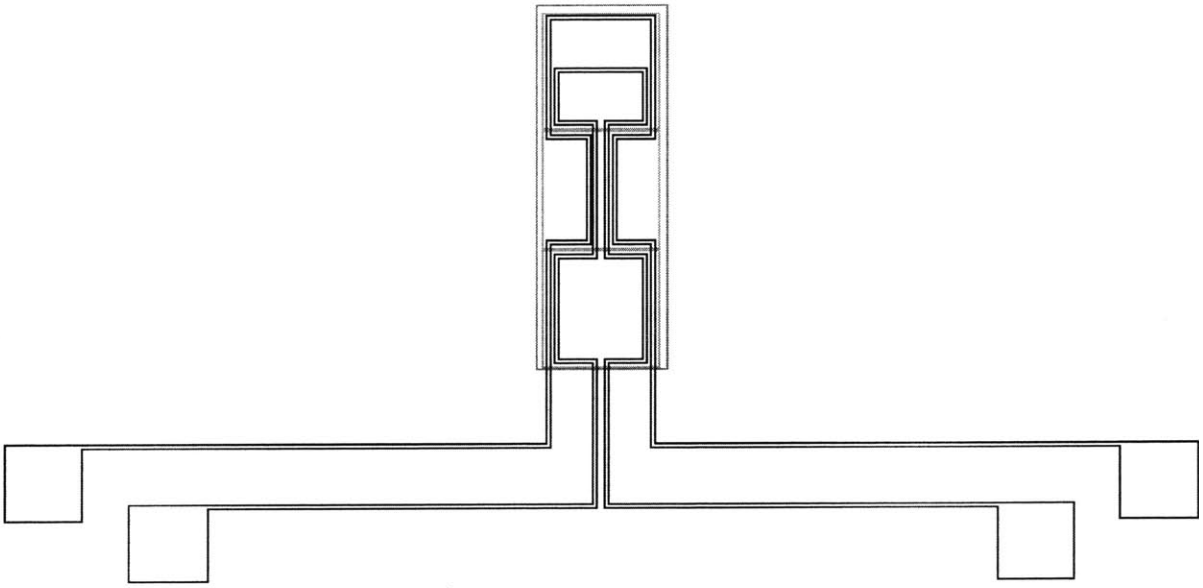

Figure B-1: Close up of CAD layout for a three membrane, multiple fold prototype. Both the silicon etch and wire masks are shown, superimposed. The two circuits are oriented so that moments of opposite sign are generated about the centerline of each flap.

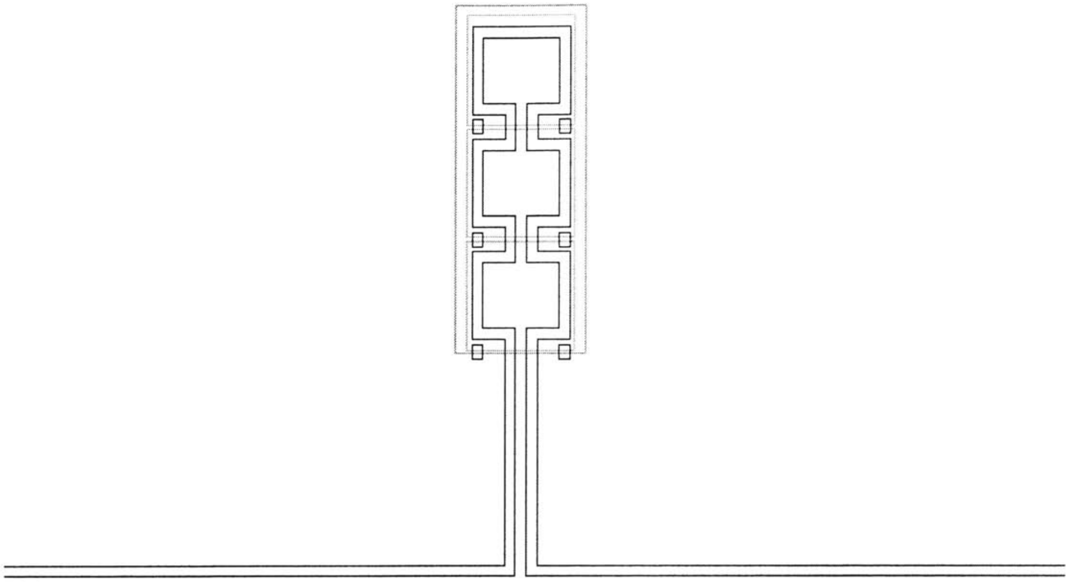

Figure B-2: Close up of CAD layout for a second type of multiple fold. A moment of the same sign and magnitude is generated on each of the three independent flaps. The expected motion is a curling effect.

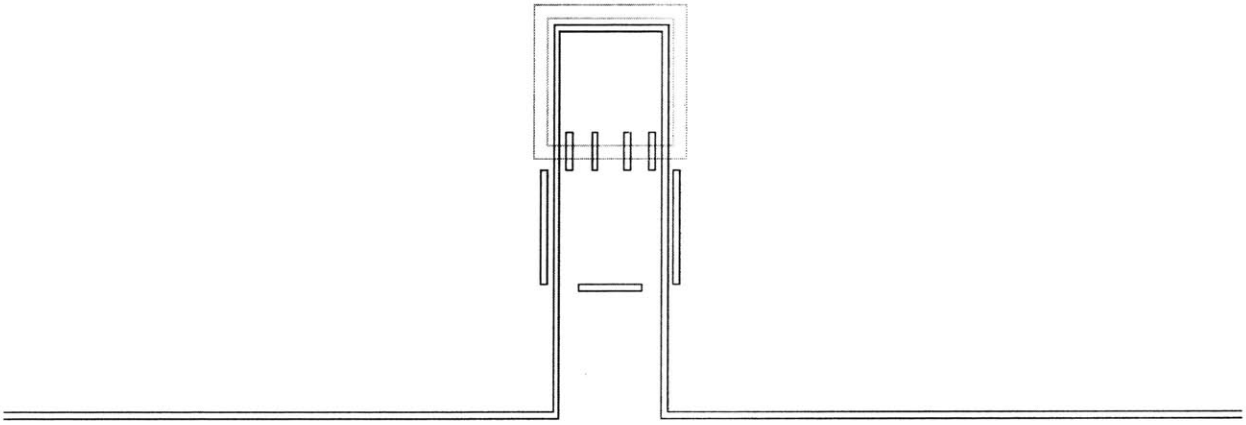

Figure B-3: Close up of CAD layout for a multiwire prototype. Both the silicon etch and wire lift-off mask are shown superimposed. Alignment fiducials are also displayed.

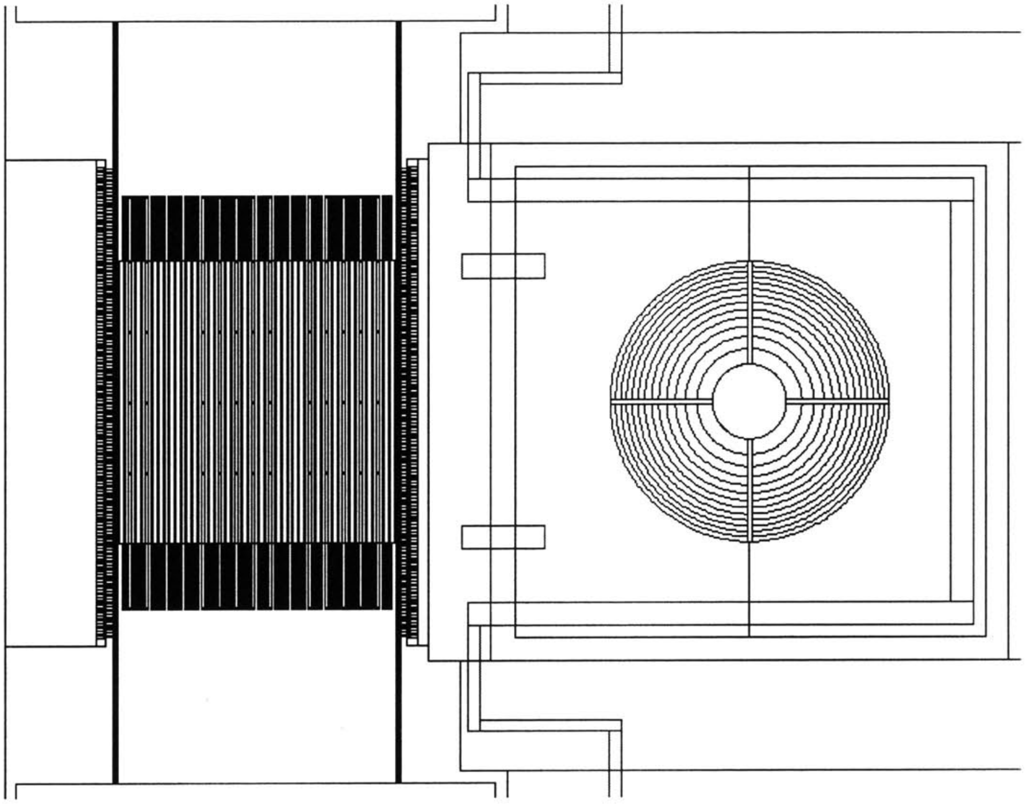

Figure B-4: Close up of CAD layout for static Fresnel zone plate and tunable diffraction grating. Both the silicon etch and wire lift-off are superimposed.

Appendix C

Process Flow - First Prototypes

Please see next page.

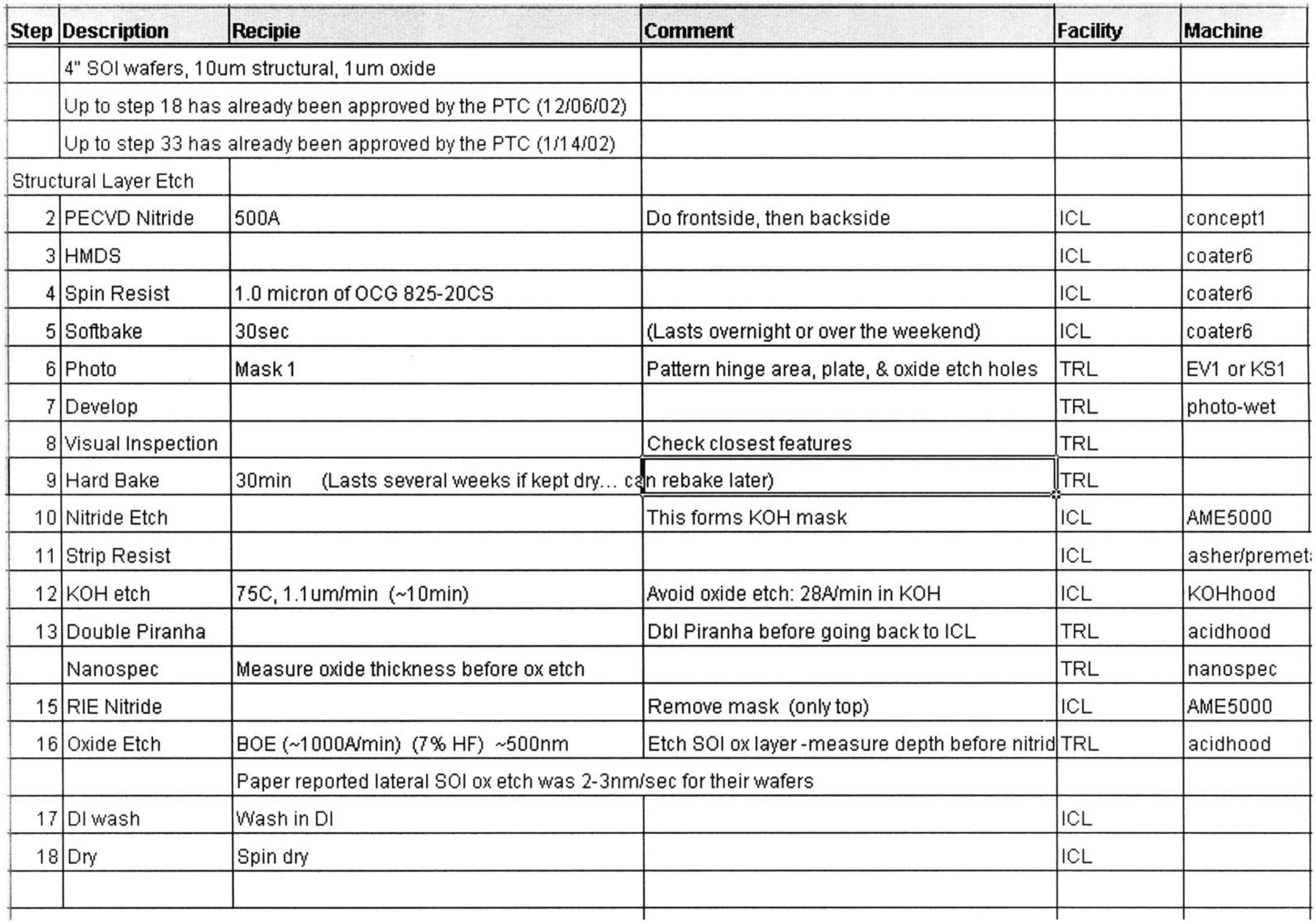

Step	Description	Recipie	Comment	Facility	Machine
	4" SOI wafers, 10um structural, 1um oxide				
	Up to step 18 has already been approved by the PTC (12/06/02)				
	Up to step 33 has already been approved by the PTC (1/14/02)				
Structural Layer Etch					
2	PECVD Nitride	500A	Do frontside, then backside	ICL	concept1
3	HMDS			ICL	coater6
4	Spin Resist	1.0 micron of OCG 825-20CS		ICL	coater6
5	Softbake	30sec	(Lasts overnight or over the weekend)	ICL	coater6
6	Photo	Mask 1	Pattern hinge area, plate, & oxide etch holes	TRL	EV1 or KS1
7	Develop			TRL	photo-wet
8	Visual Inspection		Check closest features	TRL	
9	Hard Bake	30min (Lasts several weeks if kept dry... ca	n rebake later)	TRL	
10	Nitride Etch		This forms KOH mask	ICL	AME5000
11	Strip Resist			ICL	asher/premet
12	KOH etch	75C, 1.1um/min (~10min)	Avoid oxide etch: 28A/min in KOH	ICL	KOHhood
13	Double Piranha		Dbl Piranha before going back to ICL	TRL	acidhood
	Nanospec	Measure oxide thickness before ox etch		TRL	nanospec
15	RIE Nitride		Remove mask (only top)	ICL	AME5000
16	Oxide Etch	BOE (~1000A/min) (7% HF) ~500nm	Etch SOI ox layer -measure depth before nitrid	TRL	acidhood
		Paper reported lateral SOI ox etch was 2-3nm/sec for their wafers			
17	DI wash	Wash in DI		ICL	
18	Dry	Spin dry		ICL	

Figure C-1: Process flow used to create first round of prototypes.

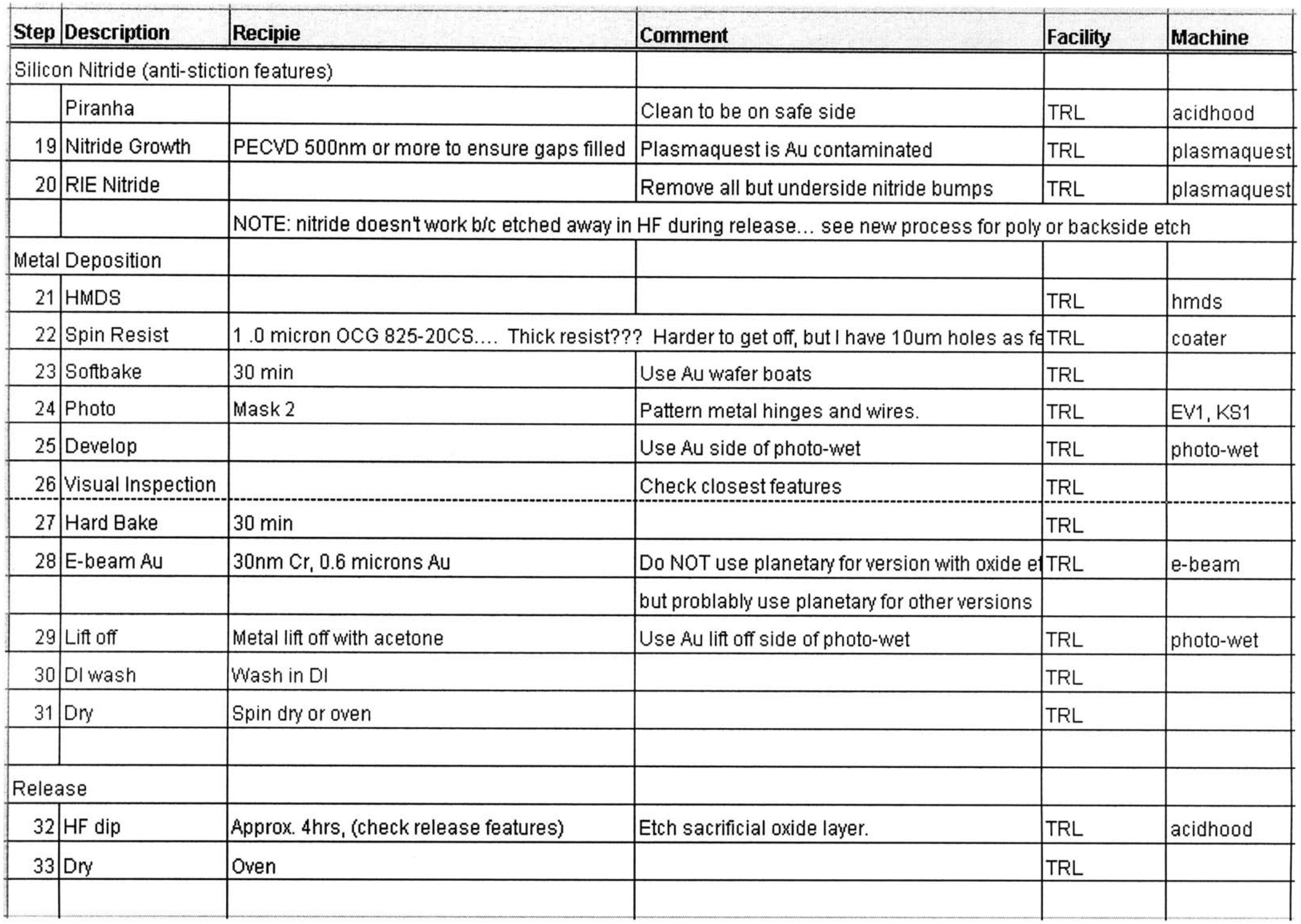

Step	Description	Recipie	Comment	Facility	Machine
Silicon Nitride (anti-stiction features)					
	Piranha		Clean to be on safe side	TRL	acidhood
19	Nitride Growth	PECVD 500nm or more to ensure gaps filled	Plasmaquest is Au contaminated	TRL	plasmaquest
20	RIE Nitride		Remove all but underside nitride bumps	TRL	plasmaquest
		NOTE: nitride doesn't work b/c etched away in HF during release... see new process for poly or backside etch			
Metal Deposition					
21	HMDS			TRL	hmds
22	Spin Resist	1 .0 micron OCG 825-20CS.... Thick resist??? Harder to get off, but I have 10um holes as fe		TRL	coater
23	Softbake	30 min	Use Au wafer boats	TRL	
24	Photo	Mask 2	Pattern metal hinges and wires.	TRL	EV1, KS1
25	Develop		Use Au side of photo-wet	TRL	photo-wet
26	Visual Inspection		Check closest features	TRL	
27	Hard Bake	30 min		TRL	
28	E-beam Au	30nm Cr, 0.6 microns Au	Do NOT use planetary for version with oxide e	TRL	e-beam
			but problably use planetary for other versions		
29	Lift off	Metal lift off with acetone	Use Au lift off side of photo-wet	TRL	photo-wet
30	DI wash	Wash in DI		TRL	
31	Dry	Spin dry or oven		TRL	
Release					
32	HF dip	Approx. 4hrs, (check release features)	Etch sacrificial oxide layer.	TRL	acidhood
33	Dry	Oven		TRL	

Figure C-2: Process flow used to create first round of prototypes (continued from last page).

Appendix D

Process Flow - Second Round of Prototypes

Please see next page.

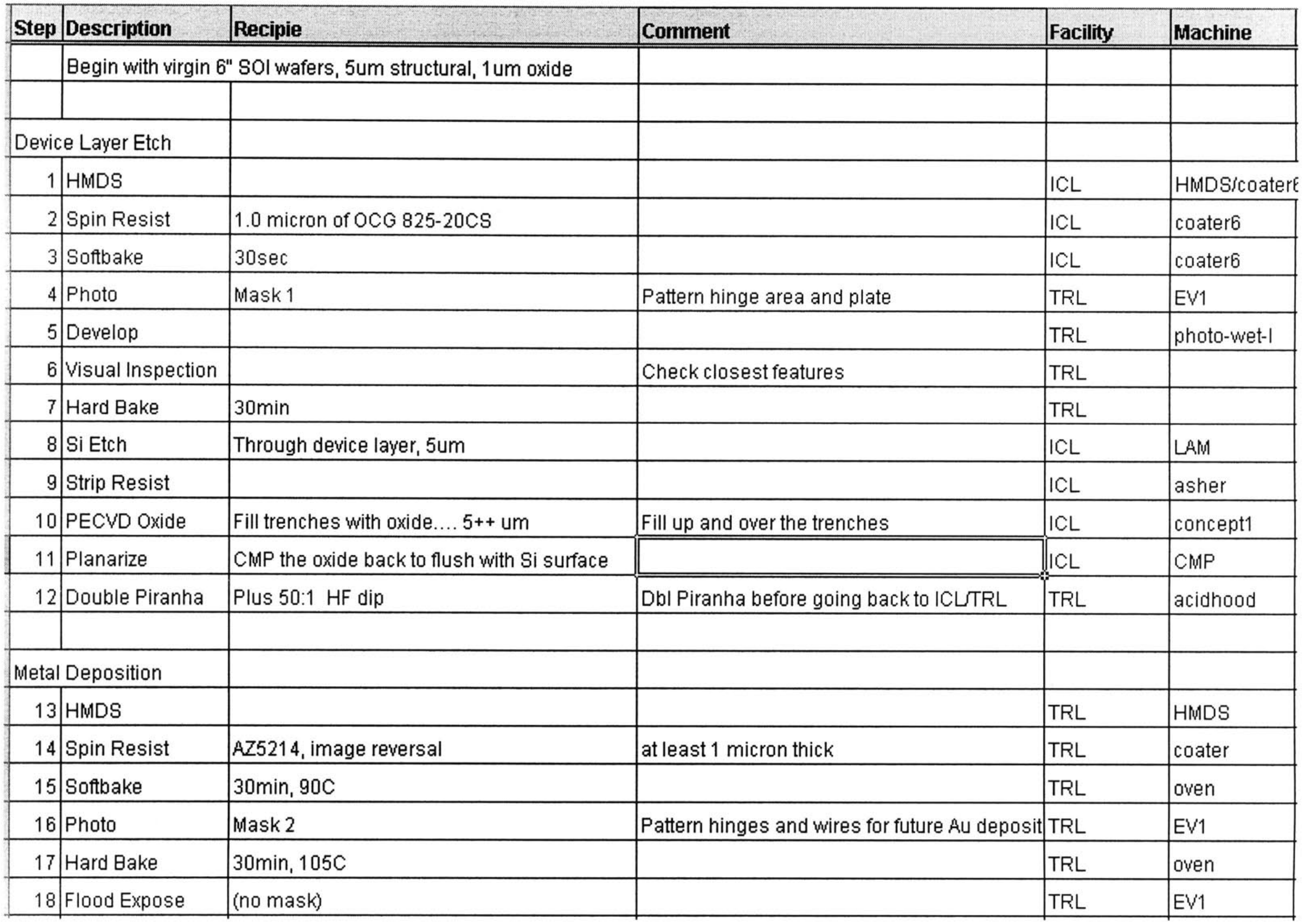

Step	Description	Recipie	Comment	Facility	Machine
	Begin with virgin 6" SOI wafers, 5um structural, 1um oxide				
Device Layer Etch					
1	HMDS			ICL	HMDS/coater
2	Spin Resist	1.0 micron of OCG 825-20CS		ICL	coater6
3	Softbake	30sec		ICL	coater6
4	Photo	Mask 1	Pattern hinge area and plate	TRL	EV1
5	Develop			TRL	photo-wet-l
6	Visual Inspection		Check closest features	TRL	
7	Hard Bake	30min		TRL	
8	Si Etch	Through device layer, 5um		ICL	LAM
9	Strip Resist			ICL	asher
10	PECVD Oxide	Fill trenches with oxide.... 5++ um	Fill up and over the trenches	ICL	concept1
11	Planarize	CMP the oxide back to flush with Si surface		ICL	CMP
12	Double Piranha	Plus 50:1 HF dip	Dbl Piranha before going back to ICL/TRL	TRL	acidhood
Metal Deposition					
13	HMDS			TRL	HMDS
14	Spin Resist	AZ5214, image reversal	at least 1 micron thick	TRL	coater
15	Softbake	30min, 90C		TRL	oven
16	Photo	Mask 2	Pattern hinges and wires for future Au deposit	TRL	EV1
17	Hard Bake	30min, 105C		TRL	oven
18	Flood Expose	(no mask)		TRL	EV1

Figure D-1: Process flow for second round of prototypes.

Step	Description	Recipie	Comment	Facility	Machine
19	Develop			TRL	photo-wet-l
20	Visual Inspection		Check closest features	TRL	
21	Microscope	Fringe technique to make sure PR removed		TRL	
22	Spin Rinse & Dry			TRL	
23	Descum	2 min @full power	Removes skim layer of PR	TRL	asher
24	E-beam Au	30nm Cr @ 2A/sec	Do not use planetary... want flat wafer.	TRL	e-beam
		0.6 microns Au @ 3A/sec		TRL	e-beam
25	Lift off	Metal lift off with acetone	Use Au lift off side of photo-wet	TRL	photo-wet-r
26	DI wash	Wash in DI		TRL	
27	Dry	Spin dry or oven		TRL	
28	Dektak		Correct hinge thickness and width?	TRL	dektak-Au
Backside Etch					
29	Cleave wafer	Cleave 6" wafer into smaller dies that fit inside plasmaquest - must leave alignment marks for bksd alignment			
30	Handle Mount	Mount dies to handle wafer with std. PR		TRL	
31	PECVD Nitride	2000A on backside only - use Joachim's SiNJoe2 recipe		TRL	plasmaquest
32	Handle Dismount	Acetone dismount		TRL	
33	HMDS	No PR in HMDS!!!!		TRL	hmds
34	Spin Resist	1 .0 micron OCG 825-20CS	Coat the backside	TRL	coater
35	Softbake	30 min		TRL	oven
36	Photo	Use Backside Etch Mask	Backside alignment	TRL	EV1
37	Develop		Use Au side of photo-wet	TRL	photo-wet
38	Visual Inspection		Check closest features	TRL	

Figure D-2: Process flow for second round of prototypes (continued from last page).

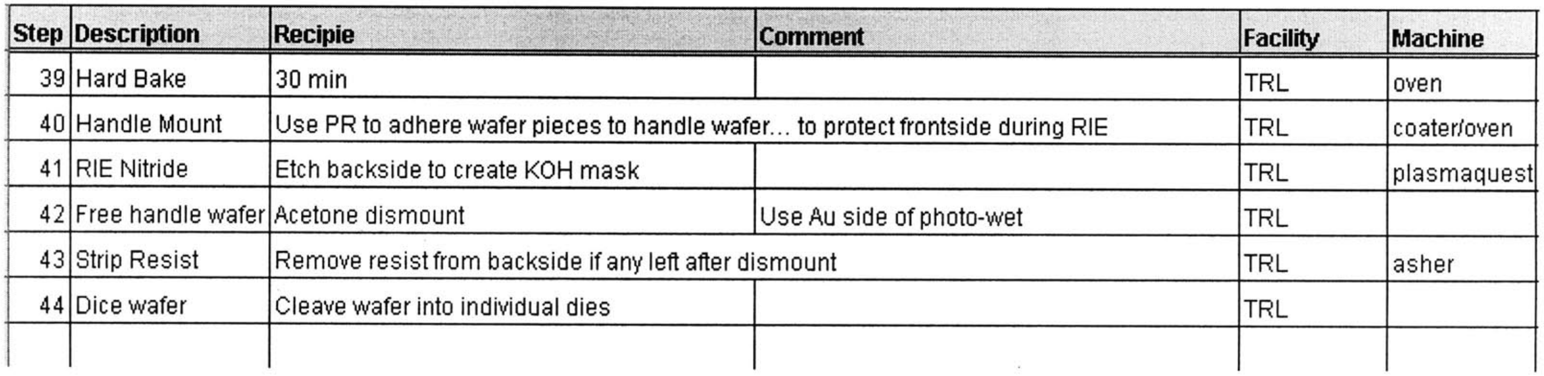

Step	Description	Recipie	Comment	Facility	Machine
39	Hard Bake	30 min		TRL	oven
40	Handle Mount	Use PR to adhere wafer pieces to handle wafer... to protect frontside during RIE		TRL	coater/oven
41	RIE Nitride	Etch backside to create KOH mask		TRL	plasmaquest
42	Free handle wafer	Acetone dismount	Use Au side of photo-wet	TRL	
43	Strip Resist	Remove resist from backside if any left after dismount		TRL	asher
44	Dice wafer	Cleave wafer into individual dies		TRL	

Figure D-3: Process flow for second round of prototypes (continued from last page).

Figure D-4: Pirate cannonball in the cleanroom.